RUPRECHT-KARLS-UNIVERSITÄT HEIDELBERG

Martin Swart

Mass Spectroscopy of Neutral Mesons in the Photon Hemisphere at HERA

Dissertation

HD-KIP-00-17

KIRCHHOFF-INSTITUT FÜR PHYSIK

INAUGURAL – DISSERTATION
zur
Erlangung der Doktorwürde
der
Naturwissenschaftlich–Mathematischen
Gesamtfakultät
der
Ruprecht–Karls–Universität
Heidelberg

vorgelegt von
Dipl.–Phys. Martin Swart
aus Karlsruhe

Tag der mündlichen Prüfung: 12. 7. 2000

HD-KIP-00-17

Mass Spectroscopy of Neutral Mesons in the Photon Hemisphere at HERA

Martin Swart

Gutachter: Prof. Dr. Karlheinz Meier
Prof. Dr. Franz Eisele

Dissertation
submitted to the
Joint Faculties for the Natural Sciences and for Mathematics
of the Ruperto - Carola - University of
Heidelberg, Germany,
for the degree of
Doctor rer. nat.

Mass Spectroscopy of Neutral Mesons in the Photon Hemisphere at HERA

presented by

Diplom–Physiker: Martin Swart
born in: Karlsruhe

Heidelberg, July 12th, 2000

Referees: Prof. Dr. Karlheinz Meier
Prof. Dr. Franz Eisele

Though this be madness,
yet there is method in't.

William Shakespeare,
Hamlet, act 2, scene 2

Abstract

The topic of this dissertation is the analysis of the inclusive photoproduction of neutral mesons with the H1 detector at HERA. The inclusive cross section for photoproduction of π^0 and η mesons is measured as a function of the transverse momentum and of the rapidity of the mesons at an average photon-proton center-of-mass energy of $W \approx 208$ GeV and for photon virtualities below $Q^2 = 0.01$ GeV^2. The mesons were reconstructed through their decays into two photons which were detected in the high resolution electromagnetic calorimeters of the H1 experiment. The π^0 and η measurements allow the kinematical region for the detection of single particle production to be extended, relative to previous charged particle measurements, by two rapidity units down to $y_{\mathrm{Lab}} = -3.5$ in the photon hemisphere. Comparison with model predictions shows good agreement. In order to study different production mechanisms of the π^0 and η mesons their relative production cross section as a function of the particles' transverse momenta was determined and compared with previous results of the Omega Photon Collaboration ($W_{\gamma p} \approx 13.7$ GeV). Finally, acceptance studies showed that the investigation of higher mass mesons whose decay cascade proceeds via the π^0 and η particles into pure photonic final states is possible only in an exclusive measurement.

Zusammenfassung

Die inklusive Photoproduktion neutraler Mesonen mit dem Detektor H1 bei HERA ist das Thema dieser Arbeit. Der inklusive Wirkungsquerschnitt für die π^0- und η-Produktion ist als Funktion der Transversalimpulse und der Rapiditäten der Mesonen bei einer mittleren Schwerpunktsenergie des Photon-Proton-Systems von $W_{\gamma p} \approx 208$ GeV und bei einer Photon Virtualität von $Q^2 < 0.01$ GeV^2 gemessen worden. Die Mesonen wurden durch ihren Zerfall in zwei Photonen rekonstruiert. Die Photonen sind in den hoch auflösenden Kalorimetern des H1-Experiments nachgewiesen worden. Bezogen auf eine frühere H1-Messung von geladenen Teilchen, erlaubt diese Messung den kinematischen Bereich der Teilchenproduktion um zwei Rapiditätseinheiten bis zu Werten von $y_{\mathrm{Lab}} = -3.5$ in die Photon-Hemisphäre auszudehnen. Ein Vergleich der Daten mit Modellvorhersagen zeigt eine gute Übereistimmung. Zur Untersuchung unterschiedlicher Produktionseigenschaften der π^0- und η-Mesonen wurde das Verhältnis ihrer Produktionswirkungsquerschnitte als Funktion der Transversalimpulse der Mesonen gebildet und mit früheren Ergebnissen der Omega-Photon Kollaboration ($W_{\gamma p} \approx 13.7$ GeV) verglichen. Schliesslich konnte gezeigt werden, dass die Untersuchung schwererer Teilchen, die über π^0- und η-Mesonen in reine Photonzustände kaskadieren, mit dem H1 Detektor aus Akzeptanzgründen nur in einer exklusiven Messung möglich ist.

Contents

List of Tables

List of Figures

Introduction

The analysis presented here is divided into two parts. The first part, the core of this analysis, is devoted to the investigation of inclusive photoproduction of π^0 and η mesons off protons at γp center-of-mass (CM) energies around $W \approx 208$ GeV. The second part deals with the search for higher mass mesons, for example the ω, $f_2(1270)$ and the glueball candidate $f_0(1500)$.

At the electron-proton collider HERA[1], photoproduction (γp) processes are induced by quasi-real photons that are emitted by the incoming electron or positron. The electron is detected at small scattering angles to ensure that the photon virtuality is below $Q^2 = 0.01$ GeV^2. The majority of the photon–proton interactions are "soft" scattering processes in which particles with limited transverse momenta are produced. These fragments of the photon, as the projectile, populate mainly the phase space region at low values of Feynman x.

A small fraction of γp processes, however, arises due to "hard" scatterings. In these, the photon either interacts as a single object with a parton from the proton ("direct" photon interaction) or via a parton-parton scattering after fluctuating into a partonic system. These latter "resolved" photon processes give rise to a photon remnant system following the direction of the incoming photon.

Investigations of the photon remnant with charged particles at HERA have been made before, using the central tracking detectors of the experiments H1 and ZEUS [ABT94, ADL99, DE95a]. With these devices, the photon hemisphere was explored for particles produced up to 3.5 units of rapidity away from the central photon–proton rapidity region, as measured in the γp center-of-mass system (CMS), and for values of transverse momenta up to 12 GeV/c. The measurement described in this thesis is an extension towards an as yet unexplored phase space region in which charged particles can no longer be reliably recorded by the H1 detector, owing to limitations in acceptance of the tracking devices.

The inclusive double differential π^0 and η photoproduction cross section is measured as a function of the particle transverse momentum and rapidity in the laboratory frame and, in the case of the π^0s, as a function of Feynman x in the γp CMS. The π^0 and η mesons are identified through their decay into two photons which are detected in the electromagnetic calorimeters of the H1 detector. The large acceptance of these calorimeters together with their fine granularity and high resolution gives access to laboratory rapidities ranging down to $y = -3.5$, i.e. 5.5 units of rapidity away from the central photon–proton rapidity region, and to transverse momenta up to 2 GeV/c.

The measured cross sections allow a check of the reliability of MC predictions in the transition region between soft and hard scattering processes, and they allow a study of

[1] In the 1996 running period, HERA (Hadron Electron Ring Accelerator) was operated with a positron beam. In this thesis "electron" is used as a generic term in technical contexts.

the primordial transverse momentum $k_\perp$ of the photon. The investigation of the ratio of the η and π^0 photoproduction cross sections shows that both cross sections approach each other with increasing values of the transverse momenta of the mesons.
Moreover, this measurement of inclusive meson spectra can be considered as the condition and technical preparation for the investigation performed in the second part, namely the particle spectroscopy in the higher mass range. The decay of the scalar $f_0(1500)$ into two η mesons and the decay of the tensor meson $f_2(1270)$ into two π^0 mesons were studied. Both decays are of interest e.g. in the context of the glueball search or in the context of rare production processes like odderon-photon fusion. It turned out that the higher mass meson spectroscopy is possible only in an exclusive measurement due to acceptance limitations of the H1 detector.

Chapter 1

Hadronic Manifestations of the Photon

The main objective of the physics program at HERA is the investigation of the proton structure. For this purpose the HERA accelerator was built for the collision of 27.5 GeV electrons with 820 GeV protons. The CM energy of this collision is $\sqrt{s} = 300$ GeV. The square of the four-momentum transfer, Q^2, which describes the resolving power of the reaction, reaches from $Q^2 \approx 0$ GeV^2 to $Q^2 \approx 9 \cdot 10^4$ GeV^2, allowing a probe of the structure of the proton down to 10^{-16} cm.
In general the scale of Q^2 is used to distinguish between two regimes:

1) the Deep Inelastic Scattering (DIS) regime, in which the ep reaction is dominated by the photon exchange; the Z and W exchanges contribute significantly only for $Q^2 \gtrsim M^2_{Z,W}$. The transverse distances resolved by the photon in DIS are a fraction of the proton radius, thus allowing an investigation of the details of the proton structure.

2) the photoproduction regime, associated with the region of vanishing values of Q^2, where the interaction is mediated by a "quasi-real" photon ($Q^2 \approx 0$). The transverse distance determined by the scale of Q^2 in photoproduction is clearly larger than the proton radius. The structure of the proton is not expected to be important for the γp cross section. Events of this kinematical region are much more of interest for studying the photon. Previous fixed target experiments [BAN85, BUE73, KOU80], using both charged particle beams and photon beams, have shown that photoproduction can be viewed as hadron-hadron scattering in which the photon fluctuates into a vector meson. The CM energies of previous γp experiments in this context range up to 19 GeV.

The subject of this analysis is related to point 2). It studies mainly the light meson photoproduction at an average γp CM energy of 208 GeV, which is about a factor of 10 larger than the CM energies reached by previous fixed target experiments. Since HERA is an ep and not a γp collider the quantities needed for the description of photoproduction are derived in this chapter from the quantities used in the context of DIS. The discussion of the hadronic manifestations of the photon at HERA energies leads to the model of the photon, as studied in [SCH93]. Finally, this chapter briefly describes the Monte Carlo event generators for photoproduction used in this analysis, PHOJET and PYTHIA. The kinematics at HERA is illustrated by means of the π^0 and η production.

1.1 Kinematical Variables in *ep* Scattering Processes

Figure 1.1 is a schematic diagram describing deep inelastic lepton-proton scattering. At HERA energies the *ep* interaction dominantly proceeds via the exchange of a virtual photon. Due to the lepton number conservation one expects a scattered electron in the final state while the proton fragments into a hadronic final state X.

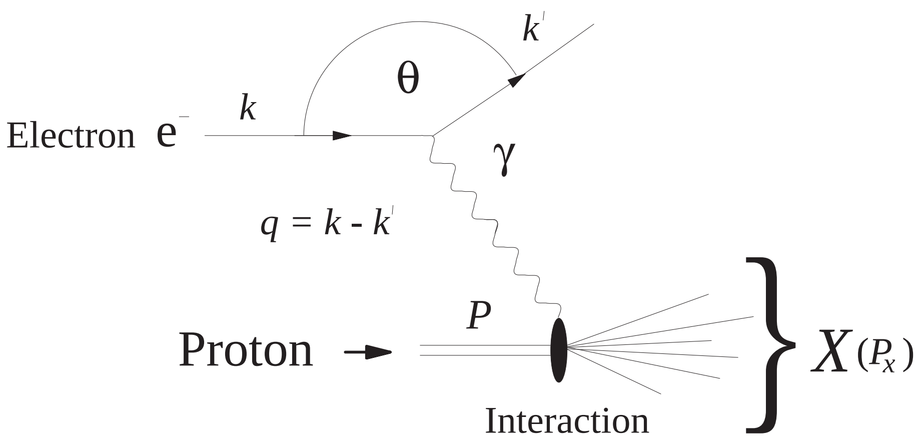

Figure 1.1: *Electron-Proton scattering via photon exchange. k, k', P and P_x denote the four-momenta used to construct Lorentz-invariant quantities.*

With k, k', P and P_x representing the four-momenta of the initial and final state lepton and the four-momenta of the incoming proton and the outgoing hadronic final state, respectively, the following set of Lorentz invariant quantities is commonly used for the description of DIS:

The CM energy squared

$$s = (P + k)^2 \tag{1.1}$$

The invariant mass squared of the exchanged virtual photon

$$Q^2 = -q^2 = -(k - k')^2 \tag{1.2}$$

$$\stackrel{\text{lab}}{=} 4E_e E'_e \cos^2 \frac{\theta}{2} \tag{1.3}$$

where E_e and E'_e denote the energy of the incoming and outgoing electron, respectively, neglecting the lepton mass m_e. The polar angle θ of the scattered electron is defined with respect to the direction of the incoming proton. The value of Q^2 determines the resolution b of the scattering process with:

$$b \sim \frac{hc}{\sqrt{Q^2}} = \frac{0.199}{\sqrt{Q^2/\,\mathrm{GeV}^2}}\,\mathrm{fm} \tag{1.4}$$

Furthermore the two dimensionless variables x and y are defined as

$$x = \frac{Q^2}{2Pq} \stackrel{\text{lab}}{=} \frac{E_e E'_e \cos^2\frac{\theta}{2}}{E_p(E_e - E'_e \sin^2\frac{\theta}{2})} \tag{1.5}$$

$$y = \frac{Pq}{Pk} \stackrel{\text{lab}}{=} 1 - \frac{E'_e}{E_e}\sin^2\frac{\theta}{2} \tag{1.6}$$

Both of them are confined to the range from 0 to 1. The variable x is often called the "Bjorken scaling variable", which is interpreted in the Quark Parton Model (QPM) as the fraction of the proton momentum carried by the struck massless quark. The variable y supplies a measure of the fraction of the energy transferred from the electron to the boson mediating the interaction.
Using the definition of the variable x, the invariant mass W of the hadronic system can be expressed by:

$$W^2 \equiv (q+P)^2 \stackrel{\text{lab}}{=} Q^2\frac{1-x}{x} + m_p^2 \tag{1.7}$$

where m_p is the proton rest mass. W^2 ranges from m_p^2 to s.
The kinematical variables x, y and Q^2 are not independent of each other, but related with the CM energy squared by the expression

$$Q^2 = xys, \tag{1.8}$$

neglecting the lepton and proton masses. Thus, for a given CM energy, two variables already completely determine the DIS process.

For the kinematical region studied in this analysis the massive boson exchange can be neglected ($Q^2 << M_Z^2$), and the *ep* scattering can be considered as a source of virtual photons, interacting with the proton. In this picture, the *ep*-cross section can be decomposed into a term representing the photon flux Φ from the electron, and a term representing the photon-proton scattering process. Therefore, the differential electron-proton cross section is given here in terms of the flux factor Φ and of σ_T, σ_L, the absorption cross sections for transversely and longitudinally polarized photons:

$$\frac{\mathrm{d}^2\sigma(e^\pm p)}{\mathrm{d}y\,\mathrm{d}Q^2} = \Phi(y,Q^2)\cdot\left[\sigma_T(y,Q^2) + \frac{2(1-y)}{(1+(1-y)^2)}\sigma_L(y,Q^2)\right] \text{ with:} \tag{1.9}$$

$$\Phi(y,Q^2) = \frac{\alpha}{2\pi}\cdot\frac{1}{yQ^2}\cdot\left(1+(1-y)^2\right)$$

The transverse and longitudinal photon cross sections are determined by the structure functions of the proton, F_1 and F_2:

$$\sigma_T(x,Q^2) = \frac{4\pi^2\alpha}{Q^2}\cdot 2xF_1(x,Q^2) \tag{1.10}$$

$$\sigma_L(x,Q^2) = \frac{4\pi^2\alpha}{Q^2}\cdot F_L(x,Q^2) \tag{1.11}$$

F_L implies the Callan-Cross relation where the proton mass m_p is not neglected:

$$F_L(x,Q^2) \equiv \left(1+\frac{4m_p^2x^2}{Q^2}\right)F_2(x,Q^2) - 2xF_1(x,Q^2) \tag{1.12}$$

F_L is proportional to the absorption cross section for longitudinal photons. In the QPM the structure functions are calculated as the probability for finding a quark (antiquark) with momentum fraction x in the proton, times the coupling factor e_f, the electric charge of the parton with flavour f, summed over all flavours in the proton:

$$F_1(x,Q^2) = \frac{1}{2\,x} F_2(x,Q^2) \tag{1.13}$$

$$F_2(x,Q^2) = \sum_{\text{flavours}} \left[x\, q_f(x,Q^2) + x\, \bar{q}_f(x,Q^2) \right] e_f^2 \tag{1.14}$$

Introducing the ratio:

$$R(x,Q^2) \equiv \frac{\sigma_L}{\sigma_T} \tag{1.15}$$

gives a relation between the total cross sections of transversely and longitudinally polarized photons to the structure function F_2:

$$\sigma_T(x,Q^2) = \frac{4\pi^2\alpha}{Q^2} \left(1 + \frac{4m_p^2 x^2}{Q^2} \right) \frac{1}{1+R(x,Q^2)} \cdot F_2(x,Q^2) \tag{1.16}$$

All functions outlined in this section are valid for ep scatterings with pure photon exchange ($Q^2 << M_Z^2$). The following section 1.2 discusses the modifications of these functions for the case of the additional restriction $Q^2 \to 0$, by which the photon can be considered as "quasi-real".

1.2 From *ep* to *γp* Cross Section in Photoproduction

Photoproduction denotes the kinematical region in which the photon can be considered as "quasi-real". For $Q^2 \approx 0$ the contributions to the cross section from longitudinally polarized photons can be neglected, and the equations above can be simplified. Equation 1.7 shows that for $Q^2 \approx 0$ also the Bjorken scaling variable x vanishes:

$$x = \frac{Q^2}{Q^2 + W^2 - m_p^2} \approx \frac{Q^2}{W^2} \approx 0. \tag{1.17}$$

According to equation 1.6 the variable y can simply be written as $y \approx 1 - E'_e/E_e$ for a value of the polar angle of the scattered electron θ close to π. The invariant mass of the hadronic system $W_{\gamma p}$, representing in photoproduction the CM energy of the γp system $\sqrt{s_{\gamma p}}$, yields

$$s_{\gamma p} = W_{\gamma p}^2 = ys(1-x) + m_p^2 \approx ys \tag{1.18}$$

using equations 1.8 and 1.7.
In photoproduction the cross section of the transversely polarized photons $\sigma_T(x,Q^2)$, as expressed in equation 1.16 with the help of the structure function F_2, represents the total γp cross section,

$$\sigma_{\text{tot}}^{\gamma p}(W_{\gamma p}) = \frac{4\pi^2\alpha}{Q^2} F_2(x,Q^2)\Big|_{Q^2=0} \tag{1.19}$$

which now depends on only one variable, $W_{\gamma p}$. Since $\sigma_{\mathrm{tot}}^{\gamma p}(W_{\gamma p})$ is a finite quantity it follows that $F_2 \propto Q^2$ for $Q^2 \to 0$. Due to the fact that it is technically impossible to measure $\sigma_{\mathrm{tot}}^{\gamma p}(W_{\gamma p})$ in ep interactions in the limit $Q^2 \approx 0$, one must refer to the differential cross section given in equation 1.10 which yields for real photons the Weizäcker-Williams approximation:

$$\frac{\mathrm{d}^2\sigma(e^{\pm}p)}{\mathrm{d}y\,\mathrm{d}Q^2} = \underbrace{\frac{\alpha}{2\,\pi\,Q^2} \cdot \left(\frac{1+(1-y)^2}{y}\right)}_{=\,\Phi(y,Q^2)} \cdot \sigma_{\mathrm{tot}}^{\gamma p}(ys) \tag{1.20}$$

where $Q^2_{\mathrm{min}} = m_e^2 y^2/(1-y)$ is the kinematic lower limit on Q^2, set by experimental conditions. An improved calculation of the photon flux is described in [FRI93] where particular experimental conditions of HERA were taken into account, leading to the improved Weizäcker-Williams approximation:

$$\frac{\mathrm{d}^2\sigma(ep)}{\mathrm{d}y\,\mathrm{d}Q^2} = \Phi'(y,Q^2)\cdot\sigma_{\mathrm{tot}}^{\gamma p}(ys) \tag{1.21}$$

with:

$$\Phi'(y,Q^2) = \frac{\alpha}{2\,\pi\,Q^2}\left(\frac{(1+(1-y)^2)}{y} - \frac{2(1-y)}{y}\,\frac{Q^2_{\mathrm{min}}}{Q^2}\right) \tag{1.22}$$

1.3 Kinematical Quantities of the Final State

The quantities mentioned so far describe scattering processes in DIS and photoproduction. They are not directly measurable in the experimental setup but they can be derived from the variables $p_\perp$, ϕ and θ, characterizing the particles of the final state; $p_\perp$ is the transverse momentum of the particle with respect to the beam line, ϕ its azimuthal angle around the beam line and θ its polar angle. The final-state variables with respect to the H1 coordinate system are shown in figure 1.2.

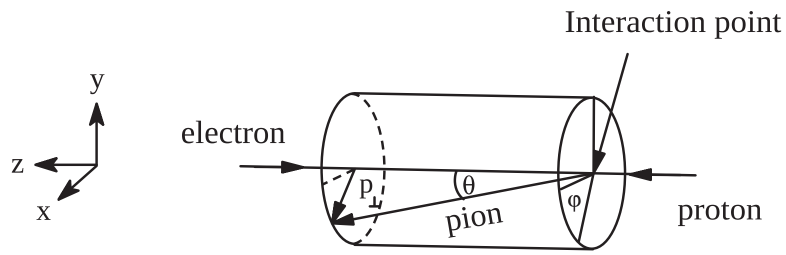

Figure 1.2: *Variables of the hadronic final state.*

Another variable, often used for the description of the final state, is the rapidity of a particle which is defined by:

$$y = \frac{1}{2}\ln\left(\frac{E+p_z}{E-p_z}\right) \tag{1.23}$$

$$= \tanh^{-1}\left(\frac{p_z}{E}\right) \tag{1.24}$$

where z defines the beam direction. Under a boost in the z direction to a frame with velocity β, y transforms as $y \rightarrow y - \tanh^{-1}(\beta)$, i.e. the shape of the rapidity distribution $\mathrm{d}N/\mathrm{d}y$ is invariant under this transformation. In the CM system the maximal rapidity values, accessible for particles at a certain CM energy, can be approximated by $(y_{\mathrm{CM}})_{\max} = ln(\sqrt{s}/m)$ requiring $p_\perp << |p_z|$. With an average γp CM energy of 208 GeV, where the π^0 and η cross section is measured, the maximal rapidity value accessible for π^0 mesons is 7.3 and 6.0 for η mesons.

For $p >> m$ the rapidity y can be approximated by the pseudo-rapidity

$$\eta = -\ln \tan \frac{\theta}{2} \tag{1.25}$$

with $\theta = \arccos(p_z/p)$. Thus the polar angle θ can be expressed in terms of the pseudo-rapidity η. According to equation 1.25 a particle with a polar angle of $\theta \approx 180^\circ$ corresponds to a value in pseudo-rapidity of $\approx -\infty$ while a centrally produced particle with θ around 90° correspond to a value around 0 in pseudo-rapidity.

From now on the variable y of equation 1.6 is denoted by y_{B} in order to avoid any confusion between this variable and the rapidity y of the mesons.

1.4 Hadronic Characteristics of the Photon

This chapter leads from the similarities between hadron-hadron scattering and photon-hadron scattering via the Vector-Meson-Dominance-Model (VDM) to the current understanding of the photon. The results of two HERA experiments, each of which focuses on certain aspects of the photon, are described and their relevance for this analysis is pointed out.

From previous fixed-target experiments it is known that photon-proton interactions can be understood in terms of hadron-hadron reactions. The most obvious similarity between them is the behaviour of the total cross section as a function of the CM energy, illustrated in figure 1.3. Hadron-proton as well as photon-proton interactions have a large cross section at low energies due to elastic scattering processes which becomes smooth at high energies where a slight universal rise of the cross section is visible. For meson-proton and photon-proton collisions ($\pi^\pm p$, $K^\pm p$, γp) a clear resonance region is visible. The photon-proton cross section is smaller by a factor roughly equal to the fine structure constant α.

The energy dependences for hadron-hadron and photon-hadron collisions can be fitted by an expression of the form $As^{-0.4525} + Bs^{0.0808}$. The first component mainly determines the cross section a low CM energies while the second one describes the universal rise of the cross section with increasing values of the CM energy $\sqrt{s}$. Figure 1.4 displays the dependence of the total photoproduction cross section as a function of the CM energy W.

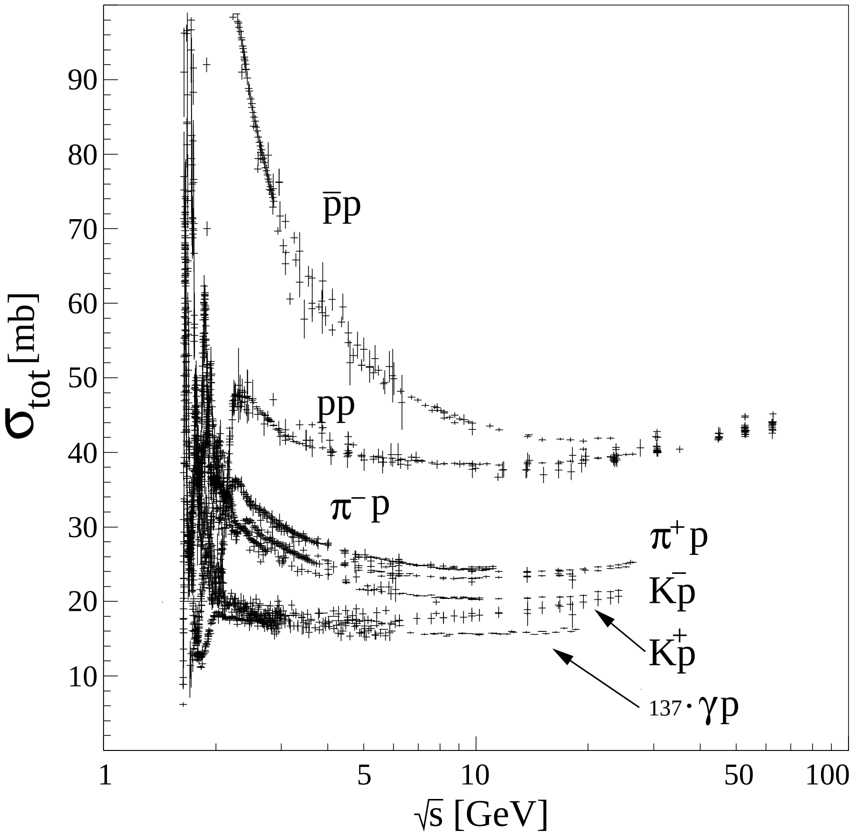

Figure 1.3: *Total cross section for various particle reactions as a function of the CM energy. The photon-proton cross sections have been multiplied by a factor of* $\frac{1}{\alpha_{em}}$.

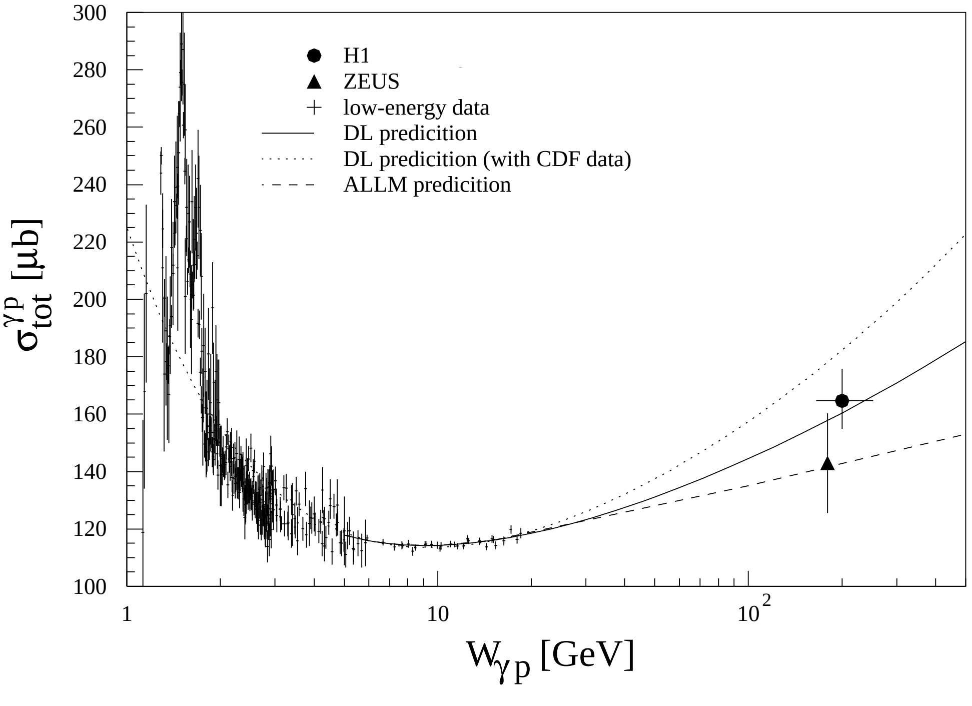

Figure 1.4: *Total* γp *cross section as measured at HERA.*

The data points in the higher energy range around 200 GeV show the total photoproduction cross section as measured by the H1 (full point) [ABT95] and ZEUS (triangle) [DER94] Collaborations at HERA. The results are in good agreement with the prediction of a fit performed by Donnachie and Landshoff (DL) in 1992 [DON92], describing the rise of the cross section with a function proportional to $(W^2_{\gamma p})^{0.0808}$. The fit is parameterized by the energy dependence found in hadron-hadron interactions (low-energy data) and extrapolated to the HERA energy range. The data points are also compared with a similar fit performed by Donnachie and Landshoff which includes the CDF measurement of the $p\bar{p}$ cross section, performed in 1994 at Fermilab [ABE94]. The inclusion of these data results in a description of the total γp cross section $\sigma^{\gamma p}_{\rm tot}$ by a function proportional to $(W^2_{\gamma p})^{0.11}$ which slightly overestimates the data. Also quite a good prediction of the measured cross section in the HERA energy range is supplied by the parametrisation of H. Abramowicz, E. M. Levin, A. Levy and U. Maor (ALLM) in which a function proportional to $(W^2_{\gamma p})^{0.045}$ [ABR91] is used. Despite the spread of the predicted cross sections the compatibility of the HERA results with DL and ALLM parametrisations is an additional confirmation of the hadronic behaviour of the photon.
The observed similarities between hadron-hadron and photon-hadron scattering led to the Vector-Dominance-Model (VDM) which was developed in the early sixties (a historical review is given in [BAU78]).
In the VDM the photon is understood as a superposition of a bare photon $|\gamma_b\rangle$ and a small hadronic component $|h\rangle$ of order $\sqrt{\alpha_{\rm em}}$. This term allows the photon to fluctuate into a $q\bar{q}$ pair forming a hadronic state which has the same quantum numbers as the photon ($J^{PC} = 1^{--}, Q = B = S = 0$). For neutral vector mesons in the ground state the latter requirement is fulfilled. According to the event classification in the hadron-hadron scattering γp interactions can be subdivided into:

- **diffractive processes**
  In diffractive processes no colour charge is exchanged. The interaction of the colliding particles is attributed to the exchange of an object with the quantum numbers of the vacuum. Experimentally, diffractive processes are characterized by a large rapidity gap in the final state. They are subdivided into:

  - **elastic events**
    In elastic events, $\gamma + p \to V + p$, the incoming photon fluctuates into a vector meson V, predominantly into a ρ^0, ω, ϕ, which is elastically scattered off the proton. The compton scattering process, $\gamma + p \to \gamma + p$, is higher by one order in α_{em} than the elastic VDM process and can be neglected.
  - **single and double diffractive events**
    In single and double diffractive events either one of the interaction particles is excited and then fragments into hadrons (single photon or proton dissociation) or both are excited and then fragment into hadrons.

- **non-diffractive processes**
  In non-diffractive processes, $\gamma + p \to X$, no large rapidity gap is seen in the final state. X denotes the hadronic final state.

In the low-$p_\perp$ region, covered by fixed-target photoproduction experiments, the VDM successfully describes the $\sigma_{\gamma p}$ cross section in terms of the vector meson proton cross section, σ_{Vp},

$$\sigma_{\gamma p}^{\mathrm{VDM}} = \sum_{V=\rho^0,\omega,\phi} \frac{4\pi\alpha}{f_V^2} \cdot \sigma_{Vp}, \tag{1.26}$$

where $4\pi\alpha/f_V^2$ is the coupling constant of the photon to the vector meson V which describes the probability for finding a photon in the state of the vector meson V. The coupling constants can be derived from meson decay experiments.

QCD calculations, however, gave significant modifications to the VDM predictions which are visible in hard (high-$p_\perp$) interactions at HERA energies. In hard photoproduction, scattering processes between partons of the photon and the proton occur. For the description of such interactions a set of parton distributions was attributed to the photon in analogy to the structure functions of the proton.

If the nearly on-shell photon couples directly, electromagnetically, to the quark taking part in the hard subprocess, then the process is referred to as a direct interaction. If the photon interacts hadronically then the process is termed resolved.
The direct processes shown in figure 1.5 are characteristic for the photon-proton collisions, they do not exist in hadron-proton reactions.

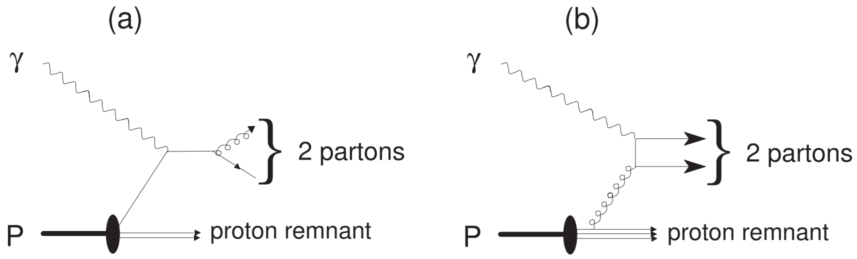

Figure 1.5: *Direct γp processes in leading order QCD: a.) QCD-"Compton"-process, b.) photon-gluon fusion.*

Indeed, the resolved photon is not completely described by the VDM. In addition to fluctuations into a vector meson, the photon can split into a $q\bar{q}$ pair without the formation of a bound hadronic state. This leads to an additional structure of the photon which is referred to as the anomalous part of the photon. Two examples of resolved γp processes are shown in figure 1.6. The most obvious and experimentally best accessible criterion to distinguish between both manifestations of the quasi real photon is the hadronic photon remnant which exists for resolved processes only, but not for direct interactions. However, the photon remnant is not only interesting as a discriminator between direct and resolved processes, but it is also of interest by itself since its transverse momentum is related to the intrinsic "primordial" transverse momentum $k_\perp$ of the partons inside the photon.

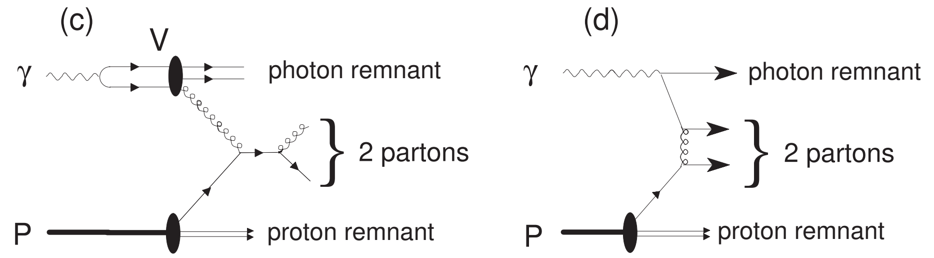

Figure 1.6: *Examples for resolved γp processes in leading order QCD. c.) VDM d.) anomalous.*

In low-$p_\perp$ processes, covered by the VDM and partly calculable by perturbative QCD, the transverse momentum of the initiator parton may have, due to its Fermi motion, an intrinsic "primordial" transverse momentum $k_\perp$ of a few hundred MeV/c, which has to be compensated by the photon remnant. In anomalous processes, where the photon remnant is represented by just a single parton, the transverse momentum $p_\perp$ of the remnant is related to the virtuality of the initial $\gamma \to q\bar{q}$ fluctuation.

The resolved and direct picture of the photon is only valid at lowest order QCD. At higher orders an ambiguity arises since the partons cannot be uniquely related to the hard subprocess or the photon remnant.

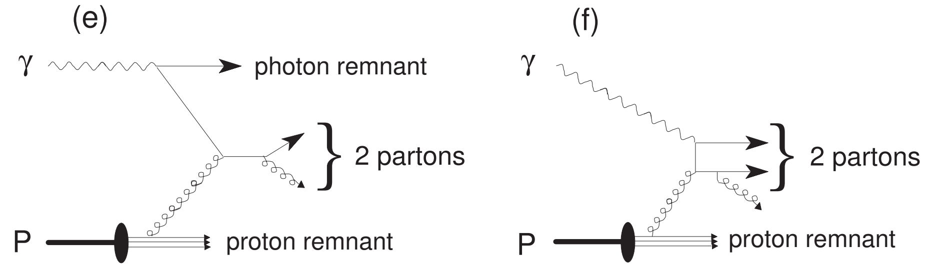

Figure 1.7: *Examples for resolved/direct γp process at higher order.*

Figure 1.7 illustrates the problem: both graphs are identical, nevertheless in (e) one quark of the photon is attributed to the photon remnant which characterises resolved processes. In (f), where both quarks of the photon take part in the hard interaction, the photon remnant is missing and thus, the process occurs as a direct one.

1.5 Monte Carlo Models

The picture of the photon as described above is implemented in the MC event generators PHOJET (version 1.04) [ENG95] and PYTHIA (version 5.722) [SJO94]. These have both been shown to describe photoproduction data in previous H1 analyses, e.g. [ABT94, ADL98].

The treatment of the photon in both models can be summarized as follows: the photon is represented by

$$|\gamma\rangle \;=\; \sqrt{Z}\,|\gamma_B\rangle + \sum_{V=\rho^0,\omega,\phi,J/\psi} \frac{e}{f_V}|V\rangle + \frac{e}{f_{q\bar{q}}}\,|q\bar{q}\rangle, \tag{1.27}$$

a superposition of three possible photon states:

- The "bare" state $|\gamma_B\rangle$ wherein the photon interacts directly with a parton of the proton. This process can be calculated in perturbative QCD where no photon structure function is involved (see figure 1.5).
- The photon fluctuated into a vector meson $|V\rangle$, predominantly a ρ^0. In this state the photon undergoes interactions well known from hadron-hadron scattering processes, leading to elastic, diffractive, low $p_\perp$ and high $p_\perp$ events. In the context of γp interactions these types of events are described by the VDM. For the description of the hard contribution in the VDM model, a photon structure function is defined which allows hard parton scattering processes within the photon leading to jets[1] and leaving a photon remnant behind.
- The $|q\bar{q}\rangle$ state describes the photon fluctuated into a $q\bar{q}$ pair of a virtuality larger than in the VDM state. Interactions with the photon in this state give rise to a "anomalous" structure function which is calculable in the framework of perturbative QCD. In "anomalous" events, the struck quark (antiquark) leads to a high $p_\perp$ jet while the remaining antiquark (quark) plays the role of the photon remnant.

The parameter Z in formula 1.27 is defined as

$$Z \;=\; 1 - \sum_{V=\rho^0,\omega,\phi} \left(\frac{e}{f_V}\right)^2 - \left(\frac{e}{f_{q\bar{q}}}\right)^2 \tag{1.28}$$

where the factors $(e/f_i)^2$ give the probability for finding the photon in the corresponding state i, with $i = (V, q\bar{q})$

Beside the same treatment of the photon, both generators, PHOJET and PYTHIA, also share the leading order (LO) approximation for QCD matrix elements describing the hard scattering subprocess (Λ_{QCD} = 200 MeV). The renormalization and factorization scales are set to $p_\perp$, the transverse momentum of the partons emerging from the hard scattering process. Since the leading order QCD calculation of a single hard parton cross section σ_{hard} diverges roughly like $\mathrm{d}p_\perp^2/p_\perp^4$, σ_{hard} is divergent for $p_\perp \to 0$. Thus a lower cut-off has to be applied which was chosen to be 2 GeV/c.
Initial and final parton radiation and the LUND [AND80] fragmentation model are included as implemented in the JETSET [SJO87] program.
The programs differ in the treatment of multiple interactions and the transition from hard to soft processes at low transverse momentum.

[1] Jets are collimated particle bundles scattered into the direction of the struck quark.

The **PHOJET** event generator simulates all components that contribute to the total photoproduction cross section. It is based on the two-component parton model (for a review, see [CAP94]). PHOJET incorporates detailed simulations of soft and hard parton interactions which are connected via an unitarization scheme.

The **PYTHIA** event generator uses QCD calculations in leading order for the primary parton scattering process and for multiple parton interactions. The latter are considered to result from the photon and proton remnants. Also PYTHIA models both hard and soft hadronic interactions, applying a unitarization scheme [SCH93].

Additional transverse momentum is generated in PYTHIA making use of the assumed intrinsic (primordial) $k_\perp$ distribution of the partons in the interacting hadrons. PYTHIA offers three possibilities to parameterise the $k_\perp$ distribution which are displayed in figure 1.8: a Gaussian, an exponential and a power law function of the form $1/(k_\perp^2 + k_{\perp,0}^2)$.

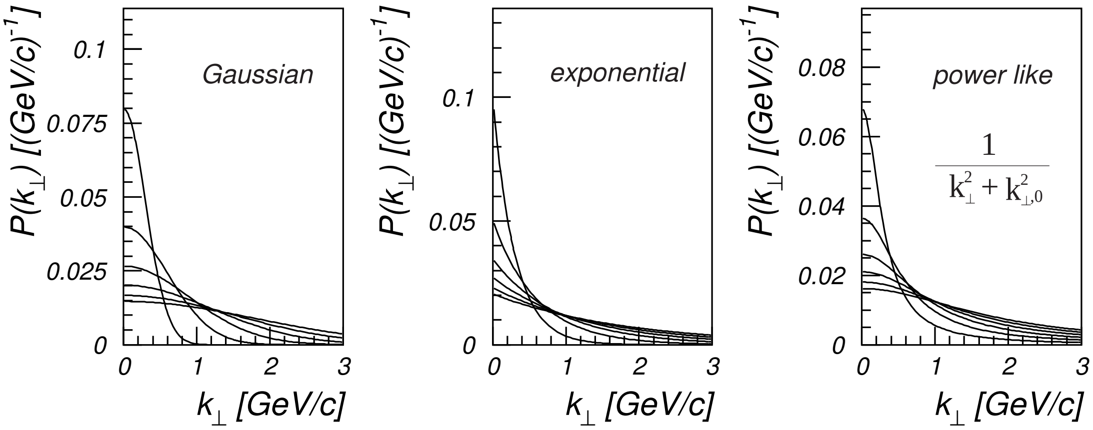

Figure 1.8: *Three assumptions on the primordial $k_\perp$ distributions of the photon remnant: a Gaussian, an exponential and a power law distribution. The width of the distributions increases from 0.3 GeV/c to 1.8 GeV/c in steps of 0.3 GeV/c.*

In both PHOJET and PYTHIA GRV-LO parametrisations are used for the parton distributions of the photon and the proton [GLU92].

1.6 Results from HERA

In the first five years of HERA operation the direct and resolved components of the photon have been extensively studied by the H1 and ZEUS Collaborations. A review of the results is given in [ERD97]. These studies have mainly been done via the analyses of jets, but also the inclusive production of charged particles gave instructive information on the hard parton-parton scattering processes which should lead to large transverse momenta of the produced particles. Out of the variety of results which were gained on the photon structure, only the two most relevant measurements for the analysis presented here are described. The first measurement is concerned with the observation of hard scattering processes at HERA energies via the inclusive spectra of charged particles, while the second one focuses on the characteristics of the photon remnant.

Inclusive Charged Particle Spectra

The aim of the inclusive charged particle measurement by the H1 Collaboration, based on the data of 1992, was to confirm the picture of the photon as described above. To this end the inclusive charged particle distribution, measured in γp collisions at HERA, was compared with corresponding distributions from hadron-hadron collisions. Since both the direct and anomalous component are absent in hadron-hadron interactions, deviations between hadron-proton and γ-proton collisions were expected. Figure 1.9 shows the result: the full points are the H1 data measured at a CM energy $\sqrt{s_{\gamma p}} \approx 200$ GeV within the kinematical range $|\eta| < 1.5$, $Q^2 < 0.01$ GeV^2 and $0.3 < y < 0.7$ with η, Q^2 and y_{B} denoting the pseudo-rapidity of the charged particles, the virtuality of the exchanged boson and the fractional energy transfer of the electron to the "quasi-real" photon. The open diamonds in the figure depict the cross section measurement of the UA1-Collaboration at the CERN $p\bar{p}$ collider at $\sqrt{s} = 200$ GeV in the rapidity region $y < |2.5|$. For comparison the UA1 data points were normalised to the H1 point at $p_\perp = 1.5$ GeV/c. In the $p_\perp$ range below 2 GeV/c the data agree quite well, which demonstrates the similarity between photon-proton and hadron-hadron interactions as expected from the VDM. However, clear differences in the higher $p_\perp$ range are visible, where the γp spectrum is obviously harder than the $p\bar{p}$ data.

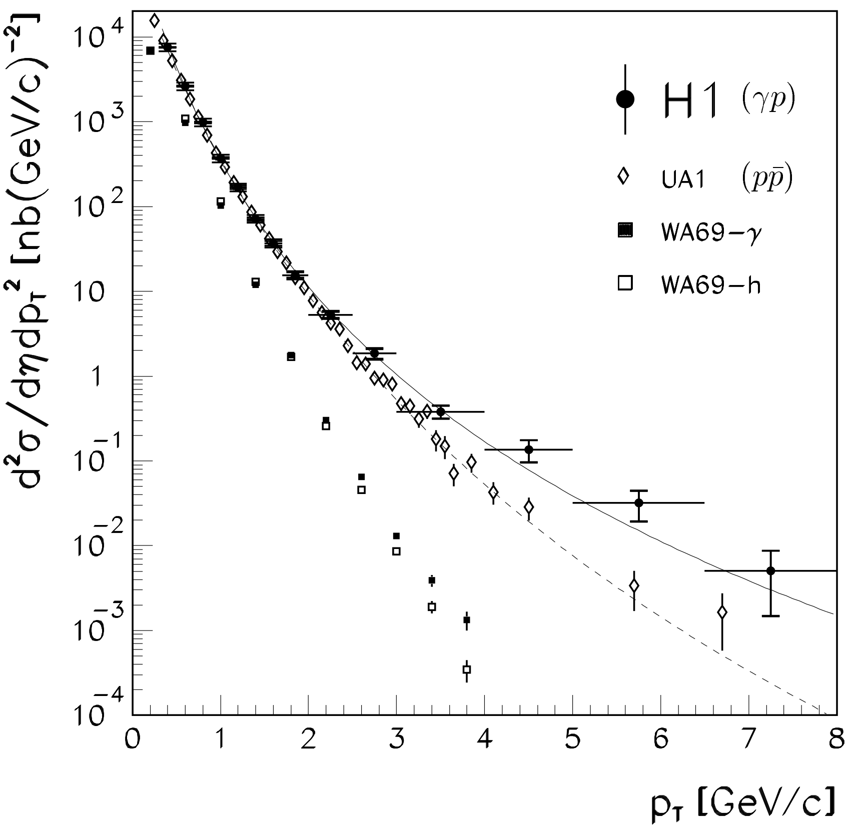

Figure 1.9: *The inclusive double differential charged particle cross section $d^2\sigma/d\eta\, dp_\perp^2$ as a function of the particles transverse momenta $p_\perp$, measured by the H1 Collaboration (full points) in the pseudo-rapidity range $|\eta| < 1.5$. The solid (dashed) line is the result of a power law fit (equation 1.29) to the H1 (UA1) data (see text).*

To quantify this effect the data were fitted with the following QCD inspired power-law:

$$E \cdot \frac{\mathrm{d}^3\sigma}{\mathrm{d}p^3} = A \cdot \left(1 + \frac{p_\perp}{(p_\perp)_0}\right)^{-n} \tag{1.29}$$

which yielded for the UA1 data (dashed line): $(p_\perp)_0 = (1.8 \pm 0.1)$ GeV/c and $n = 12.14 \pm 0.39$ and for the H1 spectrum (solid line): $(p_\perp)_0 = (0.63 \pm 0.20)$ GeV/c and $n = 7.1 \pm 0.2$ [2]. The differences between photon-proton and hadron-proton scattering are further illustrated by the results of the WA69 Collaboration, which measured charged particle cross sections with real photon and hadron beams at CM energies around 18 GeV. The results of the WA69 Collaboration are marked in figure 1.9 by the full and empty squares. The comparison of the data at small and large CM energies result in two observations:

- the γp data have a more pronounced tail at large transverse momenta than the hadron-hadron spectra
- with increasing CM energy both γ-proton and hadron-proton spectra harden

Also, the ZEUS Collaboration performed a similar measurement which is in agreement with the H1 data [DE95a].

Study of the Photon Remnant

The second measurement, performed by the ZEUS Collaboration with the data collected during the 1993 data-taking period, studied the properties of the photon remnant in resolved hard photoproduction events [DE95b]. As illustrated in figure 1.6 resolved hard photoproduction events have a final state which includes two high-$p_\perp$ jets from the hard scattering process as well as a photon and a proton remnant. Using a jet finding algorithm, optimised for this photon remnant analysis, events containing two high-$p_\perp$ jets with $p_\perp > 5$ GeV/c in the pseudo-rapidity region $\eta < 1.6$ were selected. The latter cut on the pseudo-rapidity of the jets ensures that the jets are well separated from the proton remnant in the forward region. For the separation of resolved and direct processes the additional cuts, $E_3 > 2$ GeV and $\eta_3 < -1$, on the energy and pseudo-rapidity of the third low-$p_\perp$ jet, associated to the photon remnant, were required. MC studies showed that, after applying all cuts, 97 % of the selected events could be correctly attributed to resolved hard photoproduction processes. The result of this measurement is displayed in figure 1.10. The two upper plots show the pseudo-rapidity and the transverse momentum of the third jet, corrected for all detector effects, while the corresponding energy distribution is depicted in the plot below. The data are compared with predictions of the Monte Carlo model PYTHIA with different assumptions on the initial transverse momentum $k_\perp$ of the photon. The solid line is the PYTHIA prediction with the default option: an exponential distribution $\mathrm{d}N/\mathrm{d}{k_\perp}^2 \propto e^{-k_\perp^2/k_{\perp,0}^2}$ with $k_{\perp,0} = 0.44$ GeV/c. The description of the data shown is clearly improved by choosing the harder intrinsic $k_\perp$ spectrum of the form $\mathrm{d}N/\mathrm{d}{k_\perp}^2 \propto 1/(k_\perp^2 + k_{\perp,0}^2)$ (see figure 1.8), with $k_{\perp,0} = (0.66 \pm 0.22)$ GeV/c (dashed line in figure 1.10). A comparably good description was also found for the exponential distribution with $k_{\perp,0} = (1.90 \pm 0.21)$ GeV/c.

[2] In ref. [ABT94] the error on the power n is erroneously quoted as 2.0

The analysis presented here tries to supply additional information to the results gained by the two measurements described above. In contrast to the inclusive charged particle measurement in the pseudo-rapidity range $|\eta| < 1.5$, this measurement studies the π^0 and η meson photoproduction in the much more extended rapidity region $-3.5 < y < 1.5$. The $p_\perp$ values of the mesons considered reach values up to 2 GeV/c, thus the onset of hard scattering, according to figure 1.9, should be visible. Since the very backward region can be associated with the photon remnant the meson production is expected to be sensitive to the initial $k_\perp$ of the photon.

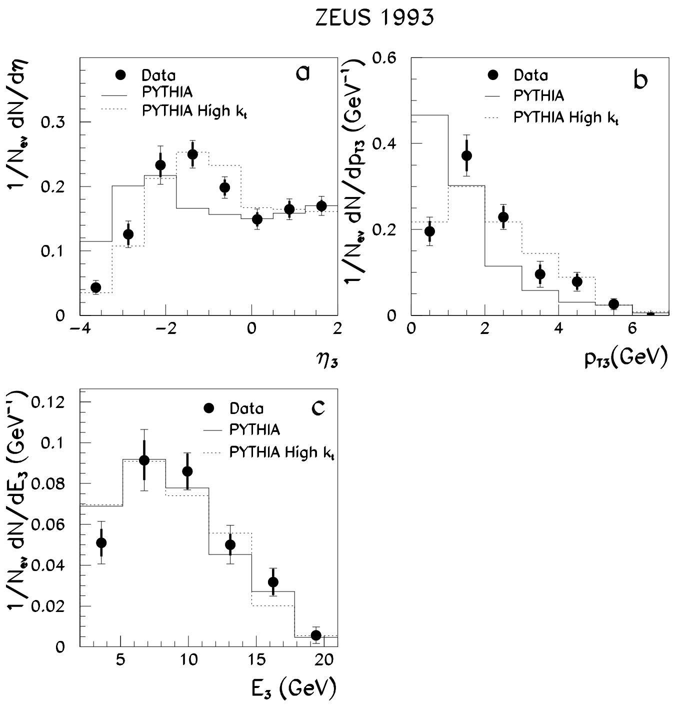

Figure 1.10: *(a) Pseudo-rapidity of the third jet corrected back to hadron level. (b) Corrected $p_\perp$ distribution (c) Corrected energy distribution. In (b) and (c) the cut η < -1 is applied. The solid line represents the prediction of PYTHIA assuming a Gaussian distribution of the initial $k_\perp$ while the dotted line shows the prediction of PYTHIA according to a power like initial $k_\perp$ distribution with k_0 = 0.66 GeV/c.*

1.7 The Kinematical Region Accessible for π^0 and η Mesons

In this section an overview of the (kinematical) properties of the π^0 and η mesons at HERA is given.

Charged pions, the long awaited Yukawa particles, were detected already in 1947 by Powell, Lattes and Occhialini in cosmic rays with the help of the nuclear emulsion technique. A few years later, in 1950, the neutral pion was also found in cosmic rays. The neutral pions have a mass of 135 MeV/c^2 and decay electromagnetically into two photons with a branching ratio of 99 %. In the static quark model of hadrons, mesons are bound quark and antiquark states. Taking the u-, d and s-quark and the corresponding antiquarks into account, one obtains nine quark combinations: a singlet state, symmetric under SU(3) transformations, and eight states (octet), which can be transformed into one another by the exchange of the u, d and s quarks. In this model the pions, consisting only of u- and d-quarks, are attributed to the octet and described by

$$\begin{array}{lll} (\pi^+) \quad |I=1, I_3=1\rangle & = & -u\bar{d} \\ (\pi^0) \quad |I=1, I_3=0\rangle & = & \sqrt{\frac{1}{2}}\left(u\bar{u} - d\bar{d}\right) \\ (\pi^-) \quad |I=1, I_3=-1\rangle & = & d\bar{u} \end{array}$$

where I denotes the Isospin and I_3 its third component. One member of the octet state, labelled η_8, is orthogonal to η_0, the singlet state, which are given by:

$$\begin{array}{lll} |\eta_0\rangle & = & \sqrt{\frac{1}{3}} \cdot (|u\bar{u}\rangle + |d\bar{d}\rangle + |s\bar{s}\rangle) \\ |\eta_8\rangle & = & \sqrt{\frac{1}{6}} \cdot (|u\bar{u}\rangle + |d\bar{d}\rangle - 2 \cdot |s\bar{s}\rangle) \end{array}$$

with $\langle\eta_0|\eta_8\rangle = 0$. However, the states observed in nature, η and η', appear to be linear combinations of the wave functions η_0 and η_8:

$$\begin{aligned} |\eta\rangle &= |\eta_0\rangle \sin\theta + |\eta_8\rangle \cos\theta \\ |\eta'\rangle &= |\eta_0\rangle \cos\theta - |\eta_8\rangle \sin\theta \end{aligned} \tag{1.30}$$

with a mixing angle $\theta \approx 11^\circ$. The η has a mass of 548 MeV/c^2 and decays also into two photons with a branching ratio of 38.8 %. Since the wave function of these mesons have $J = 0$ and odd parity they are called *pseudo-scalar mesons*.
The kinematical range accessible at HERA for the π^0 and η mesons was studied with the MC generator PYTHIA. For this purpose about 200000 events were produced within the y-range $0.3 < y < 0.7$ which corresponds to a γp CM energy ranging from 165 GeV to 251 GeV. The results are displayed in figure 1.11.

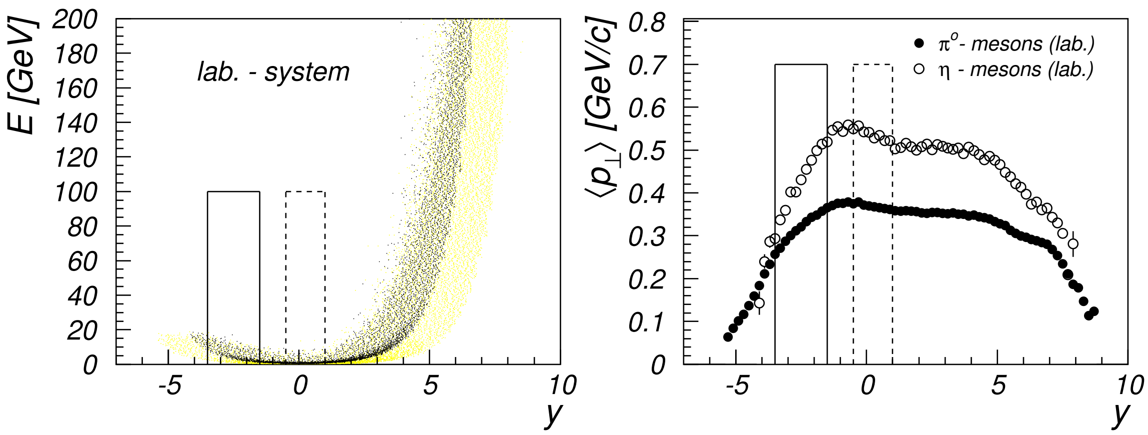

Figure 1.11: *Kinematical range accessible for π^0 and η mesons at HERA. Left side: The π^0 and η energies versus their laboratory rapidities. The gray points refer to the π^0 and the black points to the η mesons. Both, the η and π^0-meson reach energies up to 820 GeV (= beam energy of incoming protons) in the forward direction. Right side: The mean transverse momenta of the π^0 (full points) and η mesons (circles) as a function of their lab. rapidities. The kinematical range within the boxes is investigated by this analysis.*

The left plot shows the π^0 and η energies versus their laboratory rapidities y. In the forward direction ($y > 2$) the neutral mesons can reach energies up to values of 820 GeV, corresponding to the energy of the incoming protons. The maximal energy accessible for the particles, scattered into the direction of the incoming photons, is around 19 GeV. The mean transverse momenta of the π^0 and η mesons as a function of their laboratory rapidity can be seen in the right plot of figure 1.11. The mean $p_\perp$ of the η mesons is larger by roughly a factor 1.5 than the mean $p_\perp$ of the π^0s. In order to demonstrate the large effects of the asymmetric energies of the incoming particles on the π^0 and η quantities, a variable transformation via formula 1.31 from the laboratory system into the γp CMS was performed. With the four-vector $p = (E, \boldsymbol{p})$ (lab system) and the relative velocity β_f of both systems, the corresponding quantities $(E^\star, \boldsymbol{p}^\star)$ in the γp CMS are given by

$$\begin{pmatrix} E^\star \\ p^\star_{\|} \end{pmatrix} = \begin{pmatrix} \gamma_f & -\gamma_f\beta_f \\ -\gamma_f\beta_f & \gamma_f \end{pmatrix} \begin{pmatrix} E \\ p_{\|} \end{pmatrix}, \quad p^\star_\perp = p_\perp, \tag{1.31}$$

where $\gamma_f = (1 - \beta_f^2)^{-1/2}$ and $p_\perp$ ($p_{\|}$) the components perpendicular (parallel) to β_f. The relative velocity β_f was calculated by: $\beta_f = (E_P - E_\gamma)/(E_P + E_\gamma)$, where E_P and E_γ denote the beam energies of the proton and photon respectively.

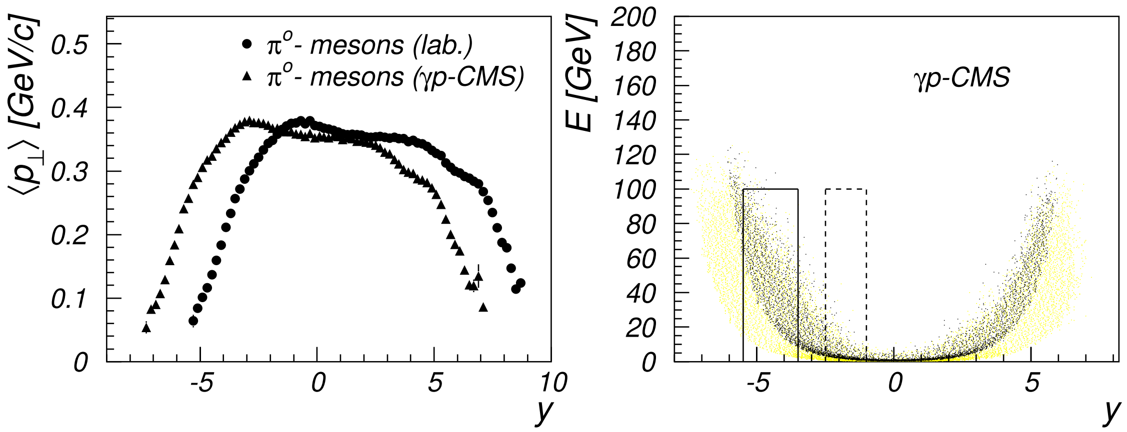

Figure 1.12: *Kinematical range accessible for π^0 and η mesons at HERA in the γp CMS. The gray points refer to the π^0s and the black points to the ηs. The kinematical range within the boxes is studied by this analysis.*

The mean transverse momenta of the π^0s as a function of their rapidities in the γp CMS can be seen in figure 1.12 (left plot). The shape of this distribution is, as expected, unchanged but the rapidity values are shifted by about two units (in the negative direction) in the γp CM system with respect to the laboratory frame. In order to explain this shift by about two units, one can subdivide the problem into two parts:

- the difference between the *ep* and the laboratory system and
- the difference between the *ep* and the γp system.

The rapidity difference for two systems, moving with the velocity β with respect to each other, is $\Delta y = \tanh^{-1}(\beta)$. This yields for the movement between the laboratory system

and the ep CMS $(\Delta y)_{ep-\text{lab.}} = 1.7$. With the mean value of 0.46 for the range $0.3 < y_{\mathrm{B}} < 0.7$, the rapidity difference between the ep- and the γp CMS yields $(\Delta y)_{ep-\gamma p} = 0.39$. The sum of both rapidity differences $\Delta y = (\Delta y)_{ep-\text{lab.}} + (\Delta y)_{ep-\gamma p} = 2.09$ explains the difference seen in the rapidity spectra above.
In the γp CMS the energies of the π^0 and η mesons are more or less symmetric and range up to values of 126 GeV, half of the γp CM energy.

Chapter 2

The *ep* Collider HERA

The first lepton–proton collider HERA[1] was set up at DESY (Hamburg, Germany) in 1992. The CM energies, reached by HERA, are one order of magnitude above those of previous fixed–target–experiments, thus allowing to study *ep* (γp) interactions at an *ep* (γp) center of mass energy around 300 (200) GeV.

In the accelerator complex, sketched in figure 2.1, protons and electrons run in bunches of $10^{10} - 10^{11}$ particles through a system of several pre–accelerators (PIA, DESY II/III, PETRA) to be finally injected into the two main accelerators of the HERA ring with energies of 40 GeV and 12 GeV, respectively.

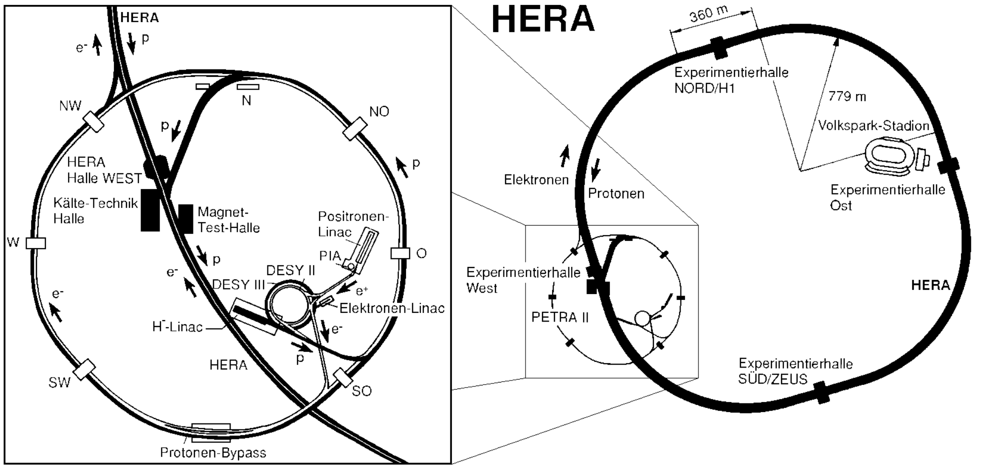

Figure 2.1: *Schematic overview of the HERA accelerator complex*

In separate storage rings for protons and electrons, with circumferences of 6.3 km, the collision partners are accelerated to their final energies. During the data taking periods the final energy of the protons amount to 820 GeV and the final energy of the positrons is 27.6 GeV, resulting in an *ep* center of mass energy of 300 GeV. The large asymmetry of the collision partners reflects the balance of the need of a high center of mass energy at minimal synchrotron radiation losses of the electron beam. Conventional magnet technology is used for the electron ring whereas superconducting magnets are needed for the

[1] Hadron–Elektron–Ring–Anlage (HERA)

bending fields in the proton ring. In principle a maximum of 210 bunches of protons and electrons can be filled, separated from each other by 96 ns. For the purpose of controlling the background rate, 10 of the electron (proton) bunches are filled without the corresponding proton (electron) bunches. The interaction region is determined by the length of the proton bunches showing approximately a Gaussian distributions with a width $\sigma \approx 11$ cm.

The integrated luminosity produced by HERA in 1996 is shown by the dashed line in figure 2.2, the solid line depicts the integrated luminosity recorded by the H1 experiment.

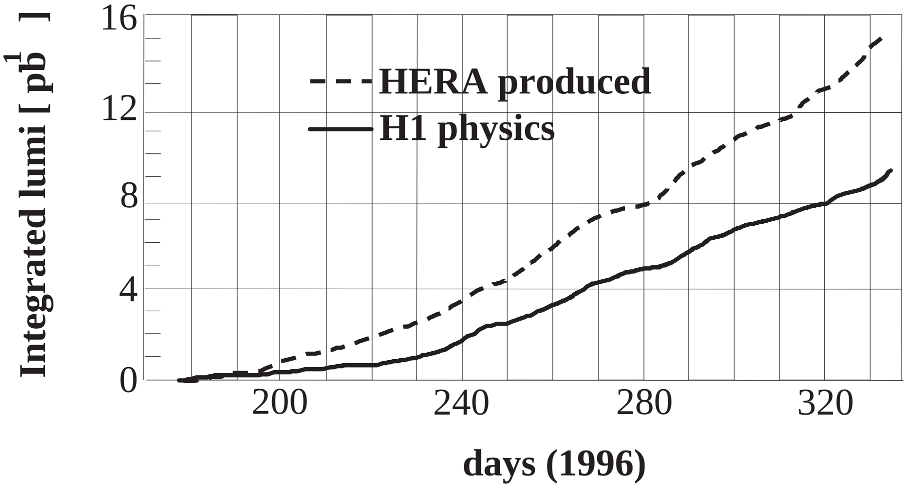

Figure 2.2: *Integrated luminosity versus the days of the year 1996. Dashed line: integrated luminosity produced by the HERA machine. Solid line: integrated luminosity collected by the H1 experiment.*

Chapter 3

The Detector H1

A detailed description of the H1 detector is given in Ref. [ABT97], figure 3.1 shows the H1 detector with its main devices listed in the legend of the figure. This chapter describes the components of the H1 detector used in the analysis which relies mainly on the H1 backward calorimeter "SpaCal" $\boxed{12}$ and the Liquid Argon calorimeter LAr $\boxed{4}$, $\boxed{5}$. In addition, the central tracking detectors $\boxed{2}$ were used for measuring the interaction vertex position and for identifying isolated electromagnetic clusters in the LAr calorimeter. Photoproduction events were selected with the help of the electron detector (not shown if figure 3.1).

3.1 The SpaCal

The SpaCal is a lead-scintillating fibre calorimeter which covers the backward region of the H1 detector, namely the polar angular range $153^\circ \leq \theta \leq 178^\circ$, where θ is determined with respect to the proton beam direction at the nominal electron proton interaction point. For pions, this corresponds to a rapidity range of $-3.5 < y < -1.4$. The location of the SpaCal in the H1 experiment is shown in figure 3.2. It is separated into an electromagnetic (EM) and a hadronic section of equal size. The EM section consists of 1192 cells with a cross section of 40.5×40.5 mm^2, each read out by a photomultiplier tube. The active volume of this part has a lead-to-fibre ratio of 2.3:1 and a depth of 27 radiation lengths (250 mm). The remaining energy leakage is negligible for electrons with energies up to values of 30 GeV. The small cell cross section results in a Molière radius of 25.5 mm and ensures a good position resolution as well as a good electron-pion separation. The hadronic section is designed in complete analogy to the electromagnetic one. It consists of 128 cells with a cross section of 120×120 mm^2 and a lead-to-fibre ratio of 3.4:1 The EM and the hadronic section each have a depth corresponding to one hadronic interaction length. A complete description of the SpaCal and of its performance is given in [APP96, APP97, NIC96].
The energy resolution of the EM SpaCal section for electromagnetically interacting particles is

$$\frac{\sigma(E)}{E} = \frac{0.075}{\sqrt{E/\,\mathrm{GeV}}} \oplus 0.010, \tag{3.1}$$

where E is the energy deposited in the SpaCal by an electromagnetically interacting particle.

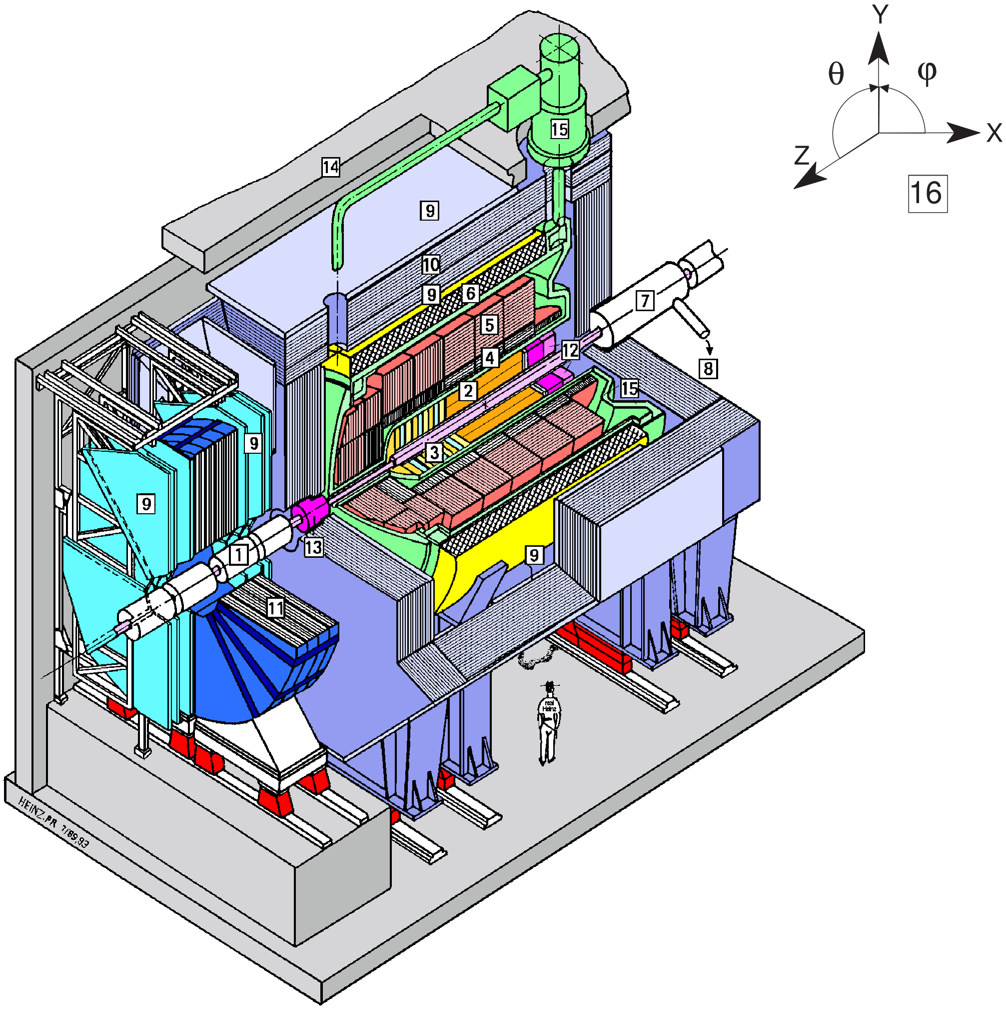

1	Beam pipe and beam magnets	8	Helium supply for 7
2	Central track detectors	9	Muon chambers
3	Forward track detectors	10	Instrumented iron yoke
4	Electromagnetic LAr calorimeter	11	Forward muon toroid
5	Hadronic LAr calorimeter	12	SPACAL and Backward DC
6	Superconducting coil (1.15 T)	13	Plug calorimeter
7	Compensating magnet	14	Concrete shielding
		15	Liquid argon cryostat
		16	H1 coordinate system

Figure 3.1: *An isometric view of the H1 detector at HERA.*

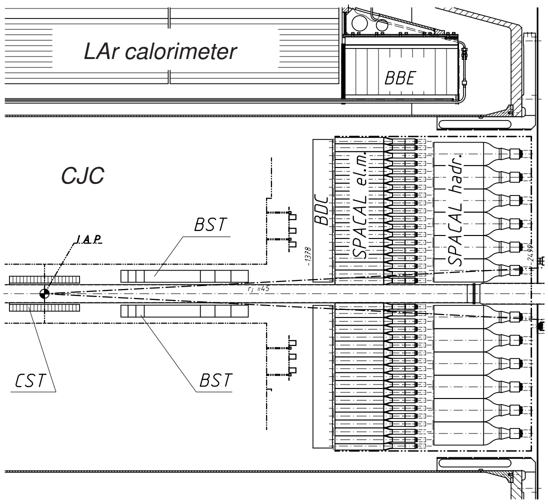

Figure 3.2: *A side view of the backward region of the H1 detector.*

The absolute energy scale, in the lower energy range from 0.2 GeV to 10 GeV, is known with an uncertainty of 4 % while in the energy region above the precision of the calibration is at the 1 % level. The resolution in θ is better than 2.5 mrad above 1 GeV. The spatial and energy resolution capabilities of the calorimeters transform directly into the accuracy of the mass determination for the π^0 mesons.

In addition to the energy and spatial information the excellent time resolution of 2 ns of the SpaCal is used to provide time-of-flight information of the energy deposition in this calorimeter for both the electromagnetic and hadronic section. A time-of-flight (ToF) window is defined in which particles from the *ep*-interaction are expected to hit the SpaCal. Events outside this window (AToF) are rejected as background. Table 3.1 summarizes the main characteristics of the SpaCal.

parameter	**electromagnetic section**	**hadronic section**
Number of cells	1192	128
cross section	$40.5 \times 40.5\ mm^2$	$120 \times 120\ mm^2$
fibre diameter	0.5 mm	1.0 mm
lead-to-fibre ration	2 : 1	4 : 1
interaction length	25 cm	24.6 cm
radiation length X_0	0.91 cm	0.85 cm
Molière radius	2.55 cm	2.45 cm
energy resolution $\frac{\sigma}{E}$	$\frac{(7.5\pm0.2)\ \%}{\sqrt{E/GeV}} \oplus (1.0 \pm 0.1)\ \%$	$(56.0 \pm 3.0)\ \%$
spatial resolution σ	$\frac{(4.4\pm0.4)\ mm}{\sqrt{E/GeV}} + (1.0 \pm 0.2)\ mm$	-
angular resolution	≤ 2 mrad	-
time resolution	(0.38 ± 0.03) ns	≤ 1 ns

Table 3.1: *SpaCal parameters.*

3.2 The Liquid Argon Calorimeter

The main calorimeter of the H1 experiment is the Liquid Argon (LAr) sampling calorimeter. It covers the forward and central regions, e.g. a polar angular range from 4° to 154°. A side view of the LAr calorimeter is displayed in figure 3.3.

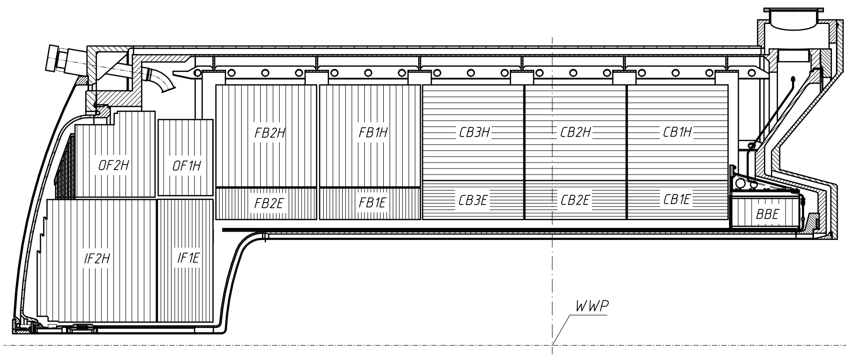

Figure 3.3: *A side view of the Liquid Argon calorimeter.*

Along the beam line the calorimeter is subdivided into eight "wheels", which consist of an inner electromagnetic and an outer hadronic section. The exception is the BBE wheel which has only an electromagnetic section. Each of the six barrel wheels is segmented in ϕ by eight identical octants. The two forward wheels (left side of figure 3.3) are assembled as two half rings. The wheels and octants have been arranged in such a way that energy losses due to passive material between the wheels and octants, so called cracks, are minimal. The electromagnetic part of the calorimeter consists of lead absorber plates (2.4 mm thick) with layers of liquid argon (2.35 mm thick) as active material between them. The total thickness varies between 20 and 30 radiation lengths.
The hadronic part consists of 19 mm stainless steel absorber plates with a double gap of 2.4 mm liquid argon, corresponding to an hadronic interaction length between 4.5 and 8. The total number of readout cells is about 45000, with a size varying between 10 and 100 cm^2. The finest granularity can be found in the forward region with typical cell sizes of 3.5 x 3.5 cm^2 while in the more central and backward regions the cell size reaches values up to 100 cm^2, a clear disadvantage for the reconstruction of π^0s in this region compared to the high granularity in the forward region or compared to the high granularity of the SpaCal. The resolution of the LAr EM section is

$$\frac{\sigma(E)}{E} \approx \frac{0.12}{\sqrt{E/\,\mathrm{GeV}}} \oplus 0.01, \tag{3.2}$$

as measured in test beams [AND94]. The LAr absolute energy scale, in the low energy range from 0.6 GeV to 10 GeV, is known at the 4% level, as shown in the present analysis. The LAr calorimeter is used to extend the kinematical range of reconstructed π^0s towards the forward region, namely up to laboratory frame rapidities of +1.5.

3.3 The Central Tracking System

The H1 tracking system is designed to measure the momenta and scattering angles of charged particles. The information supplied allows to determine the interaction point of the event (vertex) and the reconstruction of secondary vertices caused by the decay of long lived particles. Moreover, the tracking system allows to identify particles via their specific energy loss (dE/dx). The H1 tracking system is made of three major devices, the forward, central and backward trackers. The forward tracking system covers the polar angular range θ from 5° to 25°, the central one from 15° to 165° and the backward drift chamber (BDC) extends the angular measurement over the range 155° to 178°. The present analysis made mainly use of the central tracking system to reconstruct the event vertex. A side view of the H1 tracking system is presented in figure 3.4.

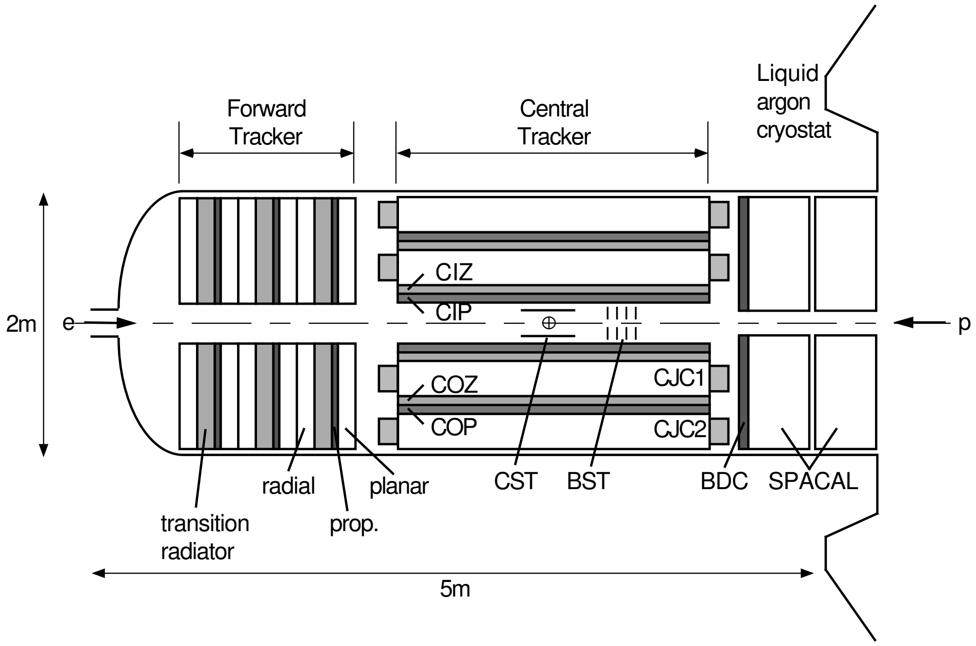

Figure 3.4: *A side view of the H1 tracking system.*

The large concentric drift chambers CJC1 and CJC2 are the basis for the track reconstruction in the central region. They have an active length of 2200 mm and consist of 30 (60) cells with 24 (32) sense wires, respectively, mounted in parallel to the z-axis. The magnetic field of 1.15 T is created by a superconducting cylindrical coil with a diameter of 6 m and a length of 5.75 m enclosing the main calorimeter. The passing time of high-$p_\perp$ particles, crossing CJC1 and CJC2, can be measured for each chamber with an accuracy of 0.5 ns, thus allowing to separate tracks from different bunch crossings. The spatial resolution in the $r\phi$-plane is 170 μm. The z-coordinate can be determined with a resolution of one percent of the wire length by comparing signals read out at both wire ends.
The determination of the z-coordinate of the particles can be improved with the help of the central (inner and outer) z-chambers CIZ and COZ with wires perpendicular to the beam direction. The CIZ is divided into 15 drift cells, the COZ into 24 cells with four sense wires per cell in both cases. With these devices the z-coordinate of a particle can be measured with an accuracy $\sigma = 0.26$ mm.
The central proportional chambers CIP and COP are Multi-Wire Proportional Chambers (MWPC) mounted within and between the CIZ. They provide a fast timing signal with

a resolution of 21 ns thus allowing, in connection with the time information of the forward tracking system, to trigger on charged particles originating at the interaction vertex.

The purpose of the Backward Drift Chamber BDC, directly mounted in front of the SpaCal, is the measurement of the backward scattered electron. This information is used for the identification of deep inelastic scattering events and the determination of their kinematical quantities. It consists of four double layers of drift cells allowing to reconstruct the tracks from at maximum eight space points. In order to increase the sensitivity of the ϕ measurement and to avoid insensitive regions like the cell boundary the layers are rotated by 11.25 degrees with respect to each other. To resolve the left-right ambiguity the layers are shifted by half a cell width in radial direction. With the BDC the polar angle of the scattered electron can be measured with an accuracy of about 0.8 mrad.

3.4 The Time-of-Flight (ToF) Systems

The time of flight (ToF) system consists of scintillators situated at several positions along the beam pipe. The forward ToF is located at z = +7 m, the “Plug” ToF at z = +5.3 and the backward ToF at z = -3.2 m. Finally, to scintillator walls (“VETO WALLS”) are installed at z = -810 cm and z = -650 cm. Each of the scintillators has a very good time resolution of one ns, needed for fulfilling the task of the system: the rejection of proton induced background. The rejection is based on the precise time information of the bunch crossings supplied by the HERA machine. The respective position of the counters defines a time window in which particles from the nominal ep-interactions are expected to cross the scintillators. Background events will mostly occur outside the defined time interval.

3.5 Luminosity Measurement at H1

The luminosity $\mathcal{L}$ is defined through the relation

$$\dot{N} = \mathcal{L} \cdot \sigma. \tag{3.3}$$

N is the number of interactions per time unit for a process with the cross section σ. This definition implies the important role of the determination of $\mathcal{L}$ as each uncertainty here directly transforms into an uncertainty of the cross section measurement. At H1 the Bethe-Heitler process $ep \to e\gamma p$, which has a large and precisely calculable cross section, is used to determine the luminosity. The main source of background is due to bremsstrahlung from the residual rest-gas in the beam pipe, having completely the same signature as the Bethe-Heitler processes. This background is determined with the help of so called electron pilot bunches, e.g. bunches, which have no proton as colliding partner, more explicitly discussed in the next section 3.6. Figure 3.5 depicts the luminosity system of H1, consisting of an electron detector (ET) and a photon detector (PD). The **electron tagger** consists of a TlCl/TlBr crystal calorimeter with an energy resolution of $\sigma(E)/E = 0.22/\sqrt{E/\,\text{GeV}}$, located at z $= -33$ m. It accepts scattered electrons from photoproduction processes with energy fractions between 0.3 and 0.8 with respect to the incoming electron beam energy of 27.5 GeV, and scattering angles < 5 mrad with respect to the electron beam direction.

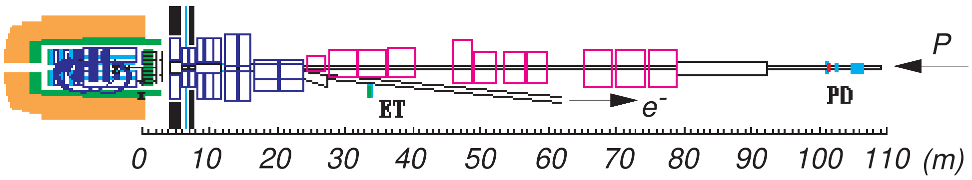

Figure 3.5: *The H1 luminosity system.*

The **photon detector**, also a TlCl/TlBr crystal calorimeter, is mounted at z = -102.9 m. Scattered electrons are deflected by a set of low-beta quadrupoles and a bending magnet before they pass an exit window at -z = 27.3 and hit the ET. The photons leave the proton beam pipe through the photon exit window at $-z$ = 92.3 m, where the proton beam pipe bends upward, before reaching the PD. A Pb (2.2 X_0) filter followed by a water Čerenkov counter (0.8 X_0), directly located in front of the PD, shields the detector from high synchroton radiation flux.

There are two methods available for measuring the luminosity: the coincidence mode requires the simultaneous detection of electrons and photons in the corresponding detectors. The luminosity is calculated as

$$\mathcal{L} = \frac{R_{\text{tot}} - (I_{\text{tot}}/I_0) \cdot R_0}{\sigma_{\text{vis.}}} \tag{3.4}$$

where R_{tot} is the total rate of the Bethe-Heitler events, R_0 is the rate in the electron pilot bunches, I_{tot}, I_0 are the corresponding electron beam currents and $\sigma_{\text{vis.}}$ is the visible part of the $ep \to e\gamma p$ cross section, corrected for acceptance and trigger efficiency of the whole luminosity system.
This mode is used for the online-determination of the luminosity allowing to optimise the beam optics during the steering phase of data taking.
The luminosity measurement is corrected offline in a detailed analysis for systematic effects of the luminosity system using the single photon method.

$$L = \int \mathcal{L} \cdot dt = \frac{N(E_\gamma > E_{\text{min}})}{\sigma(E_\gamma > E_{\text{min}})} \tag{3.5}$$

Here, $N(E_\gamma > E_{\text{min}})$ denotes the number of Bethe-Heitler events with the photon energy above a certain energy threshold (E_{min}), completely corrected for the acceptance and efficiency of the photon detector and after subtraction of the background events. $\sigma(E_\gamma > E_{\text{min}})$ denotes the corresponding cross section for this process. The advantage of the single photon method compared to the coincidence measurement is that this method is based on the photon detector only which is much less sensitive to changes in the electron beam optics.
In 1996 and 1997, the device delivered a luminosity determination with an uncertainty below 2%.

3.6 Determination of the Background due to Interactions of the Electrons with residual Gas in the Beam Pipe

Electron and proton beams at HERA consist at maximum of 200 “colliding bunches” and of 10 “pilot bunches” having no colliding partner. They serve for the estimation of background due to beam gas interactions.

The number of events for colliding bunches (N_{phys}) is determined via

$$N_{\text{phys}} = L \cdot \sigma_{\text{phys}} \, , \tag{3.6}$$

and the number for background events (N_{BG}) accordingly is

$$N_{\text{BG}} = L \cdot \sigma_{\text{BG}} \tag{3.7}$$

The number of pilot bunches (N_{pilot}) of the data sample is also proportional to σ_{BG} but with a value for the luminosity scaled down by the factor $NB_{\text{pilot}}/(NB_{\text{colliding}} + NB_{\text{pilot}})$, where $NB_{\text{colliding/pilot}}$ denotes the number of colliding and pilot bunches.

$$N_{\text{pilot}} = \frac{NB_{\text{pilot}}}{NB_{\text{colliding}} + NB_{\text{pilot}}} \cdot L \cdot \sigma_{\text{BG}} \tag{3.8}$$

Thus from 3.8 follows σ_{BG} as a function of NB_{pilot} and finally using 3.7:

$$N_{\text{BG}} = \frac{NB_{\text{colliding}} + NB_{\text{pilot}}}{NB_{\text{pilot}}} \cdot N_{\text{pilot}} \tag{3.9}$$

Assuming that all bunches contain nearly the same number of particles allows to write expression 3.9 as

$$N_{\text{BG}} = \frac{I_{\text{ebeam}} + I_{\text{pilot}}}{I_{\text{pilot}}} \cdot N_{\text{pilot}}, \tag{3.10}$$

where I_{ebeam} and I_{pilot} denote the current of the electron and pilot beam respectively.

3.7 The Triggering System of H1

The purpose of the triggering system is the selection of *ep*-interactions and the rejection of background. At HERA there are several sources of background:

- background induced by synchrotron radiation
- or by interactions of the incoming particles with residual beam gas or the beam wall
- muons from cosmic radiation
- and finally so called “Halo” muons, flying in parallel with the proton bunches, created via charged pion decay by interactions of the protons with rest gas particles in the beam pipe or the beam wall in front of the detector

At design-luminosity ($\mathcal{L} = 1.5 \cdot 10^{31}\,\mathrm{cm}^2\,\mathrm{s}^-1$) the rates of beam gas interactions are about 50 kHz, while the events of interest have rates reaching from few events per hour for charged current interactions via few Hz for deep inelastic scattering to roughly 30 Hz for photoproduction.
H1 is equipped with a multi-level triggering system, sketched in figure 3.6.

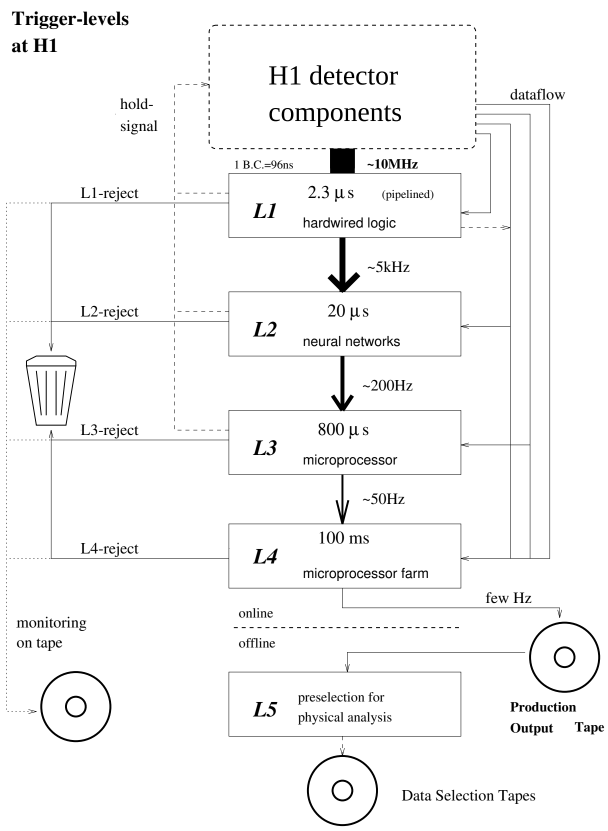

Figure 3.6: *The trigger levels at H1.*

The first trigger level L1 supplies a trigger decision already after 2.5 μs. Since the time interval between two consecutive bunch crossings is 96 ns at HERA, the full event information is stored in pipelines until the L1 decision is reached. Therefore, the trigger runs deadtime free on L1. At this level the trigger uses simple but fast information from most subdetectors of H1, for example the interaction vertex position or energy depositions with their topologies. A combination of different requirements on the information supplied by the subdetectors is called a **subtrigger** element. H1 allows 128 possibilities to combine certain detector information to a subtrigger. This analysis is mainly based on the $eTag$ and the IET trigger elements. The $eTag$ trigger fires if it records an energy deposition above a certain threshold in the electron detector located at $z = -33$ m. The inclusive electron trigger element IET is designed to recognise an electron from a deep-inelastic event if it is scattered by a large polar angle in the H1-coordinate-system and thus hits the SPACAL. The electromagnetic section of the backward calorimeter is divided into 320 so called trigger-windows, consisting of 4 x 4 neighbouring cells. The windows overlap to avoid efficiency gaps at the borders. In each window the energy recorded within the time-off-flight window is summed and compared by a discriminator to one of three possible energy thresholds. If the energy exceeds one of these thresholds the corresponding trigger bit is set. In 1996 and 1997 the IET trigger element was affected by the "Hot Spot", a small region, related to strong beam activity, located very close to the beam pipe. This activity caused high IET trigger rates, such that the region touched by the "Hot Spot" had to be excluded from the trigger logic. The information on which of the subtriggers accepted the event is fed into the data stream and thus accessible for the further data analysis. The decisions on trigger level L2 are based on the same information of the subdetectors as the decision on L1. In contrast to L1 more sophisticated algorithms are used by exploiting, for example, event topologies. The triggers of level L2 run in parallel to the readout of the detectors and need about 20 μs to take a decision. Subtrigger 50, used in this analysis, expects the L2 verification that the L1 triggering IET window has a minimal distance from the beam line of about 16 cm. The L2 condition included makes sure that the IET triggering condition on L1 is not affected by any problem connected with the "Hot Spot" due to its location very close to the beam pipe.

After a positive decision on L1 and L2 the complete event is read out, transferred to the fourth and last online triggering level L4, and the pipeline is restarted. Trigger level L3 has not been used so far. L4 is a software filter farm consisting of 32 parallel processors. At this level nearly the full event information is available after running a poor event reconstruction, which does not include the full calibration and tracking information. At this level the decisions of L1 and L2 are verified again, and, if necessary, the triggered events are rejected as background. Now the event information of each subdetector is summarized in certain data structures, so called banks, and written to tapes. At the offline operating trigger level L5 the events are fully reconstructed and classified according to their physics signature. Usually L5 is the starting point for each data analysis.

3.8 Detector Simulation

The simulation of the detector response to ep interactions allows realistic studies on event characteristics. Moreover, it is an important tool to correct the data for inefficiencies of the detector (for example the cracks of the LAr calorimeter). For the correction the program package H1SIM reads the four-momenta of particles, generated by a Monte Carlo model. It simulates the particles at their passage through the detector and calculates thereby all impacts of the detector components, acceptances, dead materials, electronic noise, etc. on the original four-momenta. The result are simulated events which are as close as possible to the events measured with the H1 detector. H1SIM itself is based on the program packages GEANT [GEA93]. The whole "physics" like tracking in a magnetic field, secondary particle generation and so on is simulated by the GEANT code from CERN upgraded with shower parametrisation packages.

Chapter 4

The Selection of Photoproduction Events

The most appropriate data for the inclusive measurement of the backward meson photoproduction are such as "unbiased" as possible. As mentioned above it is a big challenge for a high energy physics experiment to select the real ep scattering processes from background events. The clearer the signature of an event, the easier it is to perform this selection. For minimum bias events, there exists by definition no clear event signature, every physics event should be recorded. Thus two main problems appear when one tries to select physics events as minimally biased as possible:

1. the high triggering rate and the huge amount of events which has to be recorded;
2. their inconspicuous event signature.

To restrict these problems special data were taken by H1 for about one month at the end of 1997. This data sample is the basic data sample for the π^0 analysis. Unfortunately, the statistics of the sample allows only to measure the π^0 cross section at low values of $p_\perp$. For the extension of the π^0 cross section measurement towards higher values of $p_\perp$ another subtrigger was used, namely subtrigger 50, running since May 1996. Subtrigger 50 requires at least one cluster with a minimum energy around 2 GeV, recorded in the SpaCal with a minimal radial distance from the beam line of about 20 cm. With these requirements subtrigger 50 clearly biases the data sample by selecting events with a large backward activity which, for example, favours resolved photon and disfavours direct photon processes. In resolved processes the photon remnant is expected to be scattered in the backward direction while in direct processes no photon remnant exists (see section 1.4). In chapter 5 it will be shown that this subtrigger is nevertheless suited to measure the π^0 and η cross section for $p_\perp$ values above 1 GeV/c.
The basic selection criteria of events for the measurement of π^0 and η photoproduction are:

1. classification on trigger level L5 as events of the "Photoproduction Class";
2. the trigger conditions of subtrigger 50 in 1996 and of subtrigger 69 in the special minimum bias data taking period in 1997 were fulfilled.

Both selection criteria are discussed in the following sections.

4.1 Basic Selection of Photoproduction Events on Trigger Level L5

The selection cuts for the "tagged" photoproduction class on L5 require:

- the existence of a vertex or a minimal energy deposition of 1.5 GeV in the SpaCal. In events with charged particles scattered with large momenta only into the backward direction the acceptance of the central tracking system does not allow to reconstruct the vertex. The BDC can not be used for this purpose due to its moderate resolution in θ. Nevertheless, these events are not rejected in case they deposit an energy above 1.5 GeV in the SpaCal.

- $E_{\mathrm{eTag}_{33}} > 4$ GeV and $E_{\mathrm{photondetector}} < 2.0$ GeV or
  $E_{\mathrm{eTag}_{44}} > 6$ GeV and $E_{\mathrm{photondetector}} < 1.5$ GeV.
  $E_{\mathrm{eTag}_{33,44}}$ denotes the energy measured in the electron detector mounted at 33 m (44 m) in the backward direction from the interaction point and $E_{\mathrm{photondetector}}$ the energy of the photon detector. These conditions serve for the suppression of Bethe-Heitler processes used for the calculation of the luminosity which have a clear signature: an electron in one of the two electron detectors and a photon in the photon detector measured in coincidence. The energy sum of both recorded particles must yield 27.6 GeV, the beam energy of the incoming electron.

- the background recognizing routines accept the event. These routines are based on the different kinematics of beam-gas and *ep* events.

4.2 Subtrigger elements 50 and 69

Since May 1996 **subtrigger 50** requires at trigger level 1 (L1) a positive signal of the **electron tagger** (eTag)[1] and a minimal cluster energy in the SpaCal above $\approx$ 2 GeV (SPCLe_IET>1). Trigger level 2 (L2) accepts the event if the L1 triggering cluster is located in the SpaCal within a radial distance from the beam line of roughly 16 cm. In addition it consists of some trigger elements, which are based on the time-of-flight system (see section 3.4). The time-of-flight system is common to a lot of other subtriggers and designed to suppress beam-gas background.

The efficiency of the trigger element **SPCLe_IET>1** has been checked with subtrigger 43 which is completely based on the tracking system and, in contrast to SPCLe_IET>1, independent of the SpaCal. In 1996 subtrigger 43 required a positive signal of the electron tagger and at least one track with a transverse momentum greater than 0.4 GeV/c in the central pseudorapidity range ($|\eta| < 1.5$).
Figure 4.2 shows the efficiency of SPCLe_IET>1 which reaches a maximal value of (94.2 $\pm$ 1.0) %. To ensure a trigger efficiency of SPCLe_IET>1 of at least 40 % the cuts marked with the black bar in the plots of figure 4.2 have been applied. The energy of the cluster in the SpaCal with the largest energy (E_1) had to be above 2.2 GeV, and the distance of its center of gravity from the center of the beam line (RD_1) had to be larger than 16 cm.

[1]The expression "electron tagger" is used here as a synonym for the expression "electron detector".

During the minimum bias run period of 1997 **subtrigger element 69** simply consisted of the eTag trigger, a trigger element, requiring at least one track with a transverse momentum above 0.4 GeV/c, and some background suppressing conditions, also based on the time-of-flight system.
Both subtrigger elements 50 and 69 have the eTag trigger element in common which triggers on photoproduction events fulfilling the conditions $Q^2 < 0.01$ GeV^2 and $0.3 < y_{\rm B} < 0.7$.

4.3 Efficiency of the Electron Tagger

The **efficiency of the electron tagger** has been determined with the help of the program QPETAC [LEV95]. QPETAC supplies the run dependent efficiency of the electron tagger as a function of $y_{\rm B}$ if the electron is scattered into the fiducial region ($|x_{\rm eTag}| < 6.5$ cm) of the electron tagger. Figure 4.1 shows the efficiency of the electron tagger as a function of $y_{\rm B}$ for the year 1996 and for the minimum bias data taking period of 1997.

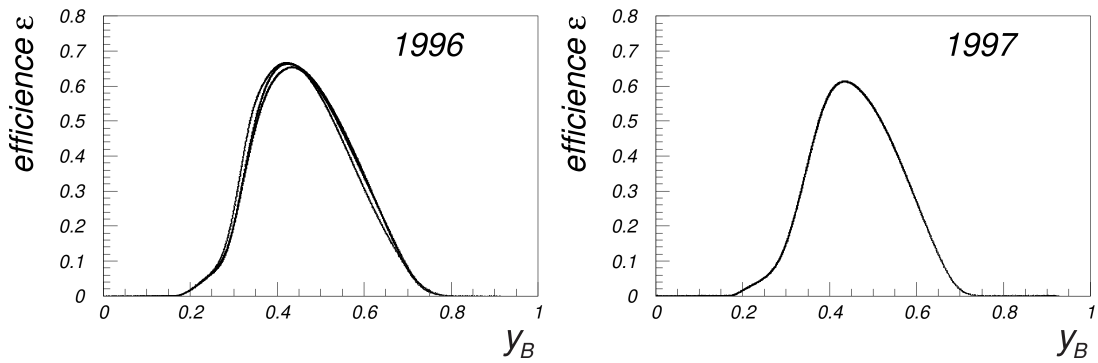

Figure 4.1: *Run dependent efficiencies of the electron tagger as a function of $y_{\rm B}$ for the years 1996 and for the minimum bias data taking period of 1997.*

In order to ensure a good electron tagger efficiency $y_{\rm B}$ was restricted to the range from 0.35 to 0.65 for both the π^0 and η cross section measurement.

To estimate the systematic uncertainty related to the absolute energy scale and energy resolution of the electron tagger the energy deposited in the tagger has been varied by 1.5 % for the 1996 and by 2.0 % for the 1997 data. The relative error $\Delta E/E$ of the electron tagger in 1997 is slightly larger compared to 1996 due to changes in the beam optics at the beginning of the year 1997. With ϵ denoting the efficiency of the electron tagger and $\Delta y^+, \Delta y^-$ the $y_{\rm B}$ variable for an electron tagger energy increased/reduced by 1.5 % and 2 % respectively, the final error was calculated via expression 4.1

$$\Delta\epsilon = \frac{|\epsilon(\Delta y^+) - \epsilon(\Delta y^-)|}{2} \tag{4.1}$$

to be 4 % on average for 1996, and 6 % for 1997.
Each event accepted by St50 and St69 has been weighted according to the weight W: $W = (\epsilon_{\rm eTag} \cdot f_i)^{-1}$ for i=50, 69 and with

$$f_{50}(E_1, RD_1) = \frac{0.94}{\exp(2.13 - E_1/0.195\,\mathrm{GeV}) + 1} \cdot \frac{0.94}{\exp(15.6 - RD_1/1.99\,\mathrm{cm}) + 1} \tag{4.2}$$

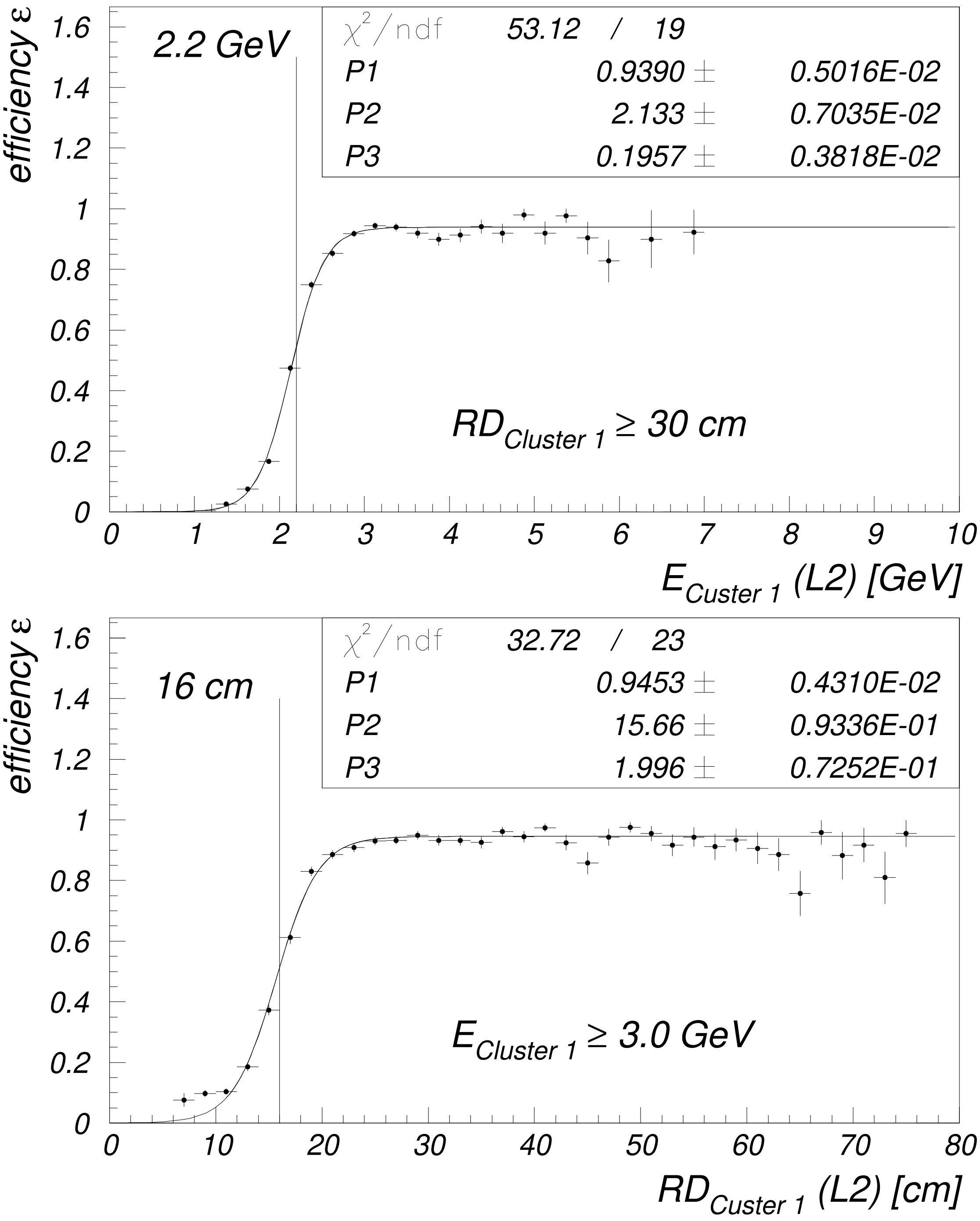

Figure 4.2: *Efficiency of subtrigger 50 as a function of the energy of the hottest cluster (upper plot) and as a function of the distance of the hottest cluster from the beam line (lower plot).*

describing the function displayed in figure 4.2. The events selected by subtrigger 69 had to be weighted only with the inverse efficiency of the electron tagger, i.e. $f_{69} = 1$.
Table 4.1 summarizes the **event selection cuts**.

Event selection cuts for Subtrigger 50	Event selection cuts for Subtrigger 69
$0.35 < y_{\mathrm{B}} < 0.65$	$0.35 < y_{\mathrm{B}} < 0.65$
$\mathrm{RD}_1 > 16$ cm	-
$\mathrm{E}_1 > 2.2$ GeV	-
$L_{\mathrm{run}} > 0.5\ \mathrm{nb}^{-1}$	$L_{\mathrm{run}} > 0.5\ \mathrm{nb}^{-1}$
Vertex reconstructed	Vertex reconstructed
$\lvert Z_{\mathrm{vertex}} \rvert < 35$ cm	$\lvert Z_{\mathrm{vertex}} \rvert < 35$ cm

Table 4.1: *Event selection cuts. RD_1 denotes the radial distance of the center of gravity of the hottest cluster from the center of the beam line in the SpaCal. E_1 marks the energy of the hottest cluster in the SpaCal. L_{run} is the run luminosity.*

Applying these event selection cuts and requiring that all detector components, used in this analysis, were operational during data taking, one obtains an integrated luminosity of $\approx 300\ \mathrm{nb}^{-1}$ (corresponding to $\approx$ 115K events) for the minimum bias run and of $\approx 4.3\ \mathrm{pb}^{-1}$ (corresponding to $\approx$ 500K events) for the 1996 data. Figure 4.3 displays for both subtriggers the ratio of the number of selected events over the run luminosity and the number of selected events as a function of the integrated luminosity of all considered runs. These plots demonstrate the stability of the subtriggers used.

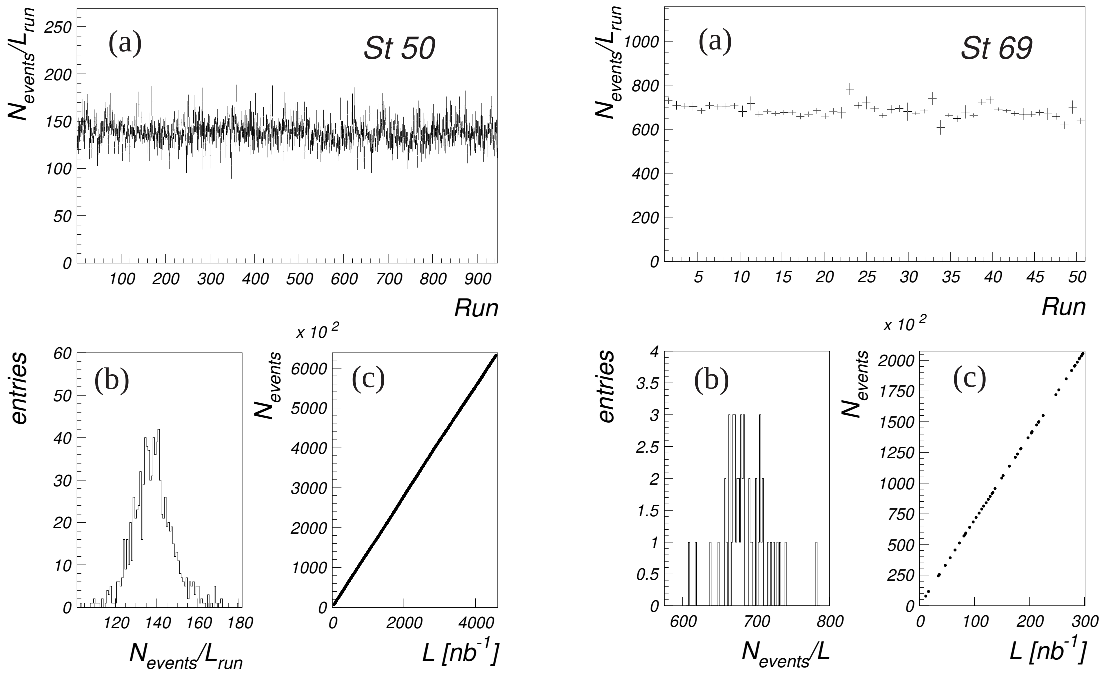

Figure 4.3: *The number of events in the plots a,b and c fulfil the selection cuts listed in table 4.1 for subtrigger 50 and 69 respectively. (a) Number of events over the run luminosity as a function of the run number. (b) Number of events per run luminosity. (c) Number of selected events as a function of the integrated luminosity.*

4.4 Estimation of the Remaining Background in Photoproduction Events

The background in photoproduction events due to interactions of the electron with particles of the rest gas in the beam pipe was estimated with the help of pilot bunches (see section 3.6). Using equation 3.10 with $(I_{\mathrm{ebeam}} + I_{\mathrm{pilot}})/I_{\mathrm{pilot}} \approx 13$ for 1996 and 1997, the contribution of the background events of the data selected in 1996 yields ≈ 1.5 % and ≈ 1.0 % for the minimum bias data of 1997.

Finally, one has to distinguish between contributions from beam-gas events to the γp cross section and to the π^0 and η cross section. A priori it is not clear that the beam-gas events contribute to the π^0 and η cross section in the same way as ep interactions due to their completely different kinematics. To this end the relative number of reconstructed π^0s per event, N_{π^0}/event, in the rapidity range -3.5 $< y <$ -1.5 was determined for ep and for beam-gas interactions. The results are:

$$\begin{aligned} N_{\pi^0}(ep)/\,\mathrm{event} &= 1.7 \;\text{ for } ep \text{ interactions,} \\ N_{\pi^0}(bg)/\,\mathrm{event} &= 0.9 \;\text{ for beam-gas interactions.} \end{aligned}$$

The number of π^0 per event for beam-gas interactions is only half as large as for ep interactions. Thus, the background events contribute to 1.5 % (1.0 %) to the total γp cross section but only to 0.75 % (0.5 %) to the π^0 (η) cross section.

Chapter 5

π^0 and η Mesons in the SpaCal and LAr Calorimeter

The procedure for reconstructing and counting π^0 and η mesons is as follows: Each photon pair, from either the SpaCal or the LAr calorimeter, is labelled according to the kinematic variable of interest, for example according to the energy, the transverse momentum or the rapidity of the photon. These quantities are calculated with the help of the four-momenta of the meson, derived from the cluster energy, the cluster coordinates, and the coordinates of the interaction point. For every photon pair, the invariant mass $m_{\gamma\gamma}$ is calculated via formula 5.1:

$$m_{\gamma\gamma}^2 = 2E_1E_2(1 - \cos\Omega_{12}) \ . \tag{5.1}$$

Here E_1 and E_2 are the energies of the measured calorimeter clusters, attributed to the decay photons, and Ω_{12} is their opening angle.

The following sections deal with the optimisation of the photon selection cuts with the help of the π^0 signal. This optimisation aims at finding the photon selection cuts with the best signal-to-background-ratio in the two-photon mass spectra. It has to fulfil the additional condition to keep the efficiency for the photon selection as high as possible. This optimisation is done with the help of the MC models PHOJET and PYTHIA. For this purpose it must be proven that any given cut has the same effect in the data and the MC models. In order to check this the energy scales of the SpaCal and the LAr calorimeter in data and simulated events are studied and corrected before the distributions in data and simulated events, relevant for the present analysis, are compared.

5.1 π^0 and η Mesons in the SpaCal

First the energy scale of the SpaCal is investigated. The $m_{\gamma\gamma}$ spectrum is plotted in intervals of the cluster energy, see figure 5.1. The mass peak is fitted with a Gaussian function, and the background with a fourth order polynomial. The mean value of the Gaussian is associated with the reconstructed π^0 mass.

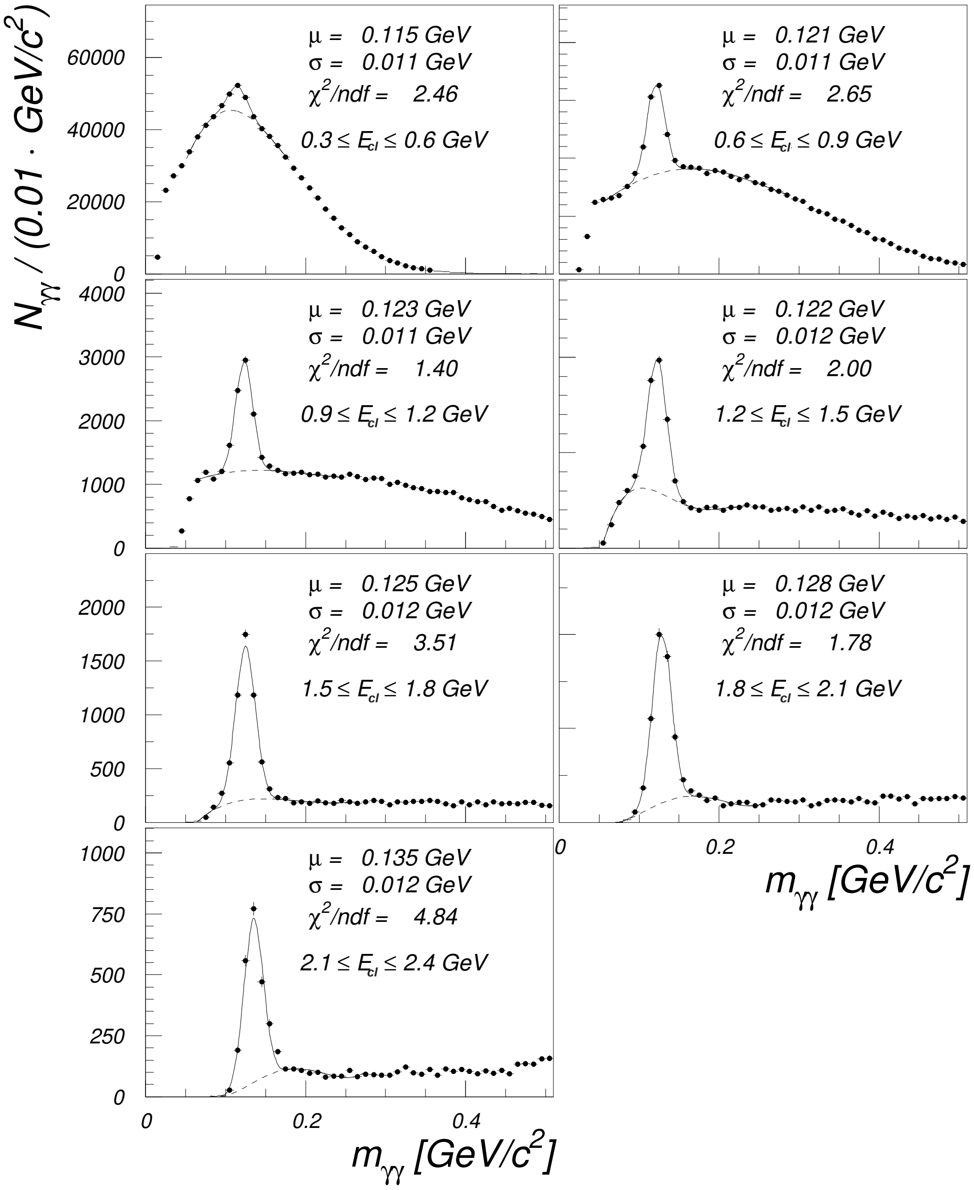

Figure 5.1: *SpaCal: $m_{\gamma\gamma}$ distributions in intervals of the cluster energy (data). The mass peak is fitted with a Gaussian, the background with a polynomial of fourth order.*

With increasing energy the deviation between the reconstructed π^0 mass and its nominal value of 135 MeV/c^2 becomes smaller and reaches the nominal mass value in the highest energy bin. There are two reasons for the deviation of the π^0 mass from its nominal value in the very low energy range ($E_{cl} < 2.0$ GeV):

- the noise cut of 15 MeV for each SpaCal cell and
- the "dead material" in front of the calorimeter.

Assuming that one cell per cluster is rejected due to the noise cut, the 15 MeV cut yields for example in the energy interval from 0.3 GeV to 0.6 GeV an energy loss of (2 - 5) % which directly transforms into the deviation of the π^0 mass from its nominal value. The observed deviation in this bin (see table 5.1) is about 15 %. Thus, the additional energy loss is due to the rejection of more than one cell per cluster or due to the energy loss of the π^0 decay photons, converted into (e^+, e^-) - pairs, and crossing the dead material in front of the calorimeter (energy losses due to pre-shower and ionization processes).

5.1.1 SpaCal Energy Scale Correction

For the correction of the energy scale the value of the measured π^0 mass has been used. For $E_1 \approx E_2$ formula 5.1 results in the simple relation $m_{\gamma\gamma} \propto E_\gamma$ which has been applied to perform the energy correction. To get the correction values for the very low energy range ($E_{\rm cl} < 2$ GeV) the π^0 mass is measured in three radial areas of the SpaCal and in intervals of the cluster energy. The result of this measurement is, for each radial area of the SpaCal, a functional relation between the measured π^0 mass and the cluster energy interval in which the π^0 is reconstructed. The relative deviation of the reconstructed π^0 mass from the nominal value has been used as a correction factor for the corresponding energy interval. For example, a reconstructed π^0 mass 20 % below the nominal mass value of 135 MeV/c^2 leads to an energy correction factor of 1.2 in the energy interval in which the π^0 has been reconstructed.
For the lowest energy interval of the inner part of the SpaCal ($0.3 < E_{\rm cl} < 0.6$ GeV, 8 cm $< RD <$ 20 cm)[1], where no clear π^0 peak is visible, the correction value of the central part of the SpaCal in the corresponding energy range has been taken. After applying these correction factors to the cluster energy, the resulting new values of the π^0 masses were compared with their nominal values. From the comparison new correction factors were derived and again applied to the cluster energy. This procedure was repeated until the deviation of the π^0 mass from its nominal value was less than 3 % in all energy bins where the π^0s could be reconstructed. In table 5.1 the π^0 mass as a function of the cluster energies before and after the correction are listed.

E_γ [GeV]	0.3 - 0.6	0.6 - 0.9	0.9 - 1.2	1.2 - 1.5	1.5 - 1.8	1.8 - 2.1	2.1 - 2.4	
$m_{\gamma\gamma}$	-	0.119	0.126	0.119	0.123	0.128	0.136	A
[GeV/c^2]	0.124	0.120	0.123	0.121	0.124	0.129	0.134	B
before corr.	0.115	0.120	0.123	0.122	0.123	0.128	0.134	C
$m_{\gamma\gamma}$	-	-	0.139	0.134	0.136	0.135	0.135	A
[GeV/c^2]	0.133	0.134	0.135	0.136	0.135	0.135	0.137	B
after corr.	0.133	0.135	0.135	0.135	0.133	0.136	0.135	C
corr.	1.14	1.14	1.07	1.14	1.10	1.05	0.99	A
factors	1.10	1.13	1.10	1.11	1.08	1.05	1.00	B
	1.17	1.12	1.10	1.10	1.09	1.05	1.00	C

Table 5.1: *π^0 mass as a function of the energy of the photon candidates in the regions A,B and C of the SpaCal (data). Region A: $8 < RD < 20$ cm, region B: $20 < RD < 40$ cm, region C: $40 < RD < 75$ cm.*

The error of the corrected energy scale has been estimated via the relation

[1] $E_{\rm cl}$ = Cluster energy, RD = Radial Distance of the cluster center of gravity from the center of the beam line.

$$\frac{\Delta(m^2)}{m^2} = \sqrt{\left(\frac{\Delta E_i}{E_i}\right)^2 + \left(\frac{\Delta E_j}{E_j}\right)^2} \tag{5.2}$$

For $E_i \approx E_j$ follows $\Delta(m^2)/m^2 = \sqrt{2} \cdot \Delta E/E$, and replacing $\Delta(m^2)$ by $2 \cdot m \cdot \Delta m$ finally yields:

$$\frac{\Delta m}{m} = \frac{1}{\sqrt{2}} \frac{\Delta E}{E} \tag{5.3}$$

This means that the uncertainty of 3 % on the π^0 mass is due to an uncertainty of the energy scale of the SpaCal in the considered energy range of about 4 %. A simple method for verifying the quality of the SpaCal calibration is to check whether higher mass mesons, e.g. the η and the ω mesons, can be reconstructed in the SpaCal with masses close to their nominal values. The PDG mass [PDG98] of the η is (547.45 ± 0.19) MeV/c^2 and for the ω the PDG mass is (791.94 ± 0.12) MeV/c^2. Figure 5.2 shows the π^0, η and ω signals as seen in the SpaCal after correcting the low energy scale with the help of the π^0 mass. These mesons have been reconstructed within the rapidity range: $-3.5 < y_{\pi^0,\eta} < -1.5$ and $-3.5 < y_\omega < -3.0$ with $E_\gamma > (0.5, 1.0, 0.4)$ GeV for the π^0, η and ω meson respectively.

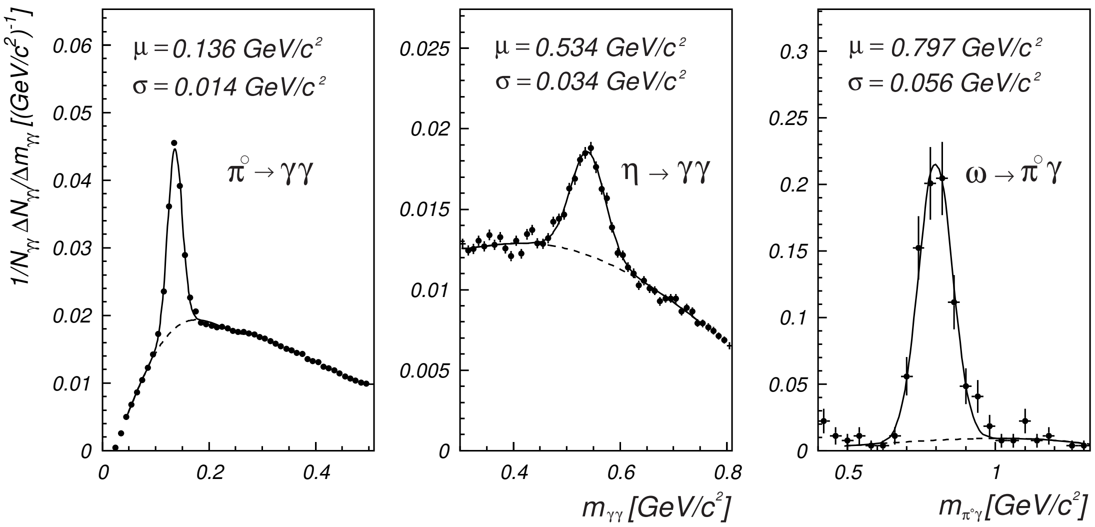

Figure 5.2: *The inclusive π^0, η and the exclusive ω signals as seen in the SpaCal after applying the energy scale correction with the help of the π^0 mass.*

For all three mesons the reconstructed mass agrees with the PDG mass within 3 %.

The energy scale correction has been performed with the data of 1996 selected by subtrigger 50 due to the high statistics of this data sample. Applying these correction factors to the minimum bias data of 1997 has also shown good results, with a comparable final error on the energy scale of 4 %.

5.1.2 Energy Scale of the SpaCal in MC Simulations

It was already mentioned that SpaCal cells with an energy below 15 MeV are not taken into account in the reconstruction of clusters (see section 5.1). The energy loss due to this cut is also visible in MC generated events. Therefore, the same energy scale correction has been applied to the simulated events, leading to correction factors listed in table 5.2. This recalibration procedure of the SpaCal finally yields an uncertainty of the energy scale in the simulated events of 4 % as before in case of data.

E_γ [GeV]	0.3 - 0.6	0.6 - 0.9	0.9 - 1.2	1.2 - 1.5	1.5 - 1.8	1.8 - 2.1	2.1 - 2.4	
$m_{\gamma\gamma}$	-	0.127	0.132	0.132	0.132	0.130	0.133	A
[GeV/c^2]	0.131	0.127	0.128	0.129	0.130	0.131	0.135	B
before corr.	0.126	0.128	0.129	0.129	0.129	0.132	0.131	C
$m_{\gamma\gamma}$	-	-	0.137	0.135	0.133	0.136	0.134	A
[GeV/c^2]	0.133	0.135	0.134	0.136	0.135	0.134	0.135	B
after corr.	0.135	0.135	0.135	0.134	0.135	0.135	0.132	C
corr.	1.06	1.06	1.02	1.03	1.02	1.04	1.02	A
factors	1.03	1.06	1.05	1.05	1.04	1.03	1.00	B
	1.06	1.06	1.04	1.04	1.04	1.02	1.03	C

Table 5.2: π^0 *mass as a function of the cluster energy in the region A,B and C of the SpaCal (PYTHIA). Region A:* $8 < RD < 20$ *cm, region B:* $20 < RD < 40$ *cm, region C:* $40 < RD < 75$ *cm. (RD = Radial Distance of the cluster center of gravity from the beam line.)*

5.1.3 Comparison of the SpaCal Data and the Simulated Events

After the correction of the SpaCal energy scale derived from data and simulated events it is possible to compare those quantities of the data which are relevant for the present analysis with the corresponding quantities of the simulated events. Already the first check of the minimum bias run of 1997 showed that there were problems with the electron tagger in this running period. Figure 5.3 compares the y_{B} distribution of a subsample of the special minimum bias run period with the y_{B} distribution of simulated events (PYTHIA). For electron energies below 13.2 GeV corresponding to values of y_{B} above 0.52 the electron tagger did not reach its full acceptance.

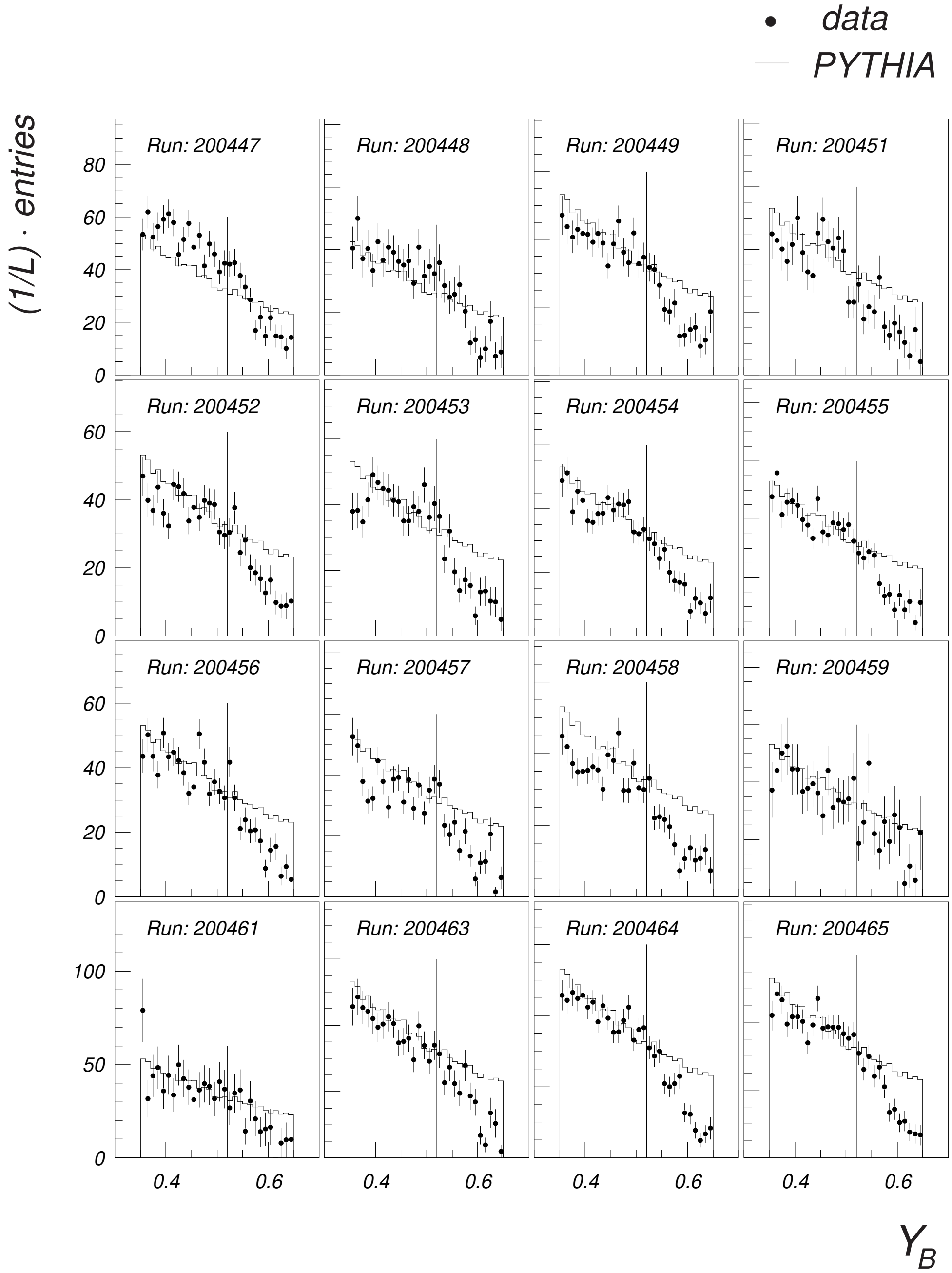

Figure 5.3: *Comparison of the y_B distribution in data and the MC PYTHIA. For $y_\mathrm{B} >$ 0.52 the electron tagger did not reach its full acceptance.*

At the end of 1997 it was realized in the context of the calibration of the luminosity system that there were problems concerning the electron tagger. Due to a distorted magnetic field in the beginning of the data taking period in May 1997 a quadrupole bridge between the H1 interaction point and the electron tagger had to be lowered. The changed magnetic field led to changes in the hit population of the electron tagger and thus to modifications of its acceptance. With the condition that the sum of the energy of the photon detector and the electron detector must yield the beam energy for Bethe-Heitler processes, a offline correction could be performed. This correction mainly depends on the x and y coordinate of the impact point of the particle in the electron tagger. The effects of this correction on the energy of the electron tagger and the corresponding y_{B} distribution are shown in figure 5.4.

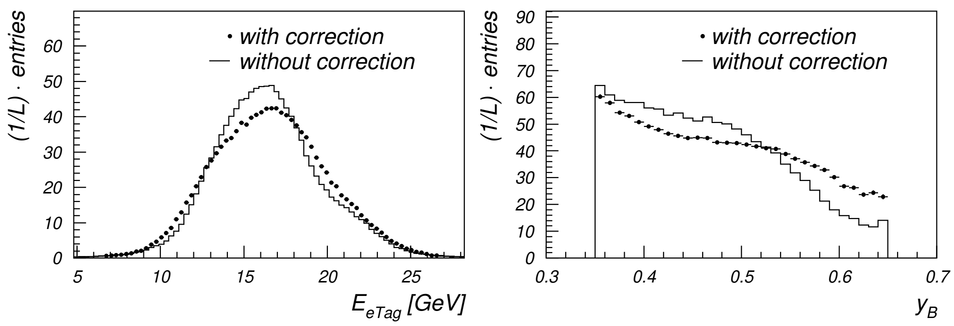

Figure 5.4: *Left side: Energy of the electron tagger for the minimum bias run 1997 before and after the energy correction. Right side: reweighted y_{B} distribution (see section 4.3) before and after the energy correction. $y_{\mathrm{B}} = 1 - E'_e/E_e$ with E_e = electron beam energy, E'_e = energy of scattered electron.*

The energy distribution of the electron tagger is broader after the correction and slightly shifted towards larger energies. The shape of the y_{B} variable is clearly improved, the steep fall of this distributions at $y_{\mathrm{B}} = 0.52$ is gone.
The upper left plot of figure 5.5 compares the z-vertex distributions between data and the MC models PHOJET and PYTHIA, and the upper right plot the y_{B} distributions within the range between 0.35 and 0.65 for the selected minimum bias data. Since the z-vertex distribution of the MC models is slightly shifted towards larger values the simulated events have been reweighted with respect to this variable. The reweighted distributions can be seen in the lower left and right plots of figure 5.5, respectively.

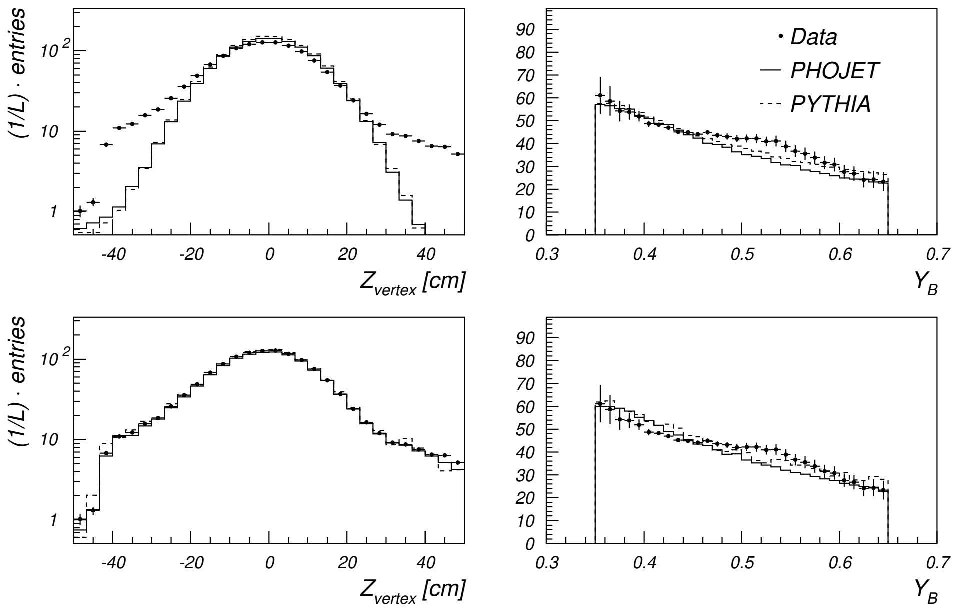

Figure 5.5: *Left side: Comparison of the z-vertex and y_{B} distributions between data (points) and the MC models PHOJET (full line) and PYTHIA (dotted line) for the minimum bias run period 1997 before reweighting. Right side: The same quantities as before but this time after the reweighting of the z-vertex distributions.*

The reweighting with respect to the z-coordinate of the vertex does not change the shape of the y_{B} distribution but increases the absolute number of entries in this plot, an effect which clearly improves the agreement between the data and the MC predictions. The errors shown in the y_{B} distributions are determined with the method described in section 4.3. The average error specified there is 6 %. The plots above show that the largest contributions to this error are due to the edges of the y_{B} distribution where the acceptance corrections for the electron tagger are highest. The reweighting procedure is as follows: First the z-coordinate of the vertex distributions of the data and the simulated events are normalised to one and divided by each other. The distribution obtained by the division is fitted with a polynomial of third order which then is used as reweighting function for the vertex distribution, i.e. each quantity of an event is filled into a histogram with the factor received by the reweighting function.
The next figure 5.6 compares the three most energetic clusters of the data with the corresponding clusters of the simulated events reweighted according to the procedure described above. The MC models are in good agreement with the data.

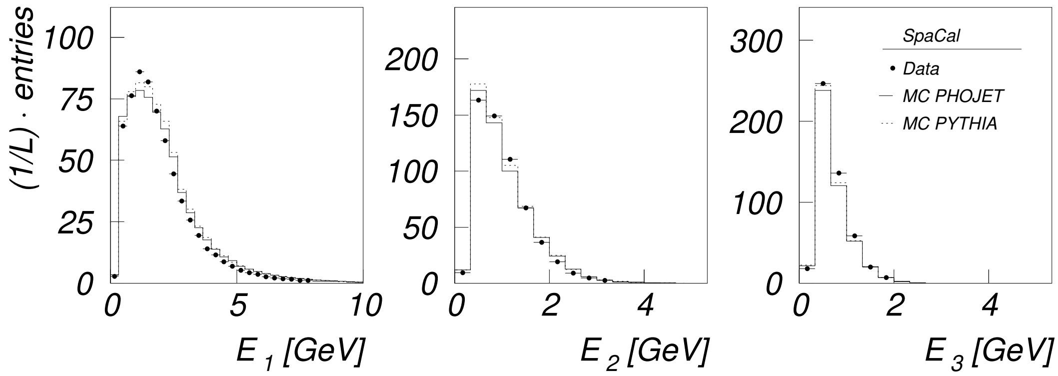

Figure 5.6: *SpaCal: Comparison of the energy of the three most energetic clusters in data (points) and the MC models PHOJET (full line) and PYTHIA (dotted line).*

Figure 5.7 shows that also the radial distributions of the clusters over the SpaCal are well reproduced by the MC models.

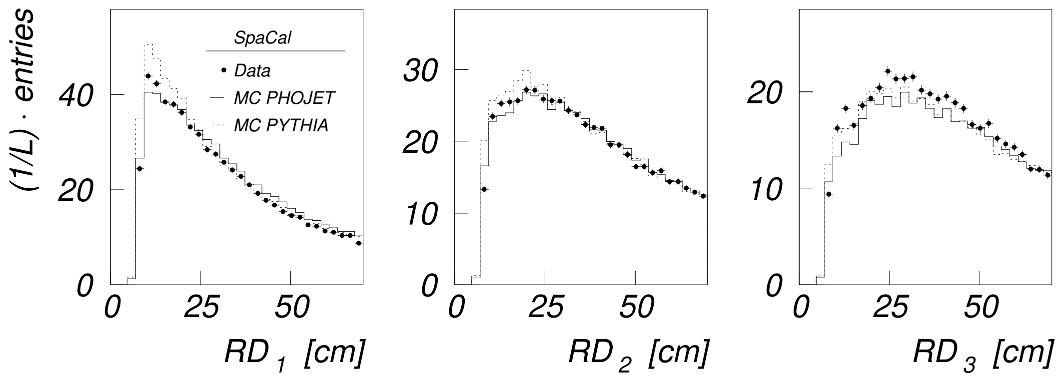

Figure 5.7: *SpaCal: Comparison of the radial distribution of the three most energetic clusters in data (points) and the MC models PHOJET (full line) and PYTHIA (dotted line).*

Finally figure 5.8 compares the radii of the first three most energetic clusters. The agreement is less satisfactory. There are more clusters with large radii in the data than in the simulated events. This can be explained as a result of the imperfect modelling of the dead material in front of the SpaCal by the simulation program. As shown in the section before, the energy loss of particles due to their crossing of dead material in front of the calorimeter is smaller in the simulated events than in the data. Dead material is necessary for the photons to convert into (e^+, e^-) - pairs. Clearly, these pairs are recorded very close to each other in the SpaCal so that they can't be resolved, but in some cases their distance is large enough for depositing their energy in more than one SpaCal cell. This leads finally to clusters with slightly more cells in the data than in the simulated events, and more cells attributed to a cluster means larger cluster radii.

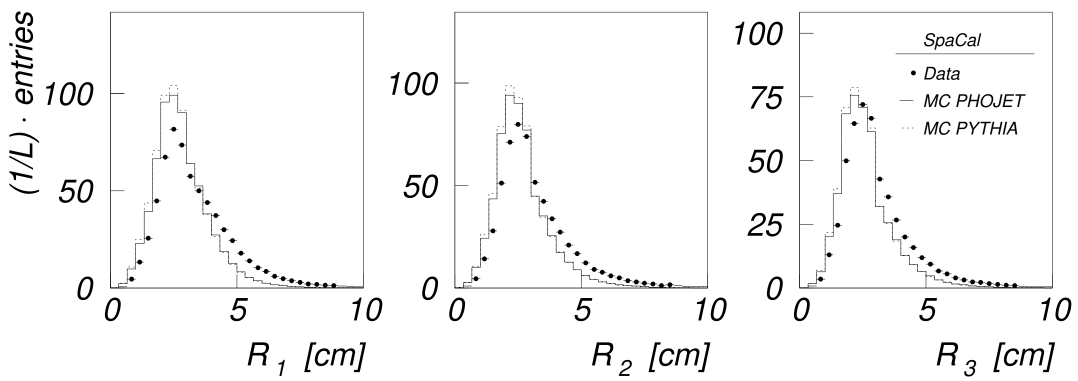

Figure 5.8: *SpaCal: Comparison of the radii of the three most energetic clusters in data (points) and the MC models PHOJET (full line) and PYTHIA (dotted line).*

Due to this problem of the inaccurate description of the cluster radii by the detector simulation no cut was applied on this quantity in the π^0 and η cross section measurements. Despite the fact that no cut on the cluster radii was applied the question still remains, how far the differences in the clustering result in differences concerning the merging of two SpaCal clusters in data and simulated events . This question will be answered in the context of the discussion of the systematic errors of the π^0 cross section measurement in section 6.4.1.

For **subtrigger 50** the same checks have been performed. In contrast to subtrigger 69, used for the minimum bias running period, the setting of the subtrigger 50 bit depends on the most energetic cluster in the SpaCal, see section 4.2 and table 4.1. In the MC simulation the subtrigger 50 triggering conditions are emulated by the cuts on the most energetic cluster (E_1) and its radial distance from the beam line (RD_1). To guarantee that a cut on these quantities rejects as many events in the data as in the simulation, the MC models have been sequentially reweighted with respect to the z-vertex distribution, the most energetic cluster and its radial distribution. Figure 5.9 depicts the comparison between data and the reweighted MC events. The agreement is satisfactory.

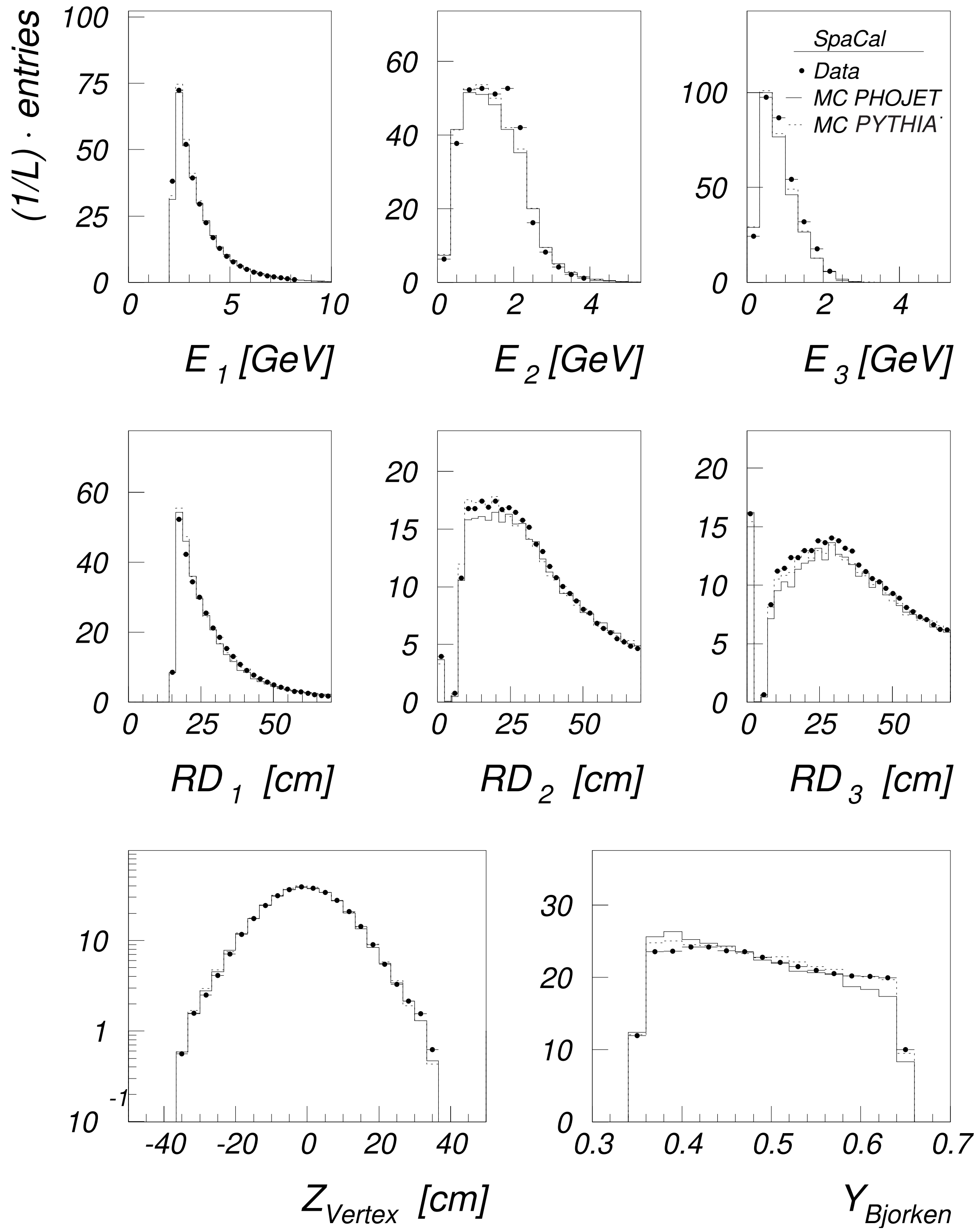

Figure 5.9: *SpaCal: Comparison of data selected by subtrigger 50 and the reweighted MC models PHOJET (full line) and PYTHIA (dotted line).* E_1 - E_3 *= Energy of the first three most energetic clusters,* RD_1 - RD_3 *the corresponding radial distance of the cluster center from the beam line. The z-vertex and the* $y_{\rm B}$ *distribution.*

5.1.4 Optimisation of the Photon Selection Cuts in the SpaCal

The last section has shown that the MC models are able to describe the data after some corrections. This allows now to optimise the photon selection cuts.
For the SpaCal, the following detector quantities influence the efficiency of the photon selection:

- the minimal cluster energy $E_{\text{cl, min}}$,
- the cluster radius R_{cl},
- the number of cells N_{cl}^{cell} belonging to a cluster,
- the hadronic cluster energy fraction $F_{\text{had}} = E_h/(E_e + E_h)$, where E_h and E_e denote the cluster energy in the hadronic and electromagnetic section of the SpaCal respectively,
- the distance DCT_{cl} between the cluster center to the closest track in the BDC.

The optimisation was done via the two-photon mass spectra. For this purpose the conditions on the cluster variables listed above were tuned in such a way that the best signal-to-background-ratio in the mass spectra was achieved.

The minimal cluster energy: $E_{\text{cl, min}}$

Clearly, when tightening the cut on the minimal cluster energy, the number of two-photon combinations is reduced, i.e. the combinatorial background decreases and the π^0 signal becomes more pronounced (see figure 5.10).

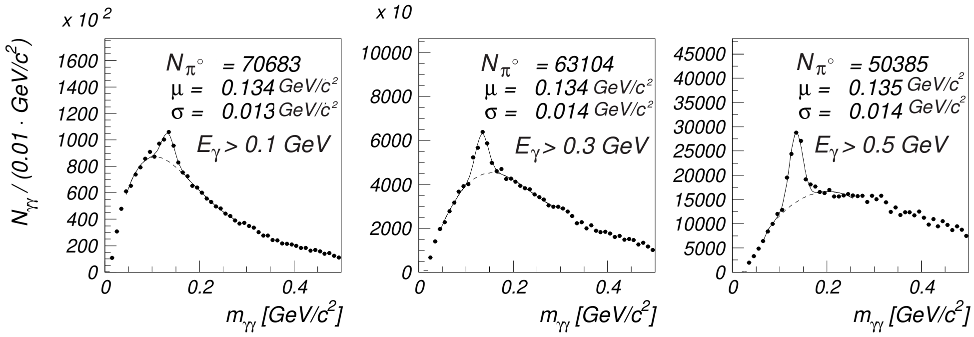

Figure 5.10: *SpaCal: $m_{\gamma\gamma}$ distributions with different cuts on the electromagnetic cluster energy E_{cl}.*

Nevertheless this cut has to be chosen as weak as possible because the π^0 and η cross sections are measured as a function of $p_\perp$, the meson transverse momentum, and y, the meson rapidity. Both variables are strongly correlated with the energy of the mesons, thus cutting on $E_{\text{cl, min}}$ restricts the phase space of the mesons. In order to get a stable π^0 signal in all bins in which the cross section is measured, a minimal cluster energy of 0.3 GeV had to be applied.

The cluster radius: R_{cl}

The probability for charged pions to generate hadronic showers in the electromagnetic part of the SpaCal is about 65 % [APP95]. Thus, hadrons, first of all π^+ and π^- mesons represent –beside the unavoidable combinatorial background– a major part of the background. Hadrons generate broader showers than photons in the calorimeter. Therefore, the cut on the cluster radius is a well suited tool for reducing the hadronic background.

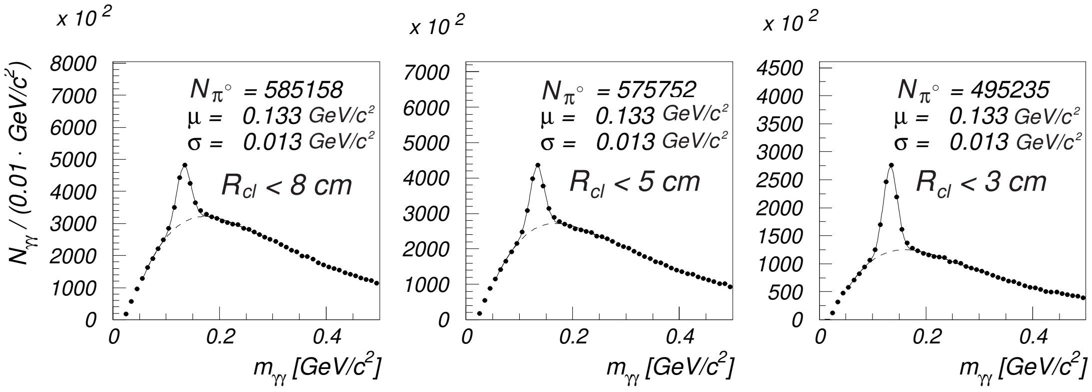

Figure 5.11: *SpaCal: $m_{\gamma\gamma}$ distributions for different cuts on the cluster radius (E_{cl} > 0.3 GeV).*

From left to right in figure 5.11, the cut on the cluster radius is tightened from 8 cm to 3 cm. As expected, the π^0 signal becomes more pronounced while the number of π^0s, represented by the number of photon pairs in the signal, decreases from 585158 to 495235, indicating that also about 15 % of the photons, which are associated with the clusters, are touched by tightening the cut on the cluster radius. Due to the fact that the cut of 300 MeV on the cluster energy guarantees a clear π^0 signal in the $m_{\gamma\gamma}$ distributions and due to the loss of nearly 15 % of π^0s in the signal it is not necessary to cut on the cluster radius for the neutral meson analysis. In addition not to cut on the cluster radius avoids the problem of the poor description of this quantity by the MC models PHOJET and PYTHIA as can be seen in figure 5.8.

The number of cluster cells: N_{cl}^{cell}

The cluster radius is strongly correlated with the number of cells belonging to a cluster. The bad description of the cluster radius by the MC models suggests not to cut on the number of cluster cells. Consequently only single cell clusters were excluded in the data and the MC events in order to suppress noise clusters which often consist of one cell only. In addition single cell clusters have a bad localisation in the xy-plane of the SpaCal since their cluster centers are associated with the coordinates of the SpaCal cells, i.e. with an accuracy of 4 x 4 cm^2. With a minimal cluster energy of 0.3 GeV the effect of this cut on the π^0 and η signal is negligible.

The hadronic energy fraction of a cluster: F_{cl}

Given the depth of the electromagnetic section, 65 % [APP95] of the incoming charged pions are expected to interact inelastically in the electromagnetic volume. Taking also the hadronic section of the SpaCal into account the probability for their interactions increases to 88 %. Thus, the selection of photon candidates can be improved by cutting on the hadronic energy fraction of a cluster F_{had}. The influence of this cut on the shape of the $m_{\gamma\gamma}$ spectrum is marginal as shown in figure 5.12. The most π^0s are found for $F_{\text{had}} < 1$ which means no restriction on F_{had} since this quantity is *per definitonem* limited to the range between 0 and 1. The improvement of the signal due to a stronger cut on F_{had} is negligible. Therefore, no cut is applied on this variable.

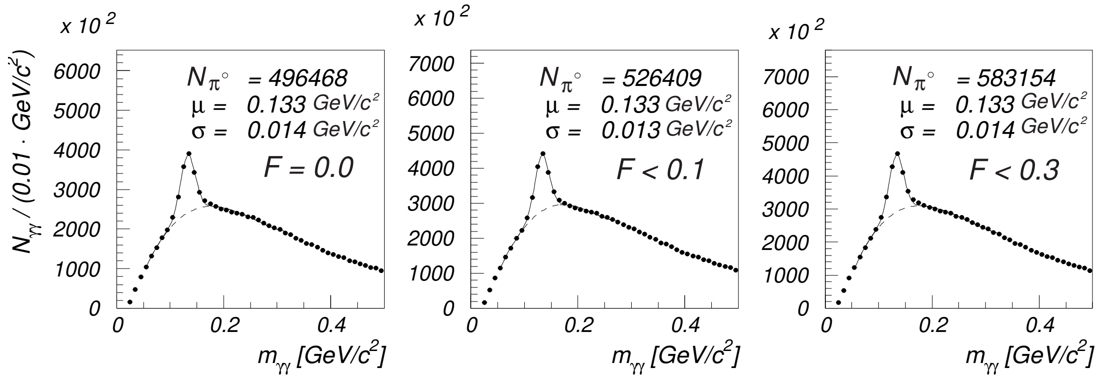

Figure 5.12: *SpaCal: $m_{\gamma\gamma}$ distributions with different cuts on the hadronic cluster energy fraction F.*

The distance between the cluster center to the nearest track of the BDC: DCT_{cl}

Usually a simple way to separate photons from charged particles is to cut on the distance between the cluster center, generated by the photon candidate, to the nearest track in the track chamber pointing to the photon's cluster center in the calorimeter. The backward drift chamber BDC, designed for the identification of charged particles flying into the SpaCal is directly mounted in front of this calorimeter. Due to the good resolution, the BDC is able to see a photon converted into an (e^+, e^-) - pair as two separated charged particles. Therefore, a cut on the distance between the cluster center to the next BDC track rejects beside the charged hadrons the photons converted in (e^+, e^-) - pairs. The left plot of figure 5.13 contains 570502 π^0s in the signal bins if no cut on the closest BDC track is applied. With the requirement that there is no track around the cluster center of gravity in a radius of 10 cm only 176070 π^0s are found in the signal, see right plot of figure 5.13, e.g. only 30 % of the π^0s survive this cut. Clearly, the signal-to-background-ratio is nicely improved by this cut, but the huge loss of π^0s which this cut implies, does not make it applicable.

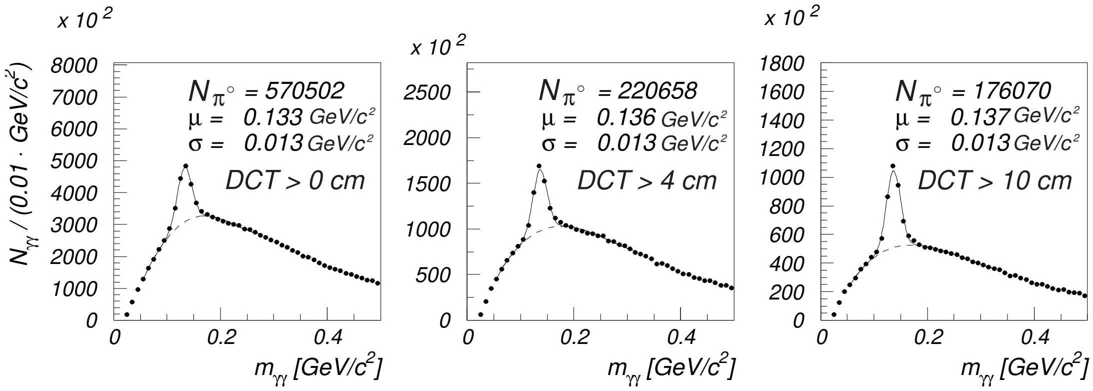

Figure 5.13: *SpaCal: $m_{\gamma\gamma}$ distributions for different cuts on the distance of the cluster center to the closest BDC track (DCT = Distance of Cluster center to closest Track).*

5.2 π^0 Mesons in the LAr Calorimeter

The next sections are completely analogous to the sections before but concern this time the energy scale of the LAr calorimeter and the comparison of the LAr distributions in the data and the MC simulations PHOJET and PYTHIA.

5.2.1 LAr Energy Scale Correction

The energy scale correction for the LAr calorimeter with the help of the π^0 mass is quite similar to the energy scale correction of the SpaCal already described. The main difference between both methods is that in the LAr calorimeter the π^0 mass was not reconstructed from photons with the requirement that both photons have approximately the same energy but with the requirement that both photons are recorded in the same LAr wheel. The latter condition includes anyway, as Figure 5.14 shows, that the energies of both photons lie mainly in a range from 0.5 to 1.0 GeV.

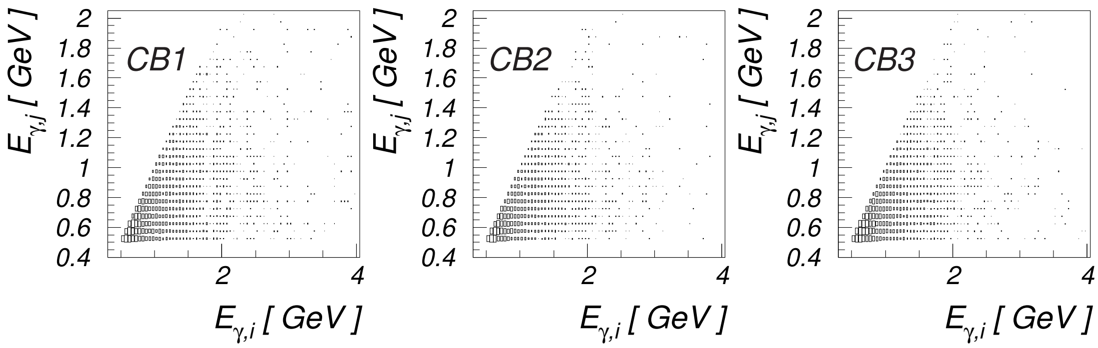

Figure 5.14: *Energy of the photons of the LAr calorimeter used for the $m_{\gamma\gamma}$ spectra (data), reconstructed in the central barrels one, two and three, abbreviated with CB1, CB2 and CB3 (compare figure 3.3).*

Figure 5.15 displays $m_{\gamma\gamma}$ spectra reconstructed from photons where both are recorded in the same LAr wheel. As before the mass peak is fitted with a Gaussian and the background with a polynomial of fourth order. The mean value of the Gaussian is associated with the π^0 mass. As correction factors for the energy scale of the LAr the relative deviations of the measured π^0 mass in each wheel from its nominal value have been taken. These correction factors were applied to the cluster energies, and then the new values of the π^0 mass in each wheel were compared with its nominal value. This procedure was repeated until the agreement of the measured π^0 mass and the nominal value of 135 MeV/c^2 reached the 3 % level. Table 5.3 summarizes the measured π^0 masses before and after the energy scale correction including the final values of the correction factors.

AE0R					
wheel	FB2	FB1	CB3	CB2	CB1
corr. factor	1.20	1.15	1.12	0.94	1.00
m_{π^0} [GeV/c^2] before corr.	0.115	0.117	0.122	0.138	0.135
m_{π^0} [GeV/c^2] after corr.	0.131	0.134	0.138	0.135	0.133

AE1R					
wheel	FB2	FB1	CB3	CB2	CB1
corr. factor	1.09	1.00	1.0	0.88	0.88
m_{π^0} [GeV/c^2] before corr.	0.127	0.137	0.136	0.153	0.152
m_{π^0} [GeV/c^2] after corr.	0.134	0.137	0.138	0.137	0.138

Table 5.3: *LAr: π^0 mass reconstructed from photons in the case where both are recorded in the same LAr wheel (Data).*

In order to estimate the error on the energy scale with formula 5.3 the π^0s have been reconstructed in energy intervals of 0.5 GeV from 0.5 GeV to 2.0 GeV within the range of the z-coordinate of the LAr from -152 cm to 288 cm. The largest deviation in each bin is about 3 % and thus comparable to the largest deviation found by comparing the π^0 mass in each wheel with the nominal value. Using formula 5.3 an uncertainty of 3 % in the π^0 mass leads to an uncertainty of the LAr energy scale of about 4 %.
For the LAr calorimeter two scales for the cluster energies are accessible, stored in the AE0R and AE1R data bank. The AE0R bank contains the information of the uncorrected (LAr) cluster energies while the AE1R bank already comprises corrections for the energy loss of particles due to their crossing of dead material in front of the calorimeter. These corrections have been derived from particles with energies above 10 GeV. The values of the π^0 mass measured with the AE1R bank listed in table 5.3 show that these corrections overestimate the influence of dead material in front of the calorimeter and are thus not applicable for the energies considered here. Nevertheless, the AE1R bank is used in this analysis to check the reliability of the energy scale correction applied. If this correction is sufficient the results of the π^0 cross section should be nearly independent of the energy scale chosen.

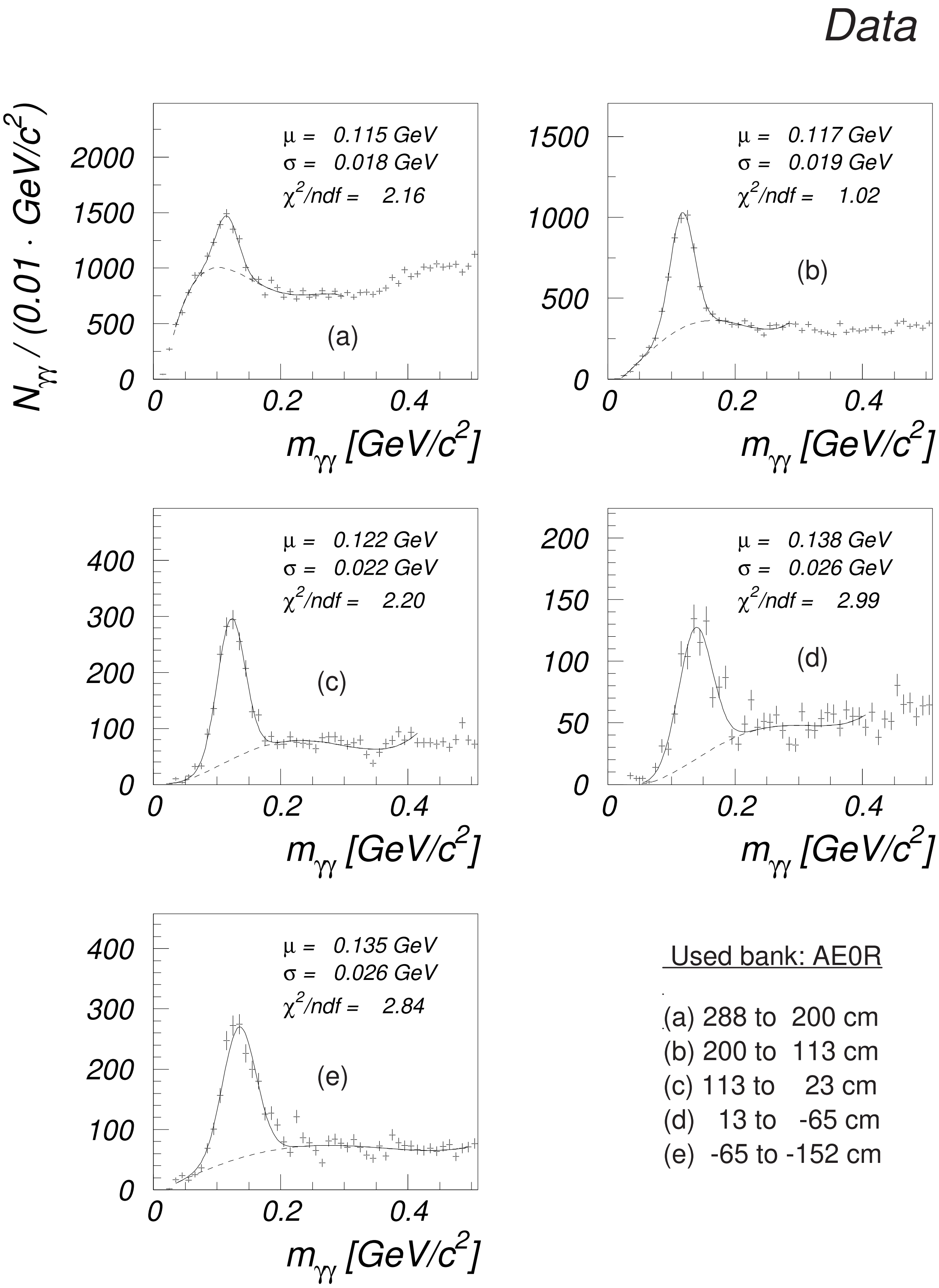

Figure 5.15: *$m_{\gamma\gamma}$ distributions reconstructed from photons where both are recorded in the same LAr wheel (Data). The bank* **AE0R** *is used.*

5.2.2 Energy Scale Correction of the LAr in MC Simulations

For the correction of the energy scale in the simulated events, completely the same procedure as described above for the data has been applied. The behaviour of the π^0 mass measured in the different LAr wheels in data and MC is quite similar for the AE0R and for the AE1R bank. After the correction the deviations of the π^0 masses reconstructed from the AE0R bank or reconstructed from the AE1R bank are at the three percent level. In table 5.4 the values of the π^0 masses measured in different LAr wheel for the MC PYTHIA are listed, and figure 5.16 gives a graphical overview of the measured π^0 masses in data and simulated events for the two energy scales AE0R and AE1R.

AE0R					
wheel	FB2	FB1	CB3	CB2	CB1
corr. factor	1.13	1.14	1.07	0.98	1.01
m_{π^0} [GeV/c^2] before corr.	0.119	0.119	0.127	0.140	0.134
m_{π^0} [GeV/c^2] after corr.	0.131	0.132	0.136	0.137	0.136

AE1R					
wheel	FB2	FB1	CB3	CB2	CB1
corr. factor	1.00	0.92	0.96	0.85	0.86
m_{π^0} [GeV/c^2] before corr.	0.138	0.143	0.141	0.159	0.155
m_{π^0} [GeV/c^2] after corr.	0.135	0.132	0.135	0.139	0.136

Table 5.4: *LAr: π^0 mass reconstructed from photons where both are recorded in the same LAr wheel (PYTHIA).*

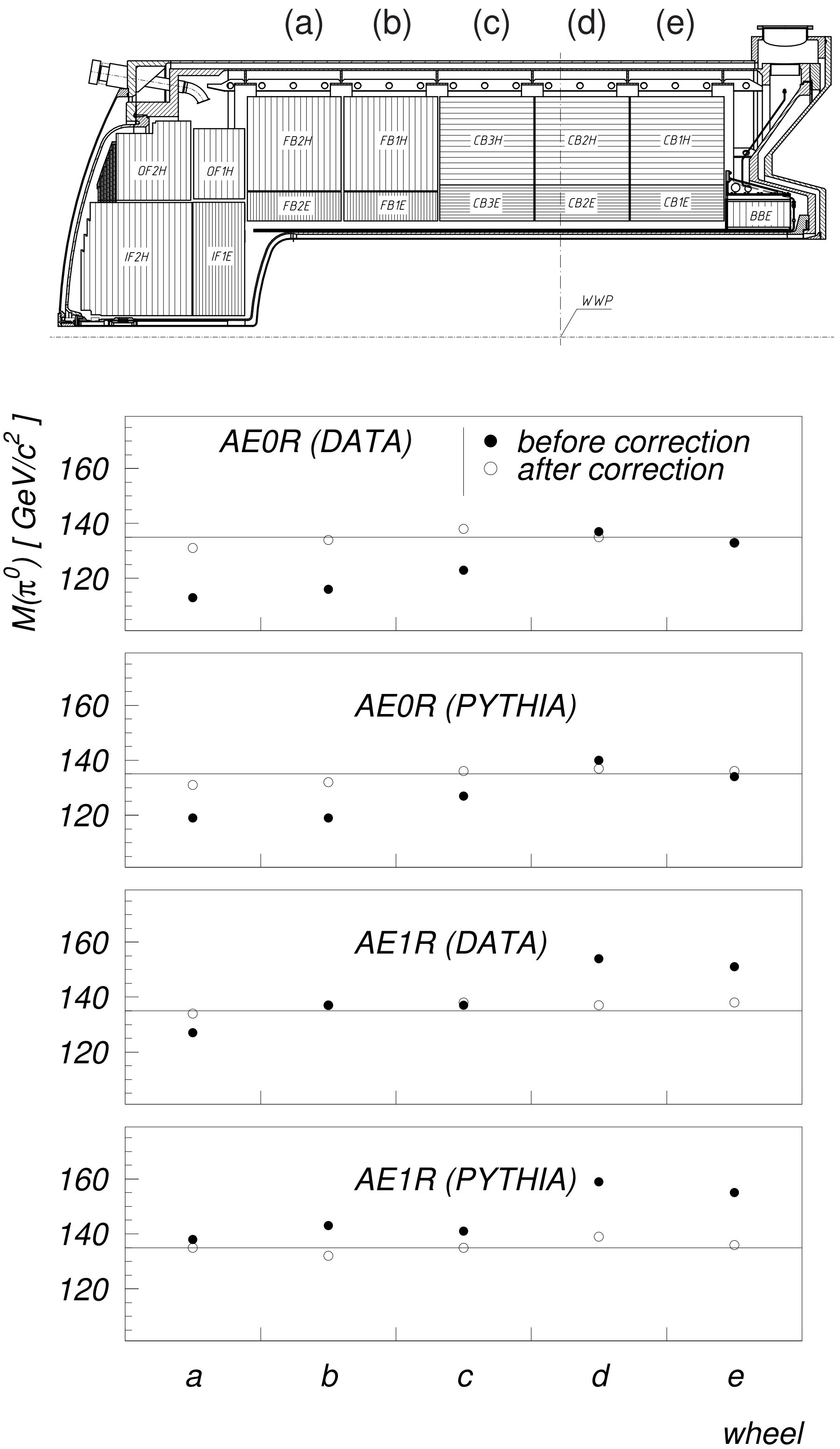

Figure 5.16: *Comparison between data and MC model PYTHIA with respect to the π^0 mass reconstructed from photons flying into the same LAr wheel. The full points are the values of the π^0 mass before the mass correction and the open points are the values of the π^0 mass after the mass correction.*

5.2.3 Comparison of the LAr Data and the Simulated Events

Figure 5.17 shows the comparison of data and reweighted MC PYTHIA concerning the LAr cluster variables explained in the caption of the figures. The MC models have been reweighted with respect to the SpaCal quantities explained in section 5.1.3. The MC models PHOJET and PYTHIA supply a good description of the considered distributions derived from the AE0R and AE1R bank (not shown here).

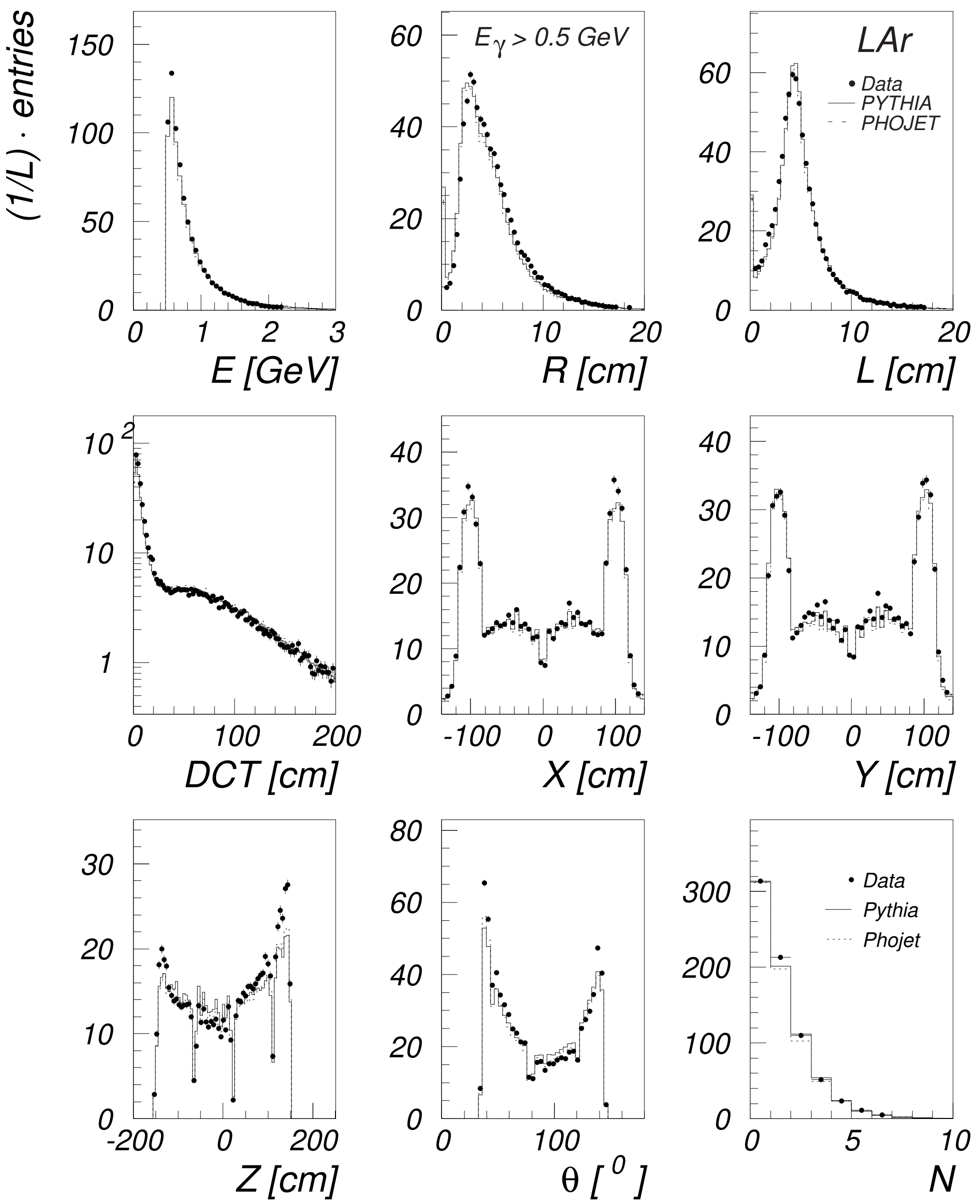

Figure 5.17: *LAr: Comparison of data (points) with reweighted MC PYTHIA 5.722 (full line) and reweighted MC Phojet 1.04 (dotted line). E = Cluster energies, R = Radial cluster extension, L = Longitudinal cluster extension, DCT = Distance of Cluster center of gravity from next Track (DTNV bank), X,Y,Z = Cluster coordinates, θ = Polar-angle, N = Number of cluster cells. Used bank: AE0R.*

5.2.4 Optimisation of the Photon Selection Cuts in the LAr Calorimeter

The procedure of optimising the photon selection cuts in the LAr calorimeter is quite similar to the procedure performed in the SpaCal, described in section 5.1.4. For this calorimeter the studies revealed that the largest effect on the signal-to-background-ratio of the π^0 signal is due to the cut on the distance between the cluster center to the closest track.

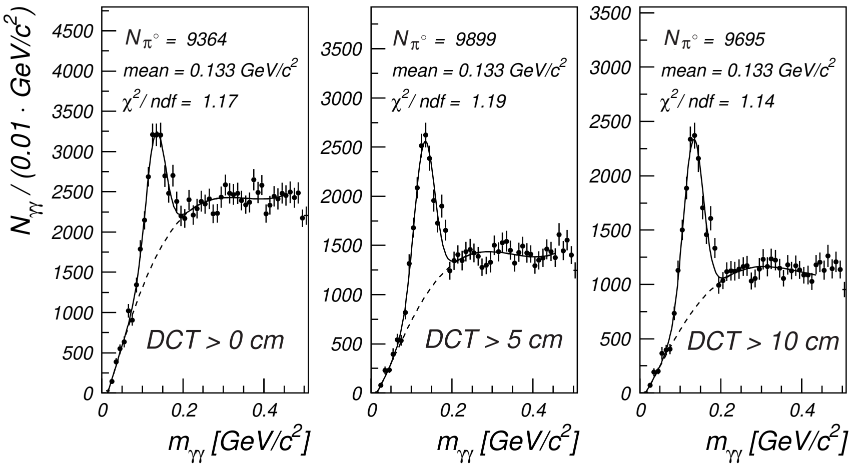

Figure 5.18: *LAr: $m_{\gamma\gamma}$ distributions with different cuts on the distance between the cluster center to the closest track.*

Going from the left to right plot of figure 5.18 the cut on the distance between cluster center and closest track (DCT) is tightened from 0 cm to 10 cm. When tightening this cut the signal becomes more pronounced. Already for the condition $DCT > 5$ cm the π^0 signal is very well pronounced. Therefore, the final analysis cut on this variable is $DCT > 5$ cm. The next plots of figure 5.19 illustrate the effect of the cut on the cluster radius on the $m_{\gamma\gamma}$ spectrum.

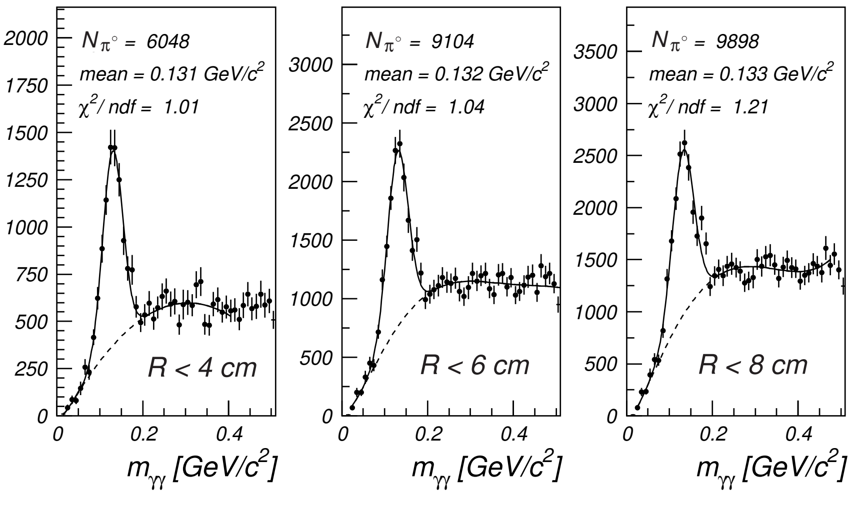

Figure 5.19: *LAr: $m_{\gamma\gamma}$ distributions with different cuts on the cluster radius R.*

In all of these plots the cut on the distance of the cluster center to the closest track of 5 cm is applied. The smaller the cluster radius is chosen the better is the signal-to-background-ratio. When tightening the cut from $R < 8$ cm to $R < 4$ cm the number of π^0s is reduced from roughly 9500 pions for R <8 cm (R = cluster radius) to ≈ 6000 pions for R <4 cm. To keep the number of π^0s as high as possible and due to the clear π^0 signal for the condition R < 8 cm, the latter condition was applied for the photon selection in the LAr. The other cuts listed in table 5.5, which summarizes the final photon selection cuts for photons in the LAr calorimeter and (for comparison) in the SpaCal, have only a small, if not negligible, effect on the improvement of the π^0 signal.

Photon selection cuts	
for the SpaCal	**for the LAr**
$E_{cl} > 0.3$ GeV (π^0)	$E_{cl} > 0.3$ GeV
$E_{cl} > 0.5$ GeV (η)	-
$N_{cell} > 1$	$N_{cell} > 1$
0 cm < R_{cl} < 10 cm	0 cm < R_{cl} < 8 cm
8 cm < RD_{cl} < 75 cm	-
-	$L_{cl} <$ 8 cm
-	$F_{cl} = 1$
-	$DCT >$ 5 cm

Table 5.5: *Cluster selection cuts for photons in the SpaCal (left side) and for the LAr calorimeter (right side). E_{cl} = Cluster energy, N_{cell} = Number of cluster cells, R_{cl} = Cluster radius, RD_{cl} = Radial distance of the cluster center of gravity from the beam line, L_{cl} = Longitudinal cluster extension, F_{cl} = electromagnetic energy fraction, DCT = Distance of the Cluster center from the next Track.*

Chapter 6

The Measurement of the π^0 Cross Section

The previous section showed that the two MC models PHOJET and PYTHIA are able to describe the selected photoproduction events. This allows a determination of all the efficiency and acceptance corrections needed for the measurement of the π^0 production cross section. The cross section is measured as a function of $p_\perp$ and y, the transverse momentum and the rapidity of the π^0s.
The double differential cross section is given by the expression

$$\frac{d^2\sigma}{dp_\perp^2 dy} = \frac{N_{\text{produced}}(\Delta p_\perp, \Delta y)}{2p_\perp \cdot \Delta p_\perp \cdot \Delta y \cdot \Phi \cdot \mathcal{L}} \tag{6.1}$$

Here, N_{produced} is the number of π^0s produced in the kinematical intervals considered ($\Delta p_\perp$, Δy), determined with all efficiency and acceptance corrections, and background subtraction. $\mathcal{L}$ is the integrated luminosity and Φ the flux factor (see section 1.2). N_{produced} can be written as

$$N_{\text{produced}} = \frac{N_{\pi^0} - N_{\pi^0,\text{BG}}}{\epsilon_{\text{eTag}} \cdot \epsilon_{St} \cdot \epsilon_{\pi^0}} \tag{6.2}$$

Here N_{π^0} denotes the number of neutral pions seen by the detector, $N_{\pi^0,\text{BG}}$ the number of π^0s coming from the background events, ϵ_{eTag} the efficiency of the eTag trigger element, ϵ_{St} the efficiency of the subtrigger 50 and 69, respectively, and finally ϵ_{π^0} represents the π^0 reconstruction efficiency.

The photon flux was determined via formula 1.22 to 0.00968 for the interval $0.35 < y_{\text{B}} < 0.65$. From section 4 it is known that the integrated luminosity $\mathcal{L}$ of the minimum bias data taking period of 1997, selected by subtrigger 69, is 300 nb^{-1}, and the integrated luminosity $\mathcal{L}$ of the data of 1996, selected by subtrigger 50, is 4.3 pb^{-1}. The trigger efficiency ϵ_{St} of the subtrigger elements was discussed in section 4.2, both include the eTag trigger element with an efficiency ϵ_{eTag} plotted in figure 4.1. The beam-gas background in photoproduction events was estimated in section 3.6 from pilot bunches to be below 1 %.

This chapter deals with the following quantities, needed for the calculation of the π^0 cross section:

- N_{π^0}, the number of neutral pions
- ϵ_{π^0}, the π^0 reconstruction efficiencies

6.1 The Determination of the Number of π^0 Mesons

The number of π^0s seen in the detector, $N_{\pi^0,\mathrm{Detector}}$, scattered into the intervals $\Delta p_\perp$ and Δy, is derived via a kinematical fit to the two photon invariant mass spectrum. The signal in the $m_{\gamma\gamma}$ spectrum is described by a Gauss function. The fact that the π^0 signal is so close to threshold introduces an uncertainty in the determination of the background. To determine this uncertainty different functions have been used which are listed in table 6.1.

Number	**Function $x = m_{\gamma\gamma}$**
1	$g(x) \cdot P^3(x) \cdot t(x)$
2	$g(x) \cdot P^4(x)$
3	$g(x) \cdot P^4(x) \cdot t(x)$
4	$g(x) \cdot P^5(x)$
5	$g(x) \cdot P^5(x) \cdot t(x)$

Table 6.1: *Functions used for fitting the $m_{\gamma\gamma}$ distributions. For the definition of the functions $g(x)$, $P^i(x)$ and $t(x)$ see below.*

$$
\begin{aligned}
g(x) &= \frac{p_1}{p_2\sqrt{2\pi}} e^{\frac{1}{2}\left(\frac{x-p_3}{p_2}\right)^2} \\
P^i(x) &= p_4 + p_5 \cdot x + p_6 \cdot x^2 + ... + p_{i+4} \cdot x^i \qquad \text{with } i = (3...5) \\
t(x) &= (x - x_0)^{p_{i+5}} \qquad \text{with } 0 < p_{i+5} < 1.
\end{aligned}
$$

The threshold value x_0 was chosen to be the first histogram bin which was not empty.

In the following, the determination of $N_{\pi^0,\mathrm{Detector}}$ is exemplified for π^0s reconstructed with a transverse momentum within the interval $0.6 < p_\perp < 0.9$ GeV/c and the rapidity range $-3.5 < y < -1.5$ covered by the SpaCal.

First the four-momenta and the kinematical variables y and $p_\perp$ of all photon pairs of the SpaCal are calculated, then the kinematical cuts are applied, and finally the invariant mass of the selected photon pairs is determined and filled into a histogram. For each background function listed in table 6.1 the invariant mass spectrum of a certain kinematical interval was fitted several times by slightly varying the initial fit parameters and the fitting intervals. Finally the function with the best χ^2/ndf (**ndf** = **n**umber of **d**egrees of **f**reedom) for each background assumption was selected.
Figure 6.1 depicts the fitted invariant mass spectra in the considered kinematical intervals for the MC models PHOJET and PYTHIA.

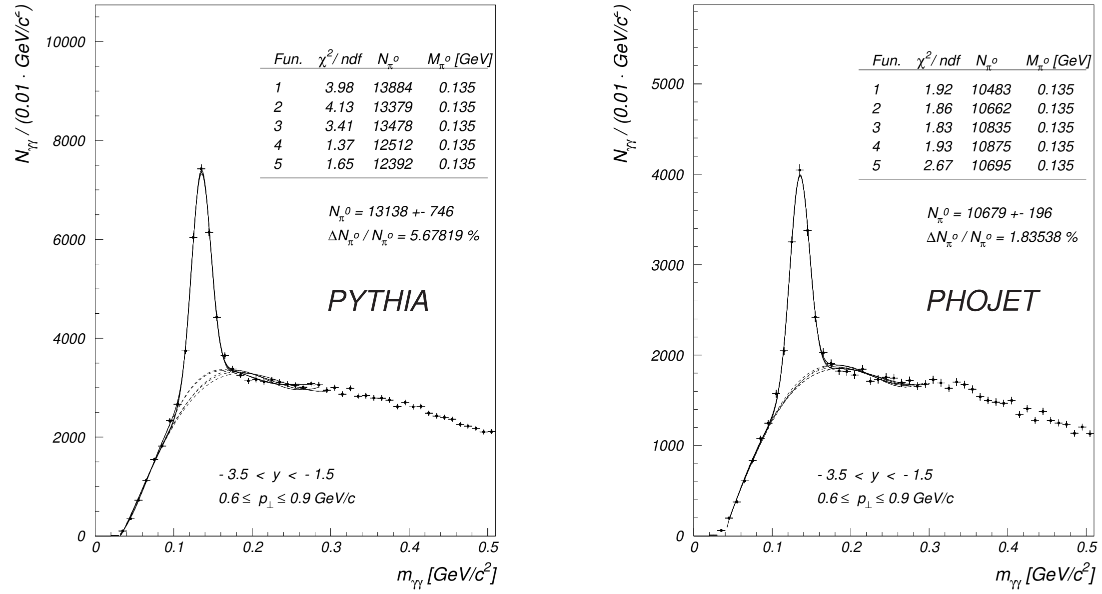

Figure 6.1: *MC PYTHIA: $m_{\gamma\gamma}$ spectra (SpaCal) in intervals of the π^0 transverse momentum fitted by different functions (-3.5 < y < -1.5). Table 6.1 gives the fit function referring to the number given in the plots above.*

After this fitting procedure, the fit parameters for each background assumption are known and thus the final estimate of N_{π^0} from $\int g(x)dx = p_1 = N_{\pi^0,\mathrm{Detector}}(\Delta y, \Delta p_\perp)$ for each interval. In order to take the uncertainties concerning the "true" behaviour of the background into account, the final number of π^0s was assumed do be:

$$N_{\pi^0}(\Delta y, \Delta p_\perp) \;=\; \frac{1}{2} \cdot \left(N_{\pi^0 \, Max}(\Delta y, \Delta p_\perp) + N_{\pi^0 \, Min}(\Delta y, \Delta p_\perp) \right) \tag{6.3}$$

$N_{\pi^0 \, Max\,(Min)}(\Delta y, \Delta p_\perp)$ is the maximal (minimal) number of π^0s supplied by the fit functions. The error on the number of the measured π^0s, $\Delta N_{\pi^0}(\Delta y, \Delta p_\perp)$, was calculated for each bin as the difference between the mean number of π^0s and the minimal number of π^0s:

$$\Delta N_{\pi^0}(\Delta y, \Delta p_\perp) \;=\; N_{\pi^0}(\Delta y, \Delta p_\perp) - N_{\pi^0 \, Min}(\Delta y, \Delta p_\perp). \tag{6.4}$$

The errors $\Delta N_{\pi^0}(\Delta y, \Delta p_\perp)$ vary quite substantially due to the accidental behaviour of the background which strongly influences the fit. In order to get a conservative but reliable estimate for the uncertainty from the fitting procedure, a global error of of 8 % was applied. For the determination of the 8 % error, the distribution of $\Delta N_{\pi^0}/N_{\pi^0}$ for all intervals, in which the cross section is measured, was plotted (see figure 6.2) and the cut on $\Delta N_{\pi^0}/N_{\pi^0}$ was chosen such that at least 90 % of the relative errors derived by the fitting method are below 8 %.

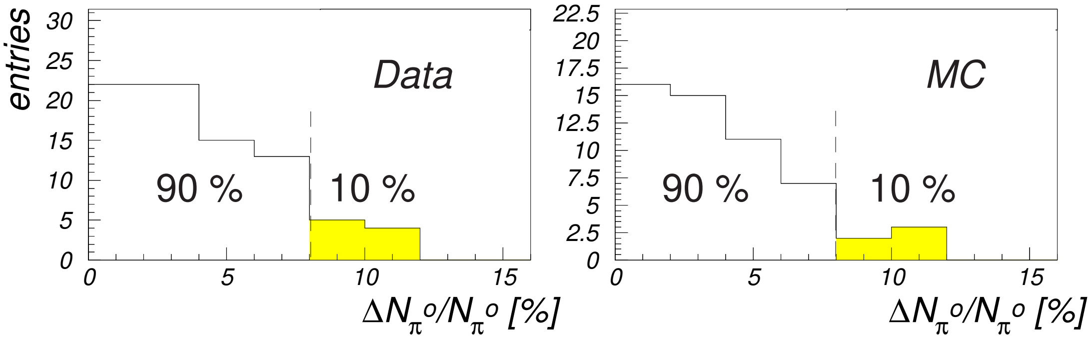

Figure 6.2: *The distribution of $\Delta N_{\pi^0,fit}/N_{\pi^0}$ for all bins in which the π^0 cross section is measured. The dashed line marks the final error on N_{π^0}.*

For the measurement of the π^0 cross section the effect on the number of measured π^0s due to the error on the energy scale of 4 % has to be taken into account. For this purpose the energy of the clusters was increased (reduced) artificially by 4 % and then, as before, the number of π^0s scattered into certain kinematical intervals was derived. For the intervals: -3.5 $< y <$ -1.5 and 0.6 $< p_\perp <$ 0.9 GeV/c, table 6.2 gives an overview of the number of π^0s derived by the fits for the nominal, reduced and increased energy scale, and figure 6.3 shows the corresponding mass distributions.

-3.5 $< y <$ -1.5 and 0.6 $< p_\perp <$ 0.9 GeV/c			
Function	N_{π^0} reduced energy	N_{π^0} nominal energy	N_{π^0} increased energy
1	128019	135663	157479
2	127129	133447	155108
3	126128	131758	159577
4	113976	127876	151895
5	130982	128035	152120
$\rightarrow$	122479 $\pm$ 8503	131770 $\pm$ 3894	153736 $\pm$ 3841

Table 6.2: *The number of π^0s seen in the interval -3.5 $< y <$ -1.5 and 1.5 $< p_\perp <$ 1.8 GeV/c derived by the fit functions with numbers 1 - 5 for the reduced, nominal and increased cluster energy. Table 6.1 gives the fit functions referring to the numbers 1 - 5. The last line represents the number of π^0s derived via formula 6.3 and 6.4 using the functions 1-5.*

With increasing cluster energy, more photons survive the cluster selection cut of 300 MeV. This results in an increasing number of π^0s seen in the kinematical interval. This expected effect is clearly visible in table 6.2 when comparing the left with the right column. The error on the final number of π^0s seen in each interval was associated to the maximal difference between the number of π^0s of the nominal energy to the number of π^0s for the reduced or increased energy, respectively. An upward/downward shift of the energy scale of 4 % lead to an error on the π^0 cross section measurement between (3 - 10) % for the minimum bias data and to an error between (10 - 20) % for the data selected by subtrigger

50. In contrast to subtrigger 69, used for the minimum bias data selection, subtrigger 50 depends strongly on the energy scale of the SpaCal, see figure 4.2. This explains the larger influence of the energy uncertainty on the cross section measurement based on the data selected by subtrigger 50, compared with the minimum bias data. The bin-to-bin error on the energy scale was added in quadrature to the global error of 8 % from the uncertain behaviour of the background.

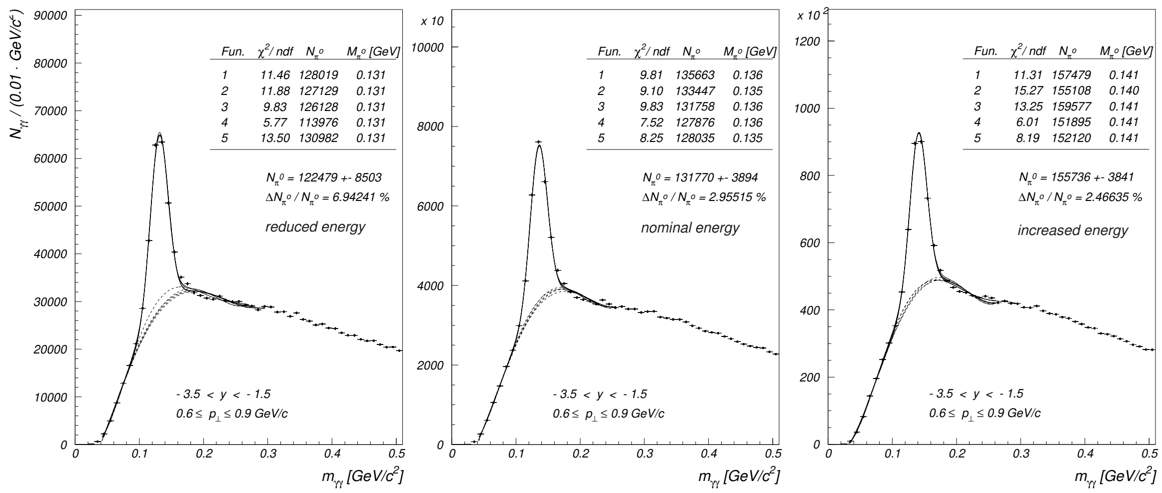

Figure 6.3: *Data: $m_{\gamma\gamma}$ spectra (SpaCal) in intervals of the π^0 transverse momentum (-3.5 < y < -1.5) fitted by different functions. Table 6.1 gives the fit function referring to the number given in the plots above. The cluster energy was artificially reduced by 4 %.*

6.2 π^0 Reconstruction Efficiencies

The π^0 reconstruction efficiencies were calculated with the MC models PHOJET and PYTHIA via formula 6.5:

$$\epsilon_{\pi^0} = \frac{N_{\pi^0,\,\mathrm{Detector}}\,(\Delta x, \Delta y)}{N_{\pi^0,\,\mathrm{Generator}}\,(\Delta x, \Delta y)} \tag{6.5}$$

$N_{\pi^0,\,\mathrm{Generator}}\,(\Delta x, \Delta y)$ is the number of π^0s generated in the intervals $\Delta x, \Delta y$ of the kinematical variables x and y.

$N_{\pi^0,\,\mathrm{Detector}}\,(\Delta x, \Delta y)$ marks the number of π^0s seen after the event selection cuts (see table 4.1) in the detector in the same kinematical range Δx, Δy in which the π^0s have been generated.

For the generators PHOJET and PYTHIA, the π^0 reconstruction efficiencies were calculated and the mean value of both models for each interval in which the π^0 cross section is measured was taken as the final value for the π^0 reconstruction efficiency. The error $\Delta\epsilon_{\pi^0}$ has three contributions:

1)

$$\Delta\epsilon_{\pi^0,\,\mathrm{PHOJET}} = \frac{\Delta N_{\pi^0,\mathrm{Detector}}(\Delta x, \Delta y)}{N_{\pi^0,\mathrm{PHOJET}}(\Delta x, \Delta y)}$$

2)

$$\Delta\epsilon_{\pi^0,\,\mathrm{PYTHIA}} = \frac{\Delta N_{\pi^0,\mathrm{Detector}}(\Delta x, \Delta y)}{N_{\pi^0,\mathrm{PYTHIA}}(\Delta x, \Delta y)}$$

3)

$$\Delta\epsilon_{\pi^0,\,\mathrm{MC}} = |\epsilon_{\mathrm{MC}} - \bar{\epsilon}| \quad \text{with} \quad \bar{\epsilon} = \frac{1}{2} \cdot (\epsilon_{\mathrm{PHOJET}} + \epsilon_{\mathrm{PYTHIA}})$$

The first two sources are due to the uncertainty of the background in the two-photon mass spectra which leads to the error $\Delta N_{\pi^0,\,\mathrm{MC}}$, the error on the number of pions determined via the fitting method, for each MC model used. The third error concerns the MC dependence which is taken into account as the deviation of the mean efficiency of both MC models from that one predicted by PHOJET and PYTHIA, respectively. The final error was calculated by expression 6.6

$$\Delta\epsilon_{\pi^0} = \sqrt{\frac{1}{4} \cdot \left(\Delta\epsilon_{\pi^0,\,\mathrm{PHOJET}} + \Delta\epsilon_{\pi^0,\,\mathrm{PYTHIA}}\right)^2 + \Delta\epsilon^2_{(\pi^0,\,\mathrm{MC})}}, \tag{6.6}$$

the sum of the mean error of the contributions 1) and 2) and the error due to the MC dependence added in quadrature.

The results are given in the appendix of this thesis in tables A.1 and A.2 for the minimum bias data of 1997 and in tables A.3 and A.4 for the data selected in 1996, for all intervals in which the π^0 cross section is measured.

For the minimum bias data of 1997, the π^0 reconstruction efficiencies for the SpaCal range from 22 % to 58 % with a mean value of 39 %. The π^0 reconstruction efficiencies of the data selected in the year 1996 reach from values of 13 % to 62 % with a mean value of 44 %.

The lowest efficiency values of approximately 12 % were found for the LAr calorimeter. In order to understand these characteristics of the LAr calorimeter which lead to an efficiency of 12 %, a TOY simulation (= a very simplified model) of this calorimeter has been written. In the TOY simulation the events were produced by the MC model PYTHIA, adjusted to the HERA kinematics like the full detector simulation. The energies of the photons are smeared with the detector resolution of 12 %$/\sqrt{E/\,\mathrm{GeV}}$. In addition, the following detector characteristics were taken into account step by step

1. the geometry of the LAr calorimeter
2. the minimal energy cut which has to be applied for the noise reduction
3. the cracks of the LAr calorimeter
4. the merging of clusters

For each step the π^0 reconstruction efficiency was calculated as $\epsilon = N_{\pi^0\text{, Simulation step}} / N_{\pi^0\text{, Generator}}$ and compared with the π^0 reconstruction efficiency supplied by the full detector simulation (H1SIM).

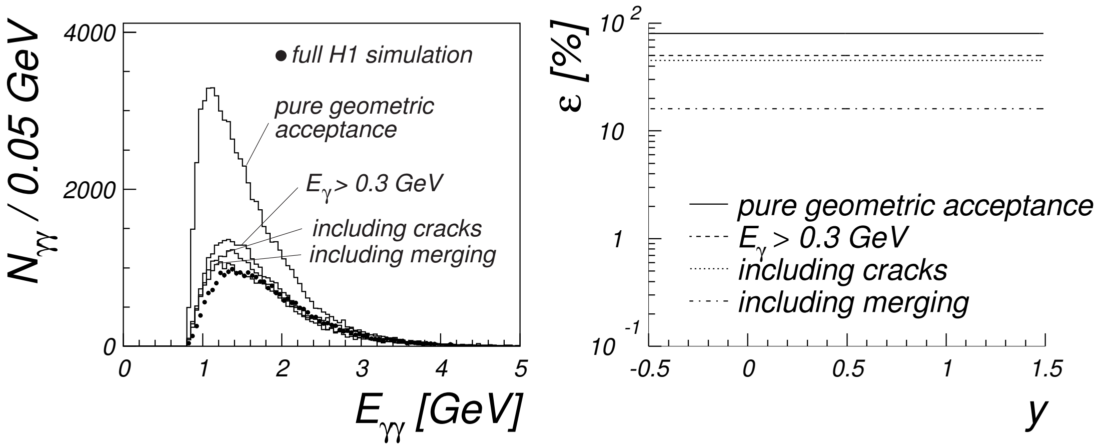

Figure 6.4: *Left side: Comparison of the energy of all two-photon combinations between the TOY (see text) and the full detector simulation. The values of the z-coordinate of the LAr calorimeter were restricted to the range $-150 < z < 200$ cm. Right side: The π^0 reconstruction efficiency (LAr) for the conditions listed in the legend of the plot.*

Figure 6.4 (left side) displays the energy of all two-photon combinations of the LAr calorimeter received by the TOY and the full simulation. Each further inclusion of the conditions listed above slightly improves the agreement between both simulations. Applying all conditions yields only a rough agreement of both simulations. Of course, this is not surprising as not all the subtleties of the LAr detector are considered. For example the size of the cluster cells surely has big effects on the quantities shown. However, the agreement of the TOY and the full simulation is good enough to explain the magnitude of the π^0 reconstruction efficiency.
Figure 6.4 (right side) shows the π^0 reconstruction efficiencies of the full and for each step of the basic simulation. The pure geometrical acceptance is about 80 %. Nearly 40 % of the π^0s are lost due to the cut $E_\gamma > 0.3$ GeV. The inclusion of the cracks of the LAr calorimeter reduces the efficiency from 50 % to 45 %. The clusters associated with the photons in the TOY simulation were merged if the their distance was smaller than 12 cm. This effect reduces the π^0 reconstruction efficiency from 45 % to 16 %, a value of the π^0 reconstruction efficiency which is comparable to the value supplied by the full detector simulation.

6.3 Purities and Stabilities of the Kinematical Intervals for the π^0 Cross Section Measurement

In this context two other variables are of interest: the purity and the stability of the π^0 reconstruction for the intervals in which the cross section is measured. The purity and stability of the bin i is defined as:

$$\text{Purity of } i\text{th bin} = \frac{N_i^{\text{rec. + gen.}}}{N_i^{\text{rec}}} \tag{6.7}$$

$$\text{Stability of } i\text{th bin} = \frac{N_i^{\text{rec. + gen.}}}{N_i^{\text{gen}}} \tag{6.8}$$

The purity is the number of π^0s generated and reconstructed in the ith bin divided by the number π^0s reconstructed in the same bin. It is a measure for the number of π^0s which migrated from the neighbouring bins into the bin considered due to the finite spatial and energy resolution of the detector.
The stability gives the complementary information of the number of π^0s migrated from the bin considered into the neighbouring bins.
Low values of purity and stability of a bin can be explained by a bin width chosen too small with respect to the resolution of the detector. Very stable bins with low values of purity, and vice versa very pure but unstable bins are more problematic. They can indicate that the binning chosen for the measurement of the variable is unsuited, or they can indicate unexpected detector effects.
There exists no strict rule which values of purity or stability a certain bin must have in order to be not excluded from the analysis. These values should rather be considered as additional information about the quality of the measurement [BAS97].

In order to count the number of π^0s generated and reconstructed in the ith bin, one has to know which particle refers, or which particles refer, to which cluster. Due to spatial and energy resolution effects of the detector, several particles can belong to one cluster. In this case they are scattered very close to each other into the corresponding subdetector. There exists no meta-information about the cluster-particle relation in the log-files of the event simulation program, which allows one to monitor a particle from its generation to the final recording of its characteristics in the corresponding detectors. To get the information about the relation of the generated four-momenta of the π^0s and the corresponding cluster quantities, a simplified method was used. First, only events with one π^0, generated in the SpaCal or the LAr calorimeter, were selected, then the variable

$$f\,(E, P_x, P_y, P_z) = E/P_z \cdot \arctan\,(P_y, P_x), \tag{6.9}$$

was calculated for the generated π^0s ($f_{\text{gen.}}$) and the reconstructed one ($f_{\text{det.}}$). The function $f(E, P_x, P_y, P_z)$ was chosen due to its strong dependence on each component of the four-momentum. Finally the difference $f_{\text{gen.}} - f_{\text{det.}}$ was determined and filled into a histogram shown on the left side of figure 6.5.

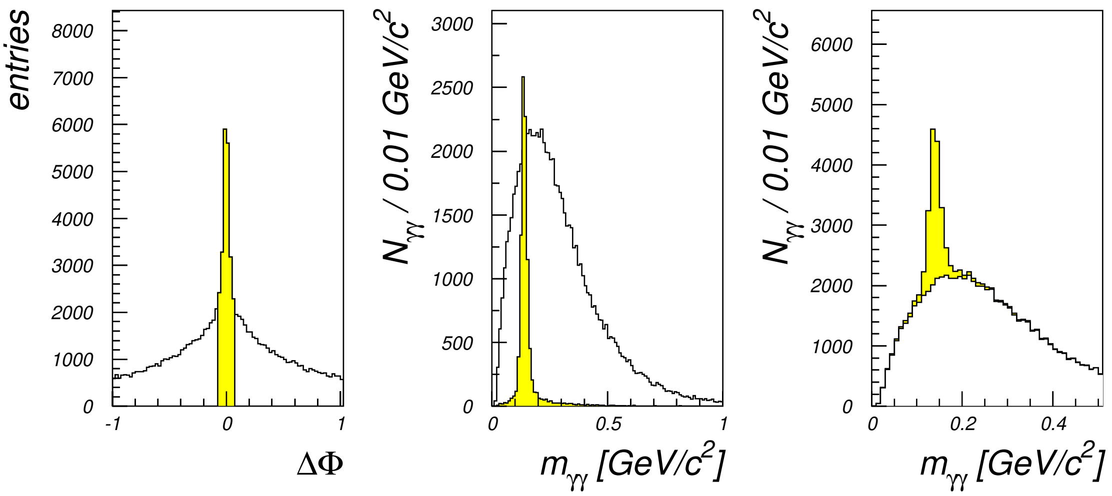

Figure 6.5: *Left side: the difference $f_{gen.} - f_{det.}$ for the π^0s found in the SpaCal. Middle: two-photon mass spectra with photon candidates having a strong correlation to generated photons (grey coloured) and two-photon mass spectrum were no correlated photon on generator level could be found. Right side: the sum of the mass spectra shown in the middle plot.*

This distribution has a clear grey shaded peak around zero generated by the π^0s which have approximately the same four-vectors on generator and on detector level. The photons belonging to the π^0s within this peak are marked so that mass spectra with the marked and unmarked photons could be produced. The resulting spectra are shown in the middle of the figure 6.5. The complete absence of a signal in the two-photon spectrum of the unmarked photons (white distribution) indicates that the presented selection method of π^0s works properly on detector level, as the clear π^0 peak shows, generated by the marked photons. The mass spectrum on the right side of figure 6.5 is the sum of the two mass spectra in the middle (which is identical to the mass spectrum generated by all photon candidates in the events with one π^0). With this π^0 selecting technique, $N^{\text{rec. + gen.}}$ can be calculated for each bin in which the cross section is measured, and via the formulas 6.7, 6.8 the purity and stability values can be determined. The results are summarized in tables 6.3 and 6.4.

y ∈	$p_\perp$ [GeV/c] ∈			
	$[0.2, 0.6]$	$[0.6, 0.8]$	$[0.8, 1.0]$	$[1.0, 2.0]$
$[-3.5, -2.8]$	(80 ± 1) %	(67 ± 5) %	-	-
$[-2.8, -2.4]$	(84 ± 1) %	(75 ± 2) %	(69 ± 5) %	(75 ± 9) %
$[-2.4, -2.0]$	(84 ± 1) %	(75 ± 1) %	(74 ± 2) %	(83 ± 2) %
$[-2.0, -1.4]$	(80 ± 1) %	(66 ± 1) %	(64 ± 2) %	(80 ± 2) %
$[-0.5, 1.0]$	-	-	(28 ± 1) %	(45 ± 1) %

Table 6.3: *Stability for the π^0 reconstruction in different bins of the pion transverse momentum $p_\perp$ and rapidity y.*

y $\in$	$p_\perp$ [GeV/c] $\in$			
	$[0.2, 0.6]$	$[0.6, 0.8]$	$[0.8, 1.0]$	$[1.0, 2.0]$
$[-3.5, -2.8]$	(88 ± 1) %	(52 ± 4) %	-	-
$[-2.8, -2.4]$	(82 ± 1) %	(68 ± 2) %	(53 ± 4) %	(47 ± 5) %
$[-2.4, -2.0]$	(81 ± 1) %	(71 ± 1) %	(68 ± 2) %	(70 ± 3) %
$[-2.0, -1.4]$	(83 ± 1) %	(67 ± 1) %	(66 ± 2) %	(82 ± 2) %
$[-0.5, 1.0]$	-	-	(41 ± 1) %	(76 ± 2) %

Table 6.4: *Purity for the π^0 reconstruction in different bins of the pion transverse momentum $p_\perp$ and rapidity y.*

The stability values for the π^0 rapidities below -1.5 are on the 75 % level. The lowest stability value of 28 % is in the interval 0.8 $< p_\perp <$ 1.0 GeV/c and -0.5 $< y <$ 1.0. The corresponding value of the purity is 41 %.

6.4 Discussion of Systematic Errors

In this section the systematic errors discussed so far are summarized, while the problems not yet treated are discussed. The errors on the results of this analysis are dominated by systematical sources while uncertainties due to statistics are negligible. The main sources of systematic errors are listed here:
1) The uncertainty on the efficiency of subtrigger 50 used to select the data in 1996 is (conservatively) estimated to be 1 % as shown in the legend of figure 4.2. The cross checks are based on subtrigger 43 which is completely independent of the SpaCal triggers (described in section 4.2).
2) The uncertainty of the electron tagger efficiency is 4 % for 1996 and 6 % for 1997 (see section 4.3).
3) The contribution of π^0s from beam-gas events, discussed in section 3.6, has an uncertainty below 1 % for the data selected in 1996 and for the minimum bias data of 1997.
4) Uncertainty of the energy scales for the LAr and SpaCal calorimeters (explained in chapter 5): An upward / downward shift of the scale by 4 % increases / reduces the cross sections by around 10 % for the minimum bias data and by around 20 % for the data selected in 1997 (st50).
5) The number of π^0s is derived from a fit of a Gaussian, plus a function describing the background, to the two photon invariant mass distribution. As the π^0 signal is close to threshold, the fit is rather sensitive to changes in the rise of the background. The studies presented in section 6.1 lead to an estimation of the uncertainty from this source of 8 %.
6) The uncertainty on the π^0 reconstruction efficiency, due to the same source as in 5), is estimated to be also 8 %, see figure 6.2.
7) The model dependence of the efficiency, determined by comparing the results derived from PYTHIA and PHOJET, leads to systematic uncertainties varying from bin to bin between 1 % and 15 % as described in section 6.2.
8) Finally, the integrated luminosity is known to a precision better than 2 % for both data samples.

Two objections could be raised against this analysis yet. The first objection concerns the poor description of the cluster radius distribution by the MC models used and the second one the MC dependence of this analysis. The following two sections discuss these items.

6.4.1 Cluster Merging

It was mentioned in subsection 5.1.4 that the poor description of the cluster radius by the MC models is less important for the π^0 analysis since no cut is applied on this variable. Nevertheless, one could argue that a larger cluster radius in the data in comparison with the MC models could result in different performances of the cluster reconstruction software. An illustrative example of this problem are two decay photons of a π^0 flying very close to each other into the SpaCal. Both particles generate showers which are transformed into clusters by the reconstruction routines. It can happen that the two clusters overlap so that the reconstruction routines have to decide which cell belongs to which cluster. Due to the larger cluster radius in the data this problem appears more often in the data than in the MC. Assuming that the cluster constructing routines tend to attribute the questionable cell energy between two clusters to the cluster with less energy, the the result is a disagreement between the reconstructed π^0 mass in the data and the MC models. In the worst case the two photons are merged into one cluster in the data but not in the MC. In the end, the π^0 reconstruction efficiencies determined via the MC models would be incorrect.

To estimate the influence of this effect on the π^0 reconstruction efficiencies the opening angle $\Omega_{\gamma\gamma}$ of all possible two-cluster combinations in the mass band of the π^0 ($0.1 < m_{\gamma\gamma} < 0.17$ GeV/c^2) is plotted in figure 6.6 in intervals of the transverse momentum of the cluster pairs and in figure 6.7 in intervals of their rapidity.

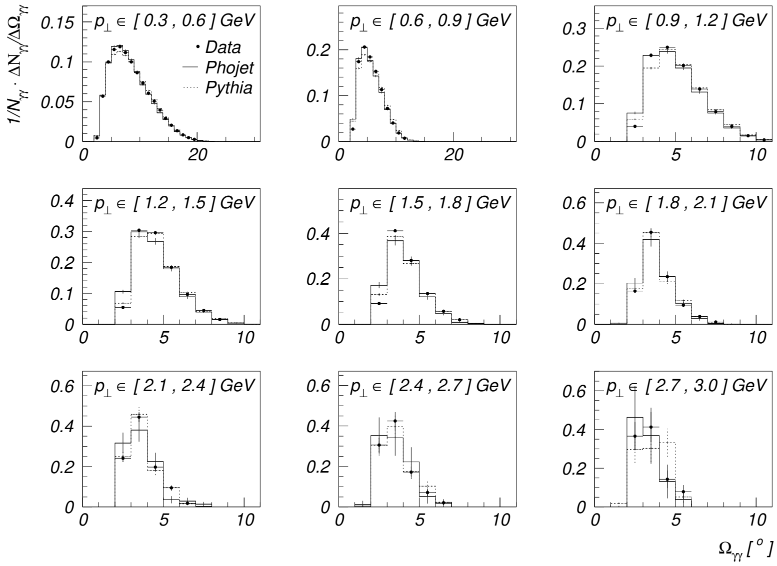

Figure 6.6: *Opening angle $\Omega_{\gamma\gamma}$ of all possible two-cluster combinations in the mass band of the π^0 ($0.1 < m_{\gamma\gamma} < 0.17$ GeV/c^2) in intervals of the transverse momentum of the cluster pairs (SpaCal).*

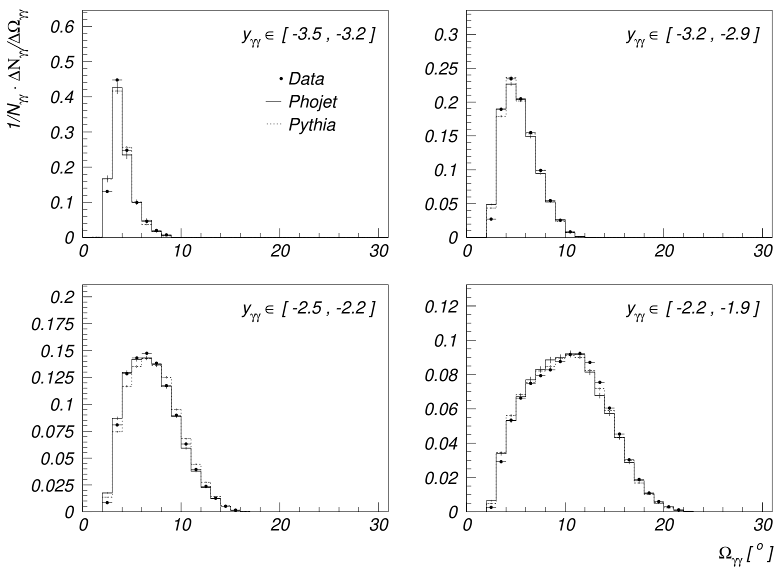

Figure 6.7: *Opening angle $\Omega_{\gamma\gamma}$ of all possible two-cluster combinations in the mass band of the π^0 ($0.1 < m_{\gamma\gamma} < 0.17$ GeV/c^2) in intervals of the rapidity of the cluster pairs (SpaCal).*

It can be seen from the figures above that there is only a small effect of the deviation between the cluster radius in the data and the cluster radius in the MC on the opening angle of the cluster pairs. The argument connecting the opening angle of the cluster pairs with the problem of the cluster merging is as follows: a larger cluster radius in the data results in a larger opening angle between the photon pairs. Thus the excess of cluster pairs with very small opening angles in the MC models includes the number of cluster pairs which have been merged in the data but not in the MC. The ratio of this excess over the distribution of all cluster pairs normalised to one in each kinematical interval considered yields, multiplied by a factor of 100, the deviation in percent. In table 6.5 the mean deviation of PHOJET and PYTHIA from the data is listed.

$E_{\gamma\gamma,\pi^0}$ [GeV]	0.5 to 1.5	1.5 to 2.5	2.5 to 3.5	3.5 to 4.5
excess [%]	0	0	0	0.12 ± 0.04

$E_{\gamma\gamma,\pi^0}$ [GeV]	4.5 to 5.5	5.5 to 6.5	6.5 to 7.5	7.5 to 8.5
excess [%]	3.2 ± 0.3	7.9 ± 0.7	5 ± 1	10 ± 2

$p_{\perp,\pi^0}$ [GeV/c]	0.3 to 0.6	0.6 to 0.9	0.9 to 1.2	1.2 to 1.5
excess [%]	0.35 ± 0.10	2.3 ± 0.6	2.7 ± 0.9	3 ± 2

$p_{\perp,\pi^0}$ [GeV/c]	1.5 to 1.8	1.8 to 2.1	2.1 to 2.5	2.5 to 2.8
excess [%]	6 ± 2	3 ± 2	5 ± 5	–

y_{π^0}	-3.5 to -3.0	-3.0 to -2.5	-2.5 to 2.0	-2.0 to 1.5
excess [%]	3.6 ± 1.0	1.8 ± 0.4	1.02 ± 0.5	1.4 ± 0.6

Table 6.5: *SpaCal: The excess of cluster pairs with an opening angle too small to be seen in the data, averaged over the MC models PHOJET and PYTHIA. The excess represents the upper limit of the number of cluster pairs being merged in the data but not in the MC.*

Clearly, a smaller cluster radius in the MC results in a smaller opening angle of the cluster pairs. Therefore the excess listed in table 6.5 has no one-to-one correlation to the number of cluster pairs being merged in the data but which are not merged in the MC. However, this excess includes the number of merged clusters in the data, and so it represents an upper limit. On the average this limit is below 3 % in the intervals of $p_{p_{\perp,\pi^0}}$ and y_{π^0} where the π^0 cross section is measured. It becomes stronger in the lowest π^0 rapidity interval, in the $p_\perp$ range above 1.5 GeV/c and for energies of the photon pairs above 5 GeV. Thus, mainly three points of the double differential cross section are effected by the problem of the cluster merging, these points are measured in the intervals:

1.) -3.5 $\leq y_{\pi^0} \leq$ -2.8, $\quad 0.6 \leq p_{\perp\,\pi^0} \leq 0.8$ GeV/c,
2.) -2.8 $\leq y_{\pi^0} \leq$ -2.4, $\quad 0.8 \leq p_{\perp\,\pi^0} \leq 1.0$ GeV/c,
3.) -2.8 $\leq y_{\pi^0} \leq$ -2.4, $\quad 1.0 \leq p_{\perp\,\pi^0} \leq 2.0$ GeV/c.

The comparison of the π^0 mass of the data (see figure 6.9) in these intervals with the corresponding π^0 mass of the simulated events (figure 6.10) shows that the pion mass reconstructed here is about 145 MeV/c^2, deviating about 7 % from the nominal mass value. An investigation of the opening angles and of the energies of the two photons coming from a π^0 in these intervals explains the deviation. The opening angles of the two photons are very small ($\approx 3°$) and the energy difference between them is larger than 3

GeV. This means a high energy photon is scattered very close to a low energy photon into the SpaCal leading to the problem of overlapping clusters. Since the π^0 mass reconstructed here is too large the clustering routines tend to overestimate the energy of the low energy cluster as suggested above. This effect is well reproduced by the simulated events, and thus no additional correction is necessary.

6.4.2 Effect of the Cuts on E_1 and RD_1 onto the results

Another systematic concern regards the cut on the most energetic cluster in the SpaCal E_1, which has to be above 1.6 GeV, and the cut on RD_1, the radial distance of the center of gravity of this cluster from the beam line. These cuts are necessary to guarantee a trigger efficiency of subtrigger 50 of at least 40 % (see section 4.2). The cuts on E_1 and RD_1, strongly decrease the π^0 reconstruction efficiencies due to the number of events lost by these cuts.

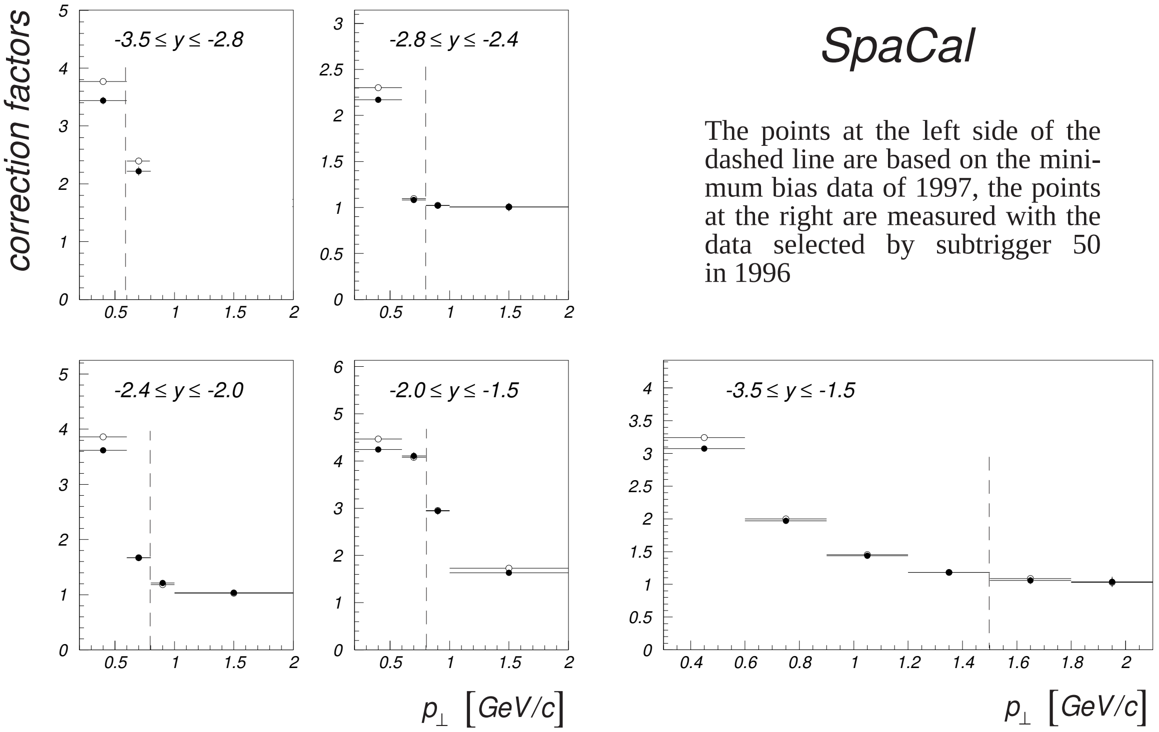

Figure 6.8: *Correction factors for the number of events lost due to the cut on the most energetic cluster in the SpaCal and on the radial distance of its center of gravity from the beam line.*

The factors shown in figure 6.8 were determined with the help of the MC models PHOJET and PYTHIA via the ratio of the number of π^0s on generator level in each interval after applying the cuts on E_1 and RD_1 over the full number of π^0s in each interval. With increasing values of $p_\perp$ the correction factors approach a value of one. The points at the right side of the plots are based on the data selected by subtrigger 50 in 1996. For these the correction factors are clearly below 2, with the exception of the points measured in the intervals:

$$-3.5 < y < -2.8 \quad \text{and} \quad 0.4 < p_\perp < 0.6 \text{ GeV/c},$$
$$-2.0 < y < -1.5 \quad \text{and} \quad 0.6 < p_\perp < 0.8 \text{ GeV/c},$$

here the correction factors are around 2.5.

The biggest advantage of the minimum bias data is that they allow a measurement of the π^0 cross section in the more central region covered by the LAr calorimeter. Subtrigger 50 relies mainly on energy deposited in the SpaCal, and might therefore introduce a bias in favour of events which populate the backward region. In physics terms, this might favour events from so called “resolved photon” processes and disfavour events from so called “direct photon” processes. This bias would naturally affect events with π^0s reconstructed in the LAr calorimeter which is not used in subtrigger 50.

6.5 The Bin-Center Correction

For the presentation of the results, a bin-center correction has been performed. This was done with the method proposed by Lafferty and Wyatt in [LAF95] which mainly consists of three steps:

1. fit the histogram by a function f,
2. determine the value of the y coordinate at the point of intersection between f and the histogram bin
3. the bin center is the inverse value of f at the point of intersection

For the π^0 cross section as a function of $p_\perp$ a power law of the form $f(x) = a \cdot (1 + x/b)^c$ has been used, and for the π^0 cross section as a function of the rapidity y the function $f(x) = a + b \cdot x^2$.

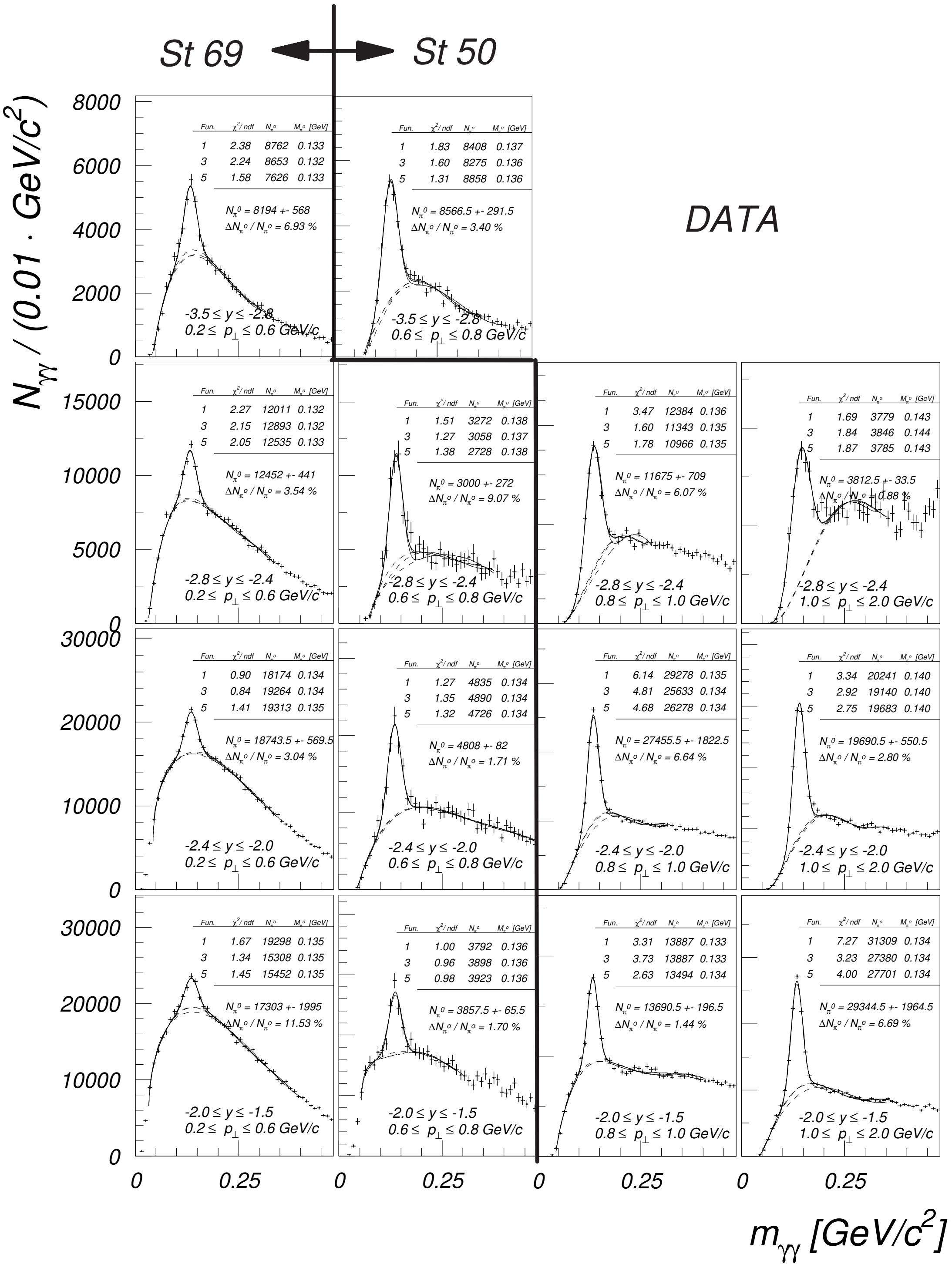

Figure 6.9: *$m_{\gamma\gamma}$ spectra (SpaCal) in intervals of the π^0 transverse momentum and the π^0 rapidity fitted by different functions. Table 6.1 gives the fit function referring to the number given in the plots. On the left of the marked line: mass spectra based on the minimum bias run of 1997 (St 69). On the right of the emphasised line: mass spectra based on data, selected by subtrigger 50 (St 50) in 1996.*

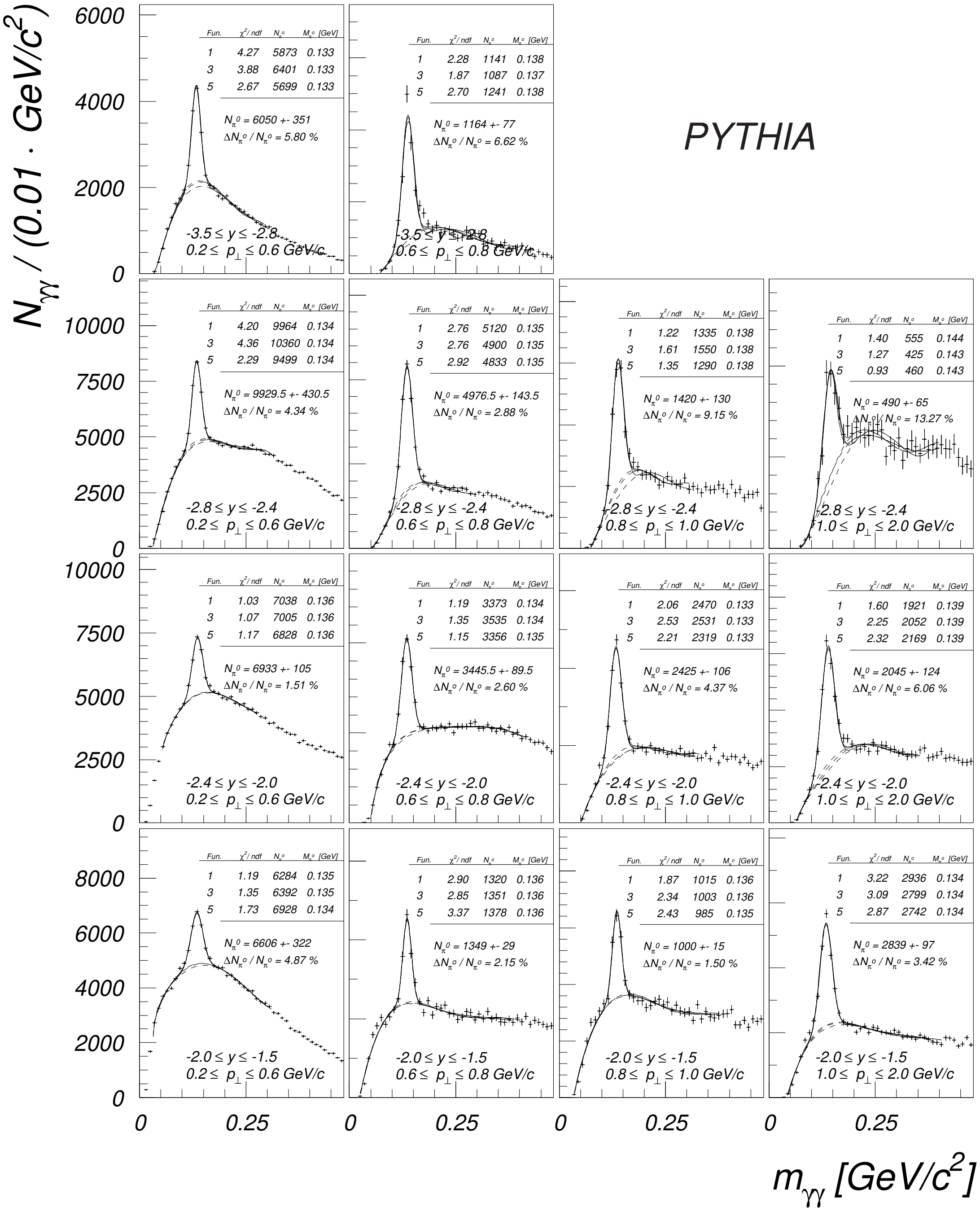

Figure 6.10: *MC PYTHIA: $m_{\gamma\gamma}$ spectra (SpaCal) in intervals of the π^0 transverse momentum and in intervals of the π^0rapidity fitted by different functions. Table 6.1 gives the fit function referring to the number given in the plots.*

6.6 Results

The cross section for inclusive neutral pion production in γp interactions is displayed in Fig. 6.11 as a function of the π^0 rapidity, for four intervals of the transverse momentum, and in Fig. 6.12 as a function of $p_\perp$, for five intervals of rapidity. The data are summarized in Table 6.6. Missing entries are due to lack of statistics (low y, high $p_\perp$) or large background (central region, low $p_\perp$). Rapidity values given are measured in the laboratory frame, i.e. $y = -3.5$ corresponds to a rapidity of -5.5 as seen in the γp CM system. Errors quoted are the sum of statistical and systematic errors, added in quadrature, in which the systematic uncertainties dominate. Bin-center corrections have been applied in deriving the cross section values.
The values from the H1 charged particle measurement, after a bin center correction, have been added in Fig. 6.11 and Fig. 6.12 for comparison. The cross sections have been corrected for charged "non - pions" by subtracting a fraction of 17.5 % as derived from the PYTHIA and PHOJET predictions, and divided by the isospin factor 2.
The entries in Fig. 6.11 (full triangles) were derived from the curve fitted to the charged particle differential cross section w.r.t. transverse momentum published in [ABT94] (see appendix B), while the entries in Fig. 6.11 (full triangles) represent the original data points from the paper quoted. The charged particle data cover the pseudorapidity (see equation 1.25) range $|\eta| \leq 1.5$. The ep cross sections given in [ABT94] have been converted into γp cross sections by virtue of the appropriate flux factor. The agreement is excellent in the kinematical ranges covered by both analyses. Fig. 6.12 demonstrates the additional phase space region accessed with the neutral pion analysis.
The model predictions according to the PHOJET and PYTHIA simulations are also shown in Figs. 6.11 and 6.12, with satisfactory agreement, especially for PYTHIA. PHOJET predicts slightly too large a π^0 rate.
Transverse momentum spectra in high energy hadron - hadron collisions are successfully described by a power law ansatz of the form

$$\frac{d^2\sigma}{dp_\perp^2\, dy} = A \cdot (1 + p_\perp / p_{\perp 0})^{-n} \ . \tag{6.10}$$

This QCD inspired ansatz, which is based on the Constituent Interchange Model (CIM) [BLA78], was designed to describe transverse momentum spectra of centrally produced particles. Accordingly, it fits well the H1 spectra measured for charged particles in the pseudorapidity range $|\eta| < 1.5$ [ABT94].

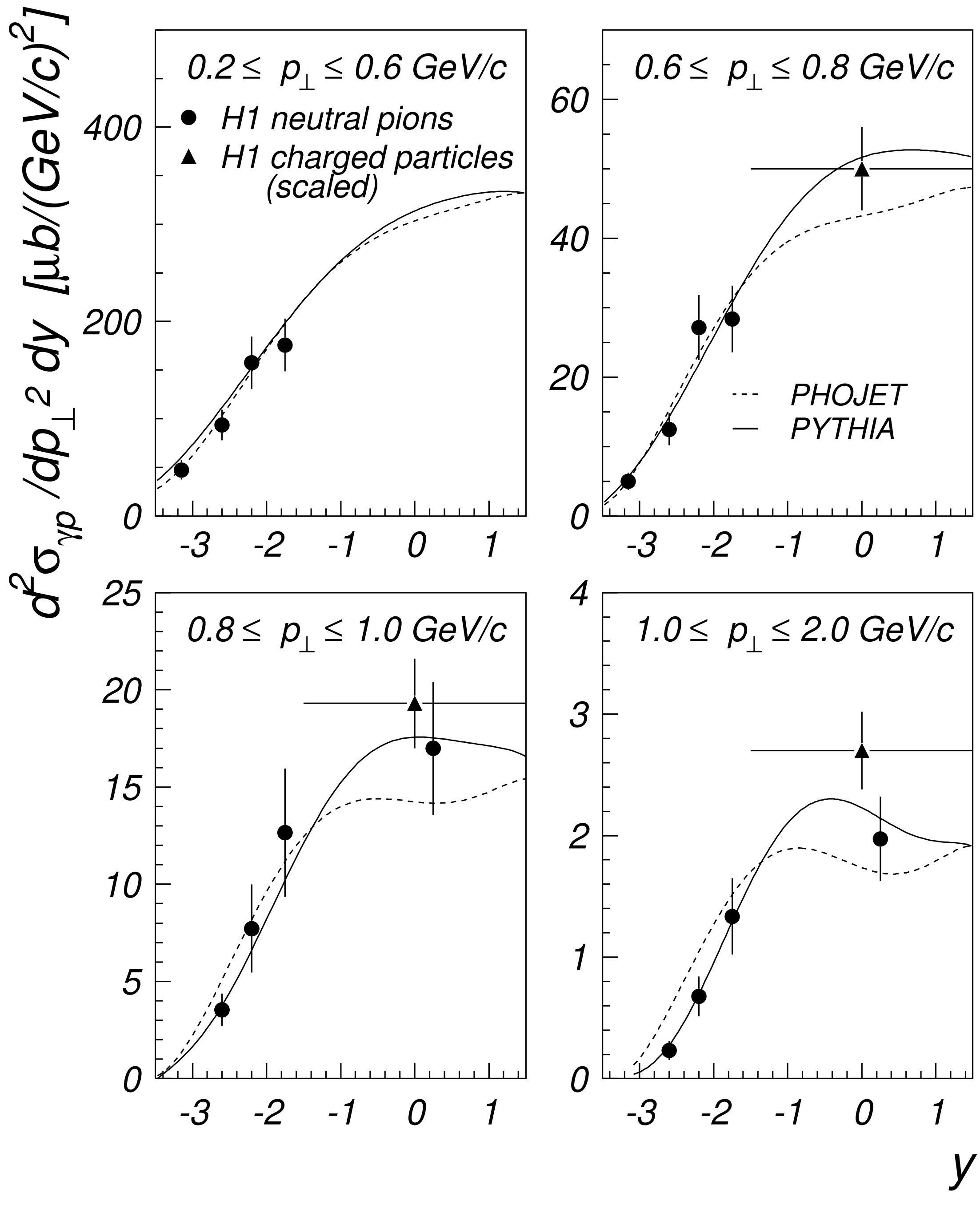

Figure 6.11: *Inclusive π^0 photoproduction cross section as a function of laboratory rapidity y in intervals of transverse momentum $p_\perp$ (full circles), for $Q^2 \leq 0.01$ GeV^2 and $0.35 < y_{\mathrm{B}} < 0.65$. The triangles are the corresponding cross section values for charged pions, derived from [ABT94] by subtracting a fraction of 17.5% to account for the "non-pion" contribution, and then dividing by the isospin factor 2 (see text). The curves are the predictions of the PHOJET (dashed) and PYTHIA (full) event generators for neutral pions.*

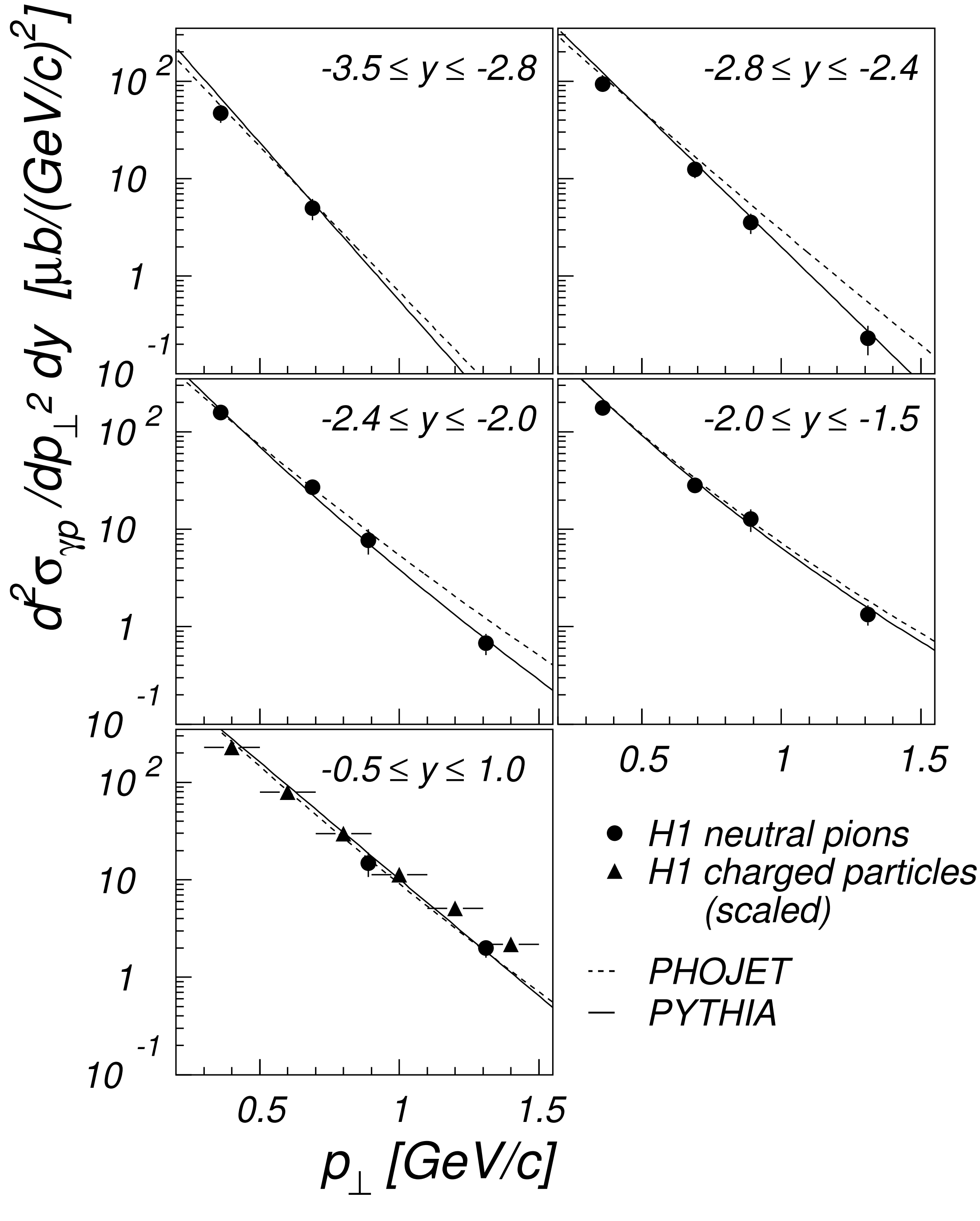

Figure 6.12: *Inclusive π^0 photoproduction cross section as a function of transverse momentum $p_\perp$ in intervals of laboratory rapidity y (full circles). The triangles are the corresponding cross section values for charged pions in the pseudorapidity range $|\eta| \leq 1.5$, derived from [ABT94] by subtracting a fraction of 17.5% to account for the "non-pion" contribution, and then dividing by the isospin factor 2 (see text). The curves are the predictions of the PHOJET (dashed) and PYTHIA (full) event generators for neutral pions.*

The fit to the charged particle spectrum yields a value of $n = 7.1 \pm 0.2$ (with $p_{\perp 0} = 0.63$ GeV/c). In recent papers of the ZEUS [DE95a] and H1 [ABT99] Collaborations, similar values for the power are quoted, namely n = 7.25 ± 0.03 (ZEUS; for $p_\perp > 1.2$ GeV/c, with $p_{\perp 0} = 0.54$ GeV/c) and n = 7.03 ± 0.07 (H1, 1999; for $p_\perp > 2$ GeV/c, with $p_{\perp 0} = 0.63$ GeV/c). This is in agreement with observations made in many hadron-hadron experiments. (See e.g. [BUE73] for centrally produced π^0s at various center-of-mass energies at the CERN ISR, and [ARN82] for measurements performed at $\sqrt{s} = 540$ GeV at the CERN SPS.)

y	$p_\perp$ [GeV/c]			
	$[0.2, 0.6]$ (0.36)	$[0.6, 0.8]$ (0.69)	$[0.8, 1.0]$ (0.89)	$[1.0, 2.0]$ (1.31)
$[-3.5, -2.8]$ (-3.15)	47 ± 10	5.0 ± 1.2	-	-
$[-2.8, -2.4]$ (-2.6)	94 ± 16	12 ± 2	3.6 ± 0.8	0.23 ± 0.08
$[-2.4, -2.0]$ (-2.2)	158 ± 27	27 ± 5	8.0 ± 2.0	0.68 ± 0.17
$[-2.0, -1.5]$ (-1.75)	176 ± 27	28 ± 5	12.9 ± 3.4	1.34 ± 0.32
$[-0.5, +1.0]$ (0.25)	-	-	16.9 ± 3.5	1.97 ± 0.35

y	$p_\perp$ [GeV/c]					
	$[0.2, 0.6]$ (0.34)	$[0.6, 0.9]$ (0.73)	$[0.9, 1.2]$ (1.03)	$[1.2, 1.5]$ (1.33)	$[1.5, 1.8]$ (1.63)	$[1.8, 2.1]$ (1.93)
$[-3.5, -1.5]$	114 ± 20	12.5 ± 2.4	2.0 ± 0.4	0.47 ± 0.15	0.14 ± 0.05	0.04 ± 0.01

Table 6.6: *Inclusive π^0 photoproduction cross sections $d^2\sigma/dp_\perp^2 dy$ ($\mu b/(GeV/c^2)$) for different bins in the π^0 transverse momentum $p_\perp$ and rapidity y. In addition to the interval limits, the bin centers are quoted.*

The transverse momentum spectrum of π^0s, integrated over the laboratory rapidity range covered by the SpaCal, i.e. $-3.5 < y < -1.5$, is shown in Fig. 6.13 a.

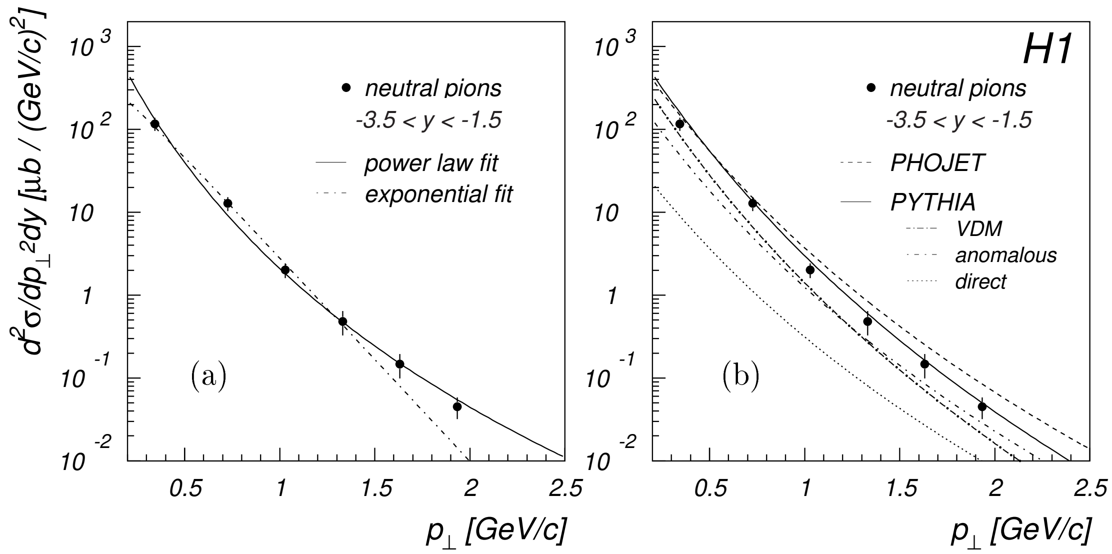

Figure 6.13: *(a) Inclusive π^0 photoproduction cross section as a function of $p_\perp$ (circles), for the rapidity region $-3.5 < y < -1.5$. The dash-dotted curve is a fit of an exponential to the data in the range $0.3 < p_\perp < 1.6$ GeV/c; the full curve is the result of a power law fit (see text). (b) Same cross section as in (a) but this time compared to predictions of PHOJET and PYTHIA. In addition, the decomposition (PYTHIA) into VDM, anomalous, and direct contributions is shown.*

The measurements presented here have been performed in the backward region at larger negative rapidities where phase space effects begin to be visible, causing a damping of transverse momentum spectra. This leads to a reduction of the magnitude of the cross section and to a steepening of the $p_\perp$ distribution. The power law ansatz does, nevertheless, satisfactorily describe the shape of the spectrum if the parameter $p_{\perp 0}$ is fixed to the value found in [ABT99], namely $p_\perp = 0.63$ GeV/c. The fit results in a value for the power of $n = 8.0 \pm 0.2$ ($\chi^2/\mathrm{ndf} = 0.85$).
Comparing the neutral pion and charged particle $p_\perp$ spectra, e.g. from Ref. [ABT99], suggests that in the π^0 data above 1.5 GeV/c the influence of hard scattering effects becomes visible which leads to a hardening of the transverse momentum distribution. In soft hadronic interactions, the $p_\perp$ spectra are known to follow a steep exponential distribution as predicted e.g. by the Thermodynamic Model [HAG83]. Fitting the function

$$\frac{d^2\sigma}{dp_\perp^2 dy} = a \cdot \exp(-b \cdot \sqrt{p_\perp^2 c^2 + m_{\pi^0}^2 c^4}), \tag{6.11}$$

in the complete $p_\perp$-range yields $b = (5.7 \pm 0.3)$ GeV^{-1} ($\chi^2/\mathrm{ndf} = 1.0$). The value found for the slope b is typical for soft hadronic interactions. Fit errors reflect the errors on the data points which are dominated by systematics.
This exponential fit does indeed well describe the region of low transverse momenta. (Taking the "Thermodynamic Model" literally, one derives an "interaction temperature" of $(2.19 \pm 0.12) \cdot 10^{12}$ K from the value of the slope.) Above $p_\perp \approx 1.5$ GeV/c, however, the exponential form does not follow the data, in contrast to the above quoted power

law ansatz. In the light of the measurements performed with charged particles, this is interpreted as an indication of the onset of hard parton–parton scattering processes.
Fig. 6.13 b shows again the cross section as a function of $p_\perp$, this time in comparison with the model predictions of PYTHIA and PHOJET. The agreement with PYTHIA is fairly better than that with PHOJET. Also shown are the separate PYTHIA predictions for the "resolved" (separated into "Vector Dominance" and "anomalous") and "direct" photon contributions. The anomalous photon contribution describes the flattening of the spectrum around $p_\perp = 1.5$ GeV/c which is attributed to the onset of hard scattering processes. The direct component is smaller than the resolved one by roughly one order of magnitude.
The manifestation of a possible intrinsic transverse momentum $k_\perp$ of partons inside the photon (in its hadronic phase) has been investigated using the generator PYTHIA. PYTHIA offers the choice of several distributions for the parameter $k_\perp$: A Gaussian, an exponential, and a "power law" ansatz, see above. All three parametrisations have been used in varying the parameter defining their widths, namely between $k_{\perp,0} = 100$ MeV/c and $k_{\perp,0} = 2.8$ GeV/c. The results have been quantified by fits to the data.
The largest influence on the predicted shape of the y distribution appears in the highest $p_\perp$ interval. This interval, together with the curves predicted by PYTHIA for the Gaussian, exponential, and power law parametrisation, is shown in Fig. 6.14.

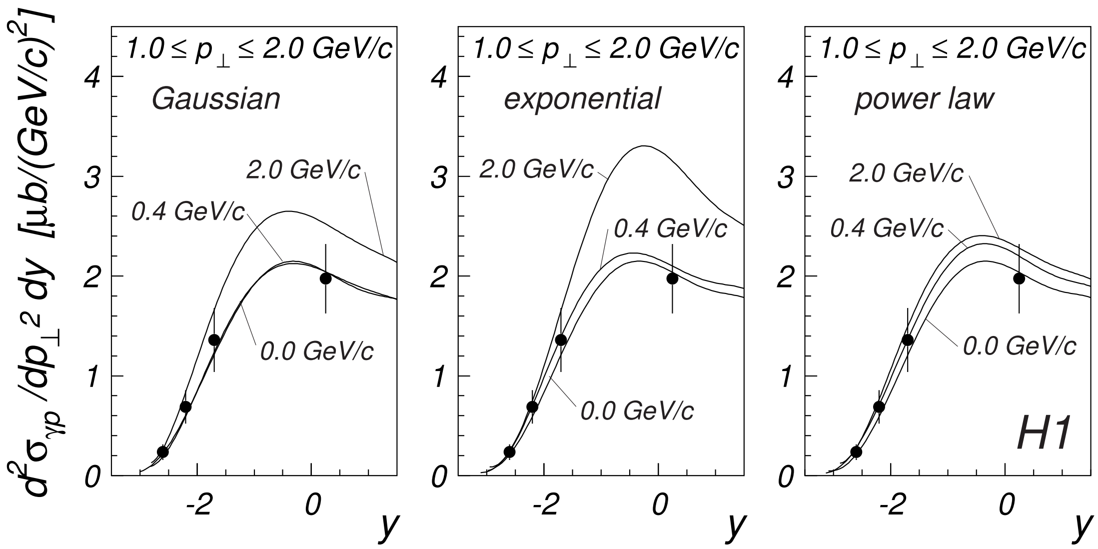

Figure 6.14: *The π^0 cross section as a function of the π^0 rapidity y for the $p_\perp$ range indicated in the figure. The curves are predictions of PYTHIA, labelled with the corresponding $k_{\perp,0}$ values, as described in the text.*

Increasing the parameter $k_{\perp,0}$ leads to drastic deviations of the predictions from the measured cross sections for the Gaussian and exponential parametrisations, but has only a small effect when the QCD-favoured power law ansatz is used. The reason is that the Gauss and exponential functions are strongly damped with increasing $k_\perp$, while $\langle k_\perp^2 \rangle$ becomes infinite for the power law function [SJO94]. PYTHIA therefore uses the $p_\perp$ value defining the hard scale as cutoff parameter, thus constraining the $k_\perp$ spectrum to rather low values so that the influence of a varying $k_{\perp,0}$ is less distinct.

Quantifying the results by a χ^2 leads to the distributions shown in Fig. 6.15. Clearly, large values of $k_{\perp,0}$ are excluded by the Gauss and exponential parametrisations, and also the power law ansatz favours low values of $k_{\perp,0}$. Even a vanishing $k_{\perp,0}$ is consistent with the data.

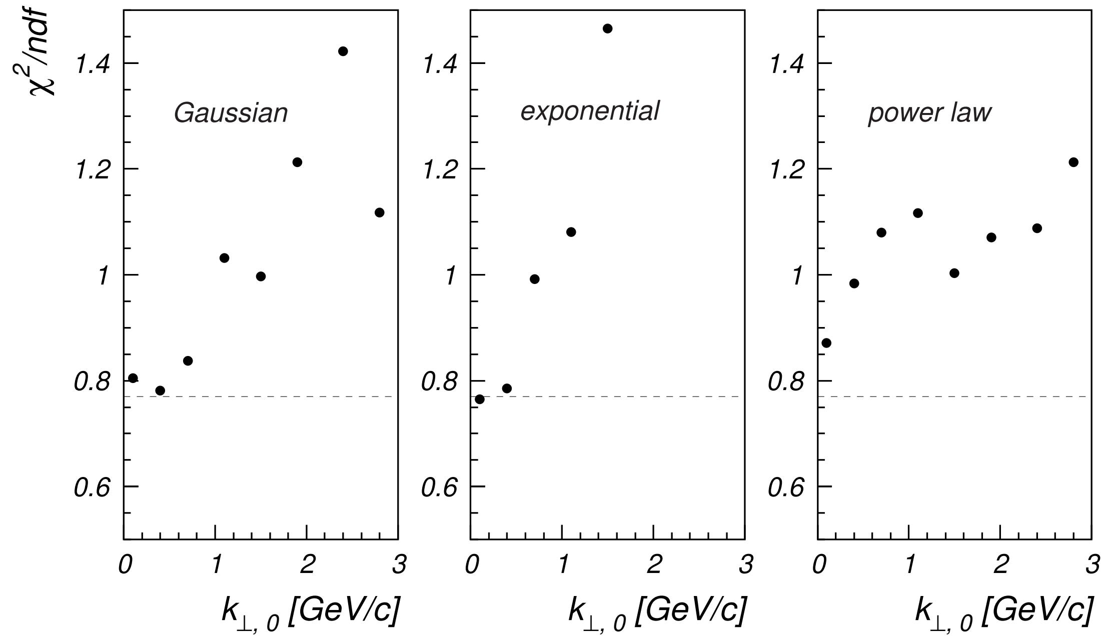

Figure 6.15: *χ^2/ndf as a function of the "primordial" intrinsic $k_\perp$ assuming a Gaussian, exponential and power law $k_\perp$ distribution. The χ^2 was obtained taking into account all data points from the double differential cross sections shown in Fig. 6.11 and 6.12 .*

Finally and for completeness, the behaviour of the distribution of the Feynman variable x_F has been investigated, with x_F defined as the fraction p_L/p_L^{max} in the phase space region covered, where p_L is the pion's momentum component parallel to the beam axis in the γp CM frame, and p_L^{max} its maximally possible value.
The cross section values are shown in Table 6.7. In figure 6.16, the differential cross section $d\sigma/dx_F$ is displayed. There is good agreement with the model prediction of PYTHIA and PHOJET.

y	x_F					
	$[0.1, 0.15]$ (0.125)	$[0.15, 0.2]$ (0.175)	$[0.2, 0.25]$ (0.225)	$[0.25, 0.3]$ (0.275)	$[0.3, 0.4]$ (0.348)	$[0.4, 0.6]$ (0.493)
$[-3.5, -1.5]$	477 ± 67	279 ± 43	209 ± 35	131 ± 19	65 ± 12	19 ± 5

Table 6.7: *Inclusive π^0 photoproduction cross sections $d\sigma/dx_F$ (μb) in intervals of x_F, in the rapidity range $-3.5 < y < -1.5$. In addition to the interval limits, the bin centers are quoted.*

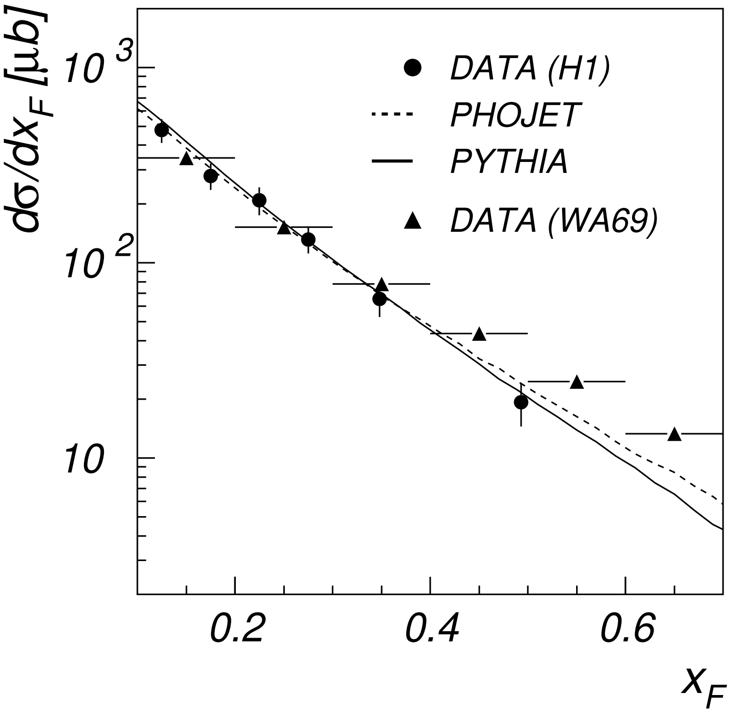

Figure 6.16: *Inclusive π^0 photoproduction cross section as a function of Feynman x. The curves are the predictions of the PHOJET (dashed) and PYTHIA (full) modells. The H1 data, at $\sqrt{s_{\gamma p}} \approx 208$ GeV, as well as the MC model predictions, are obtained in the rapidity range $-3.5 < y < -1.5$. The data of the Omega Photon Collaboration (WA69), at $\sqrt{s_{\gamma p}} \approx 12.3$ GeV, were derived as described in appendix C.*

In figure 6.16 are also shown data from the Omega Photon collaboration [APS91], obtained in fixed target γp collisions with an average photon energy of 80 GeV (corresponding to $\sqrt{s_{\gamma p}} = 12.3$ GeV). From this CM energy and the π^0 mass one derives a CM rapidity range of up to 4.5 units, available for neutral pions. These cross sections of inclusive π^0 photoproduction, available in ref. [DUR] as $Ed^3\sigma/dp^3$ in bins of x_{F} and $p_\perp$, have been converted to cross sections differential in x_{F}, by integrating over $p_\perp$ in each bin (see appendix C)[1] of x_{F}. The two experiments are in good agreement, although small differences are seen in shape and normalisation. These differences can be qualitatively understood from the difference in rapidity range; the cuts $-3.5 < y < -1.5$ (corresponding to $-5.5 < y < -3.5$ in the γp CM) reduces the H1 π^0 cross section at both large and small x_{F}, as can be seen in figure 6.17

[1] In the lowest bin of $p_\perp$ and x_{F}, where a measurement is missing in [DUR], the corresponding measurement from the data set with average beam energy 140 GeV has been used.

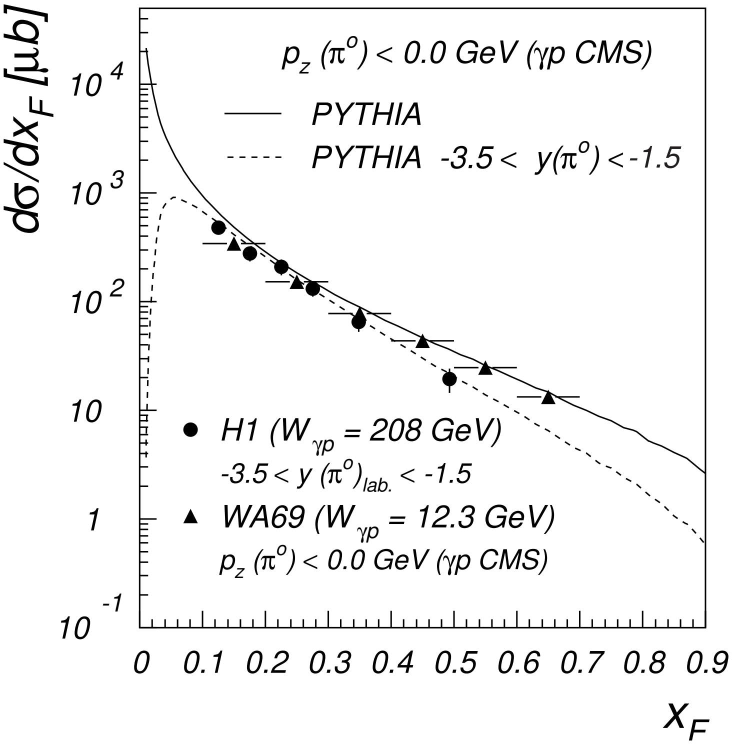

Figure 6.17: *The same data points as shown in figure 6.16 but this time also compared to the x_F distribution of PYTHIA for all π^0s scattered into the backward hemisphere in the γp CMS system ($p_{z,\,CMS} < 0.0$ GeV).*

This reduction is only partly compensated by the expected increase due to the increase of the total cross section between the two CM energies (factor ~ 1.3 [PDG98] and see figure 1.4).

Finally, one may ask whether it is justified to compare the x_F distribution of WA69 with the x_F distribution measured in this analysis. At the fixed target experiment (WA69) the γp CM energy $W_{\gamma p}$ ranges from 10.7 GeV to 13.7 GeV with a mean value of 12.3 GeV. In this analysis $W_{\gamma p}$ covers a 22 times larger interval namely, from 177.7 GeV to 242.1 GeV. Thus each interval of the measured cross section may have another mean value of $W_{\gamma p}$. In this context the comparison of the π^0 cross section with the H1 charged particle analysis is less problematic since both measurements cover roughly the same range in $W_{\gamma p}$. Section 6.6.1 studies the dependence of the measured π^0 cross sections on $W_{\gamma p}$.

6.6.1 The Dependence of the π^0 Cross Section on the CM Energy of the γp System

$W_{\gamma p}$ can be calculated via $W_{\gamma p} \approx \sqrt{y_B s_{ep}}$ (compare section 1.2). Due to the acceptance of the electron tagger the variable y_B is restricted to $0.35 < y_B < 0.65$ (see table 4.1) which corresponds to the interval $177.7 < W_{\gamma p} < 242.1$ GeV. To study the influence of this wide range onto the π^0 cross section, the mean value of $W_{\gamma p}$ is plotted in figure 6.18 (based on the MC PYTHIA) as a function of the π^0 transverse momentum $p_\perp$ and of the Feynman variable x_F.

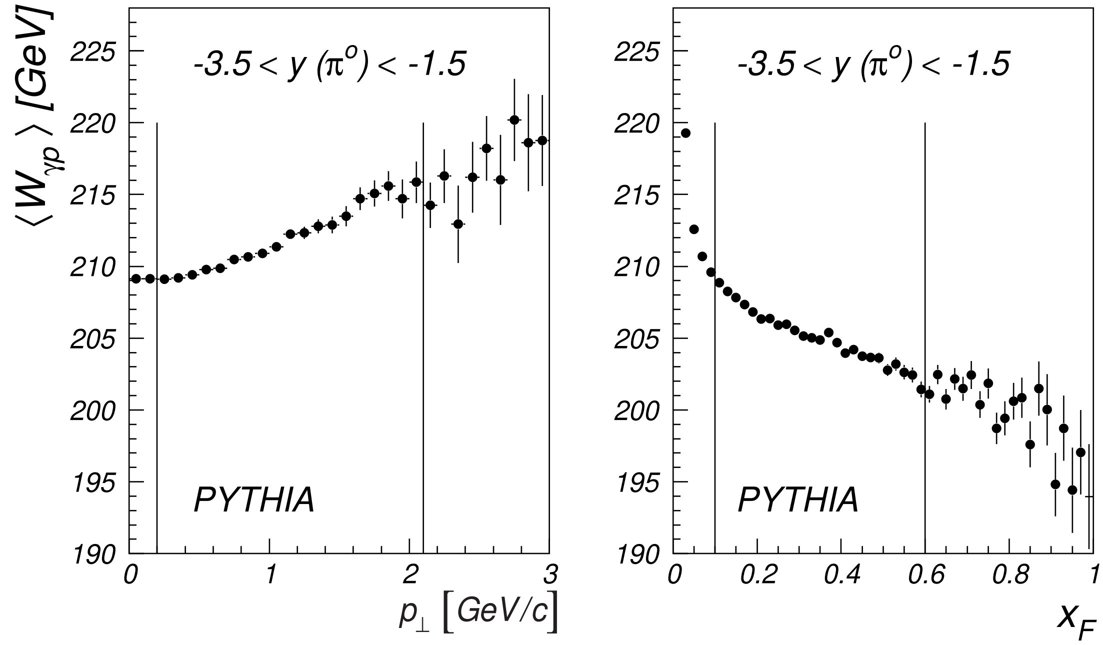

Figure 6.18: *PYTHIA:* $\langle W_{\gamma p}\rangle$ *as a function of the* π^0 *transverse momentum and as a function of* x_{F}. *The region within the two vertical lines of each plot mark the range covered by this measurement.*

The mean value of 208 GeV for $W_{\gamma p}$, already mentioned several times in this thesis, is derived from the mean value of the y_{B} distribution of the minimum bias data. Also the y_{B} distributions generated by PYTHIA and PHOJET result in a mean value of $W_{\gamma p}$ close to 208 GeV. The deviations from this value become larger with increasing values of $p_\perp$ and decreasing values of x_{F}. Within the kinematical region of the neutral pion measurement, these deviations are below the 3 % level. They can be explained by the fact that high $p_\perp$ values preferentially are produced at higher values of $W_{\gamma p}$. Higher values of $p_\perp$ correspond to low values of p_{L} and thus to small values of x_{F} as illustrated in the plots above. Compared to the clearly larger effects of the different y ranges of both measurements on the shape and the normalisation of the x_{F} distribution, the 3 % effect due to varying mean values of $W_{\gamma p}$ was neglected.

Chapter 7

The Measurement of the η Cross Section

The results of the π^0 cross section measurement encourage a similar measurement with η mesons in order to study differences between the production mechanisms of both mesons. The measurement of the η cross section is based completely on data selected by subtrigger 50 in 1996. Since no clear η signal in the backward region of the LAr calorimeter is visible, only the SpaCal has been used for the η cross section measurement. The limited statistics of the minimum bias run of 1997 does not allow one to perform this measurement. The determination of the η cross section was performed in analogy to the determination of the π^0 cross section. Therefore, this chapter mainly focuses on these items where both measurements slightly differ due to the different properties of both mesons.

7.1 Different Kinematical Properties of π^0 and η Mesons

π^0 and η mesons have different masses and branching ratios for their decays into two photons. The π^0 with a mass of about 135 MeV decays into two photons with a branching ratio of 99 %, while the η with a mass of 548 MeV, four times heavier than the π^0 mass, decays into two photons with a branching ratio of about 39 %. Already these differences explain the low number of η mesons in the data compared to the neutral pions, and they result in a different probability for being detected in the SpaCal. Figure 7.1, based on the PYTHIA MC, shows the opening angle Ω between the decay photons of the π^0 and η mesons as a function of the energy $E_{\gamma\gamma}$ of the corresponding mother particles. Only the π^0 and η mesons within the kinematical intervals $-3.5 < y < -1.5$ and $0.2 < p_\perp < 2$ GeV/c of the cross section measurements were selected. Due to the higher mass, the opening angles between the decay photons of the η mesons are larger than the opening angles of the π^0 mesons. The horizontal lines mark the minimal and maximal opening angles between two clusters, associated with the photon candidates, which can be measured by the SpaCal. Photons of the neutral pion decays, scattered into the SpaCal with an opening angle below 3°, generate overlapping clusters in this calorimeter. Thus, this plot illustrates that the merging of two clusters starts for π^0s with an energy above 5 GeV while the η analysis is not affected by this problem. The maximal opening angle of two photons which can be measured by the SpaCal is around 50° due to its limited radial extension.

As can be seen in figure 7.1 the limitation of the opening angle Ω to values below 50° is of minor importance for the detection of both mesons in the considered kinematical intervals. Moreover, it shows that the minimal energies of the π^0 (η) mesons flying into the SpaCal is around 0.6 GeV (1.4 GeV).

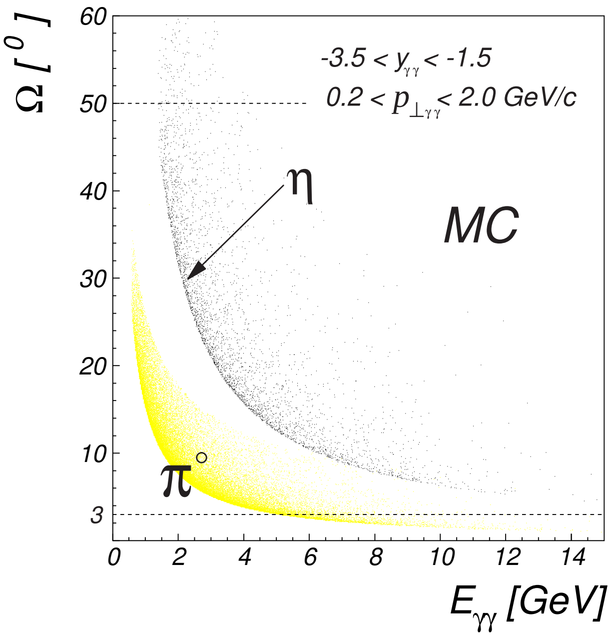

Figure 7.1: *PYTHIA: Opening angles of the* π^0 *and* η *decay photons as a function of the energy of the corresponding mother particles. The black lines mark the acceptance region of the SpaCal for the opening angles between photons which were produced perpendicular to the beam axis at the decay of the meson. Only* π^0 *and* η *mesons within the kinematical range* $-3.5 < y_{\gamma\gamma} < -1.5$ *and* $0.2 < \pi_{\perp\gamma\gamma} < 2.0$ *GeV/c were selected.*

7.2 The Determination of the Number of η Mesons

The cuts applied in the photon selection for the η analysis are listed in table 5.5. They agree with the selection cuts for photons applied in the π^0 cross section measurement with the only difference of a slightly increased cut on the minimal cluster energy, necessary to see a clear η signal in the SpaCal.

The plots of figure 7.2 present the η signal as seen in the SpaCal in those bins in which the η cross section is measured. In contrast to the π^0 signal the η signal is not close to threshold so that the description of the background is less problematic. To estimate the error due to the fitting procedure for deriving the number of ηs, the signal was fitted with a Gaussian function and the background with a polynomial of third order. The width of the Gaussian was varied between 0.028 GeV/c^2 and 0.038 GeV/c^2 resulting in an uncertainty of the number of ηs of about 7 % for all bins in which the cross section is measured.

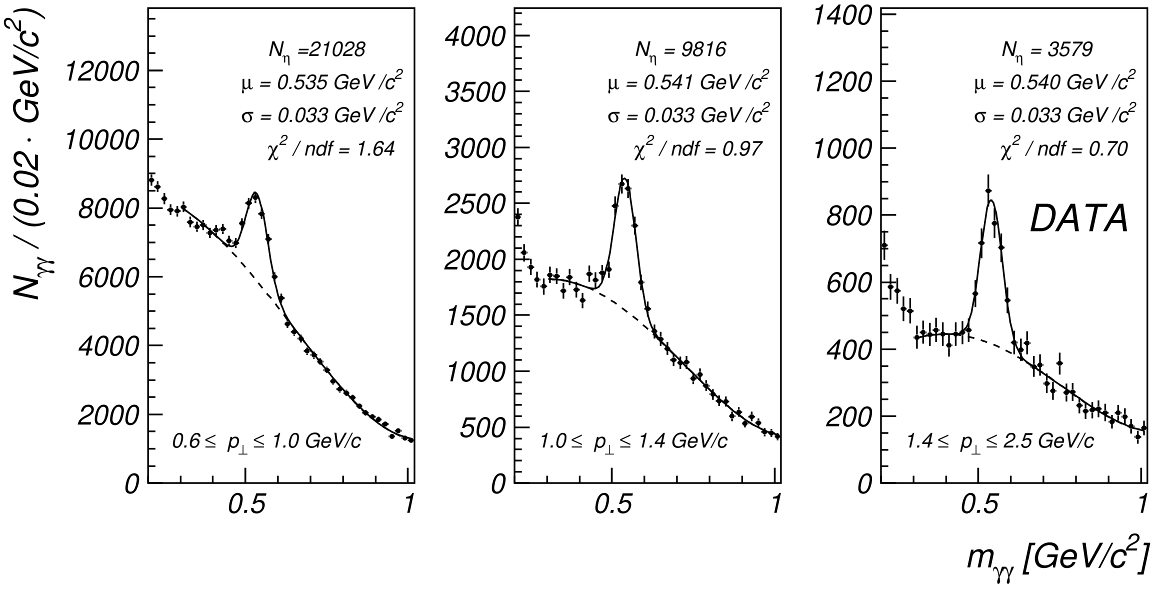

Figure 7.2: *Data: $m_{\gamma\gamma}$ spectra of the SpaCal in the mass range of the η meson for different intervals of the η transverse momentum and for the η rapidity range: -3.5 < y < -1.5.*

7.3 The η Reconstruction Efficiency

The reconstruction efficiencies for the η mesons were determined with the help of the same MC models, PYTHIA and PHOJET, as used for the determination of the π^0 reconstruction. The η signal in the simulated events is displayed in figure 7.3

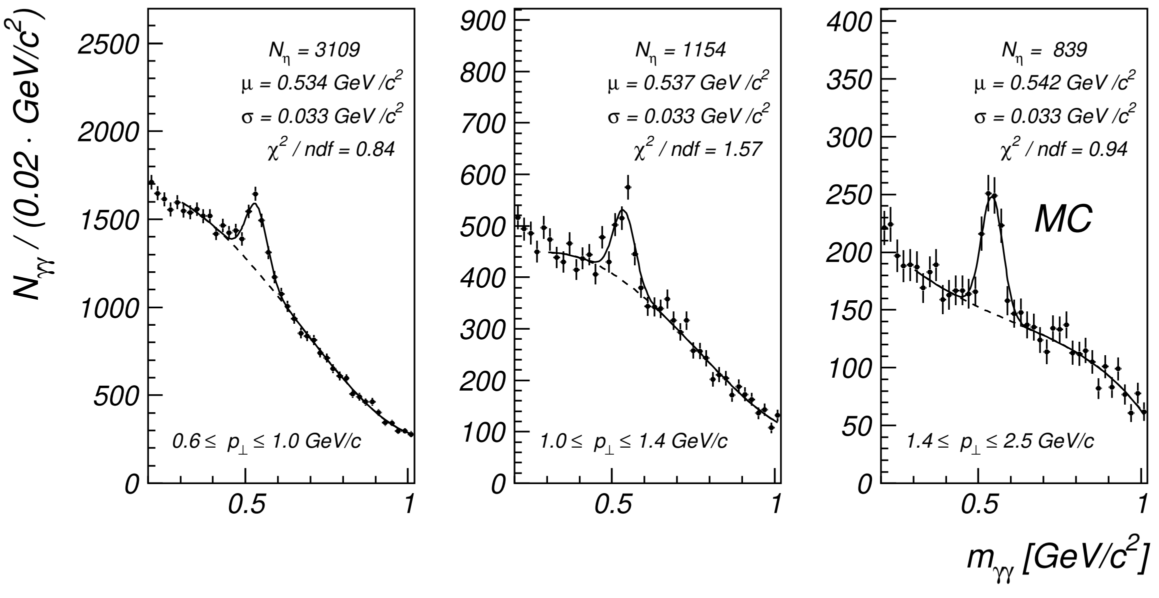

Figure 7.3: *The same distributions as shown in figure 7.2 for the simulated events generated by the MC models PYTHIA and PHOJET (see text).*

As in the case of the π^0 mesons the shape of signal and background is well reproduced by the simulated events.

For both generators the number of fully simulated events is about 1 million. After applying the cuts simulating subtrigger 50, this number of events is still too small to see a clear η signal in the SpaCal for each MC separately. Therefore, both samples of simulated events were combined. The error on the MC dependence of the η analysis was transferred from the studies with the π^0 mesons. There, the dependence varied between 5 and 15 %. To be conservative, the MC dependence for the η analysis was assumed to be as large as the maximal value of the π^0 analysis, namely 15 %.

Another important question concerns correction factors due to the cuts on the most energetic cluster ($E_1 > 2.2$ GeV) in the SpaCal and on the radial distance of its cluster center from the beam line ($RD_1 > 16$ cm), necessary for simulating subtrigger 50 (see section 4.2). In table 7.1 the correction factors due to the cuts simulating subtrigger 50 are listed for the bins in which the cross section is measured. The correction factors were derived with the MC models PHOJET and PYTHIA via the ratio of the number of ηs generated in the corresponding intervals over the number of ηs remaining in these intervals after applying the cut on E_1 and RD_1.

$p_\perp$ interval [GeV/c]	$[0.6, 1.0]$	$[1.0, 1.4]$	$[1.4, 2.1]$
corr. factor (PYTHIA)	2.55	1.83	1.52
corr. factor (PHOJET)	2.46	1.78	1.32
corr. factor (mean)	2.51 ± 0.05	1.81 ± 0.03	1.42 ± 0.1

Table 7.1: *Corrections factors for the η cross section measurement due to the cuts on the most energetic cluster in the SpaCal and on the radial distance of its center from the beam line.*

As in the case of the π^0s the largest differences between the two MC models occurs in the largest $p_\perp$-interval.

7.4 Discussion of Systematic Errors

The η cross section is measured via formula 6.1. Most of the systematic errors of the quantities needed for the determination of the cross section are already discussed in the context of the π^0 analysis in section 6.4. Here, for reasons of transparency, the systematic errors are summarized once more in table 7.2, differences between the two measurements are marked by an arrow in the corresponding column.

1) Uncertainty on the efficiency of subtrigger 50	$\Delta\epsilon_{\mathrm{st50}}$	1 %
2) Uncertainty on the electron tagger efficiency	$\Delta\epsilon_{\mathrm{eTag}}$	6 %
3) Contributions of π^0s due to beam-gas events	$\Delta N_{\pi^0,\mathrm{BG}}$	< 1 %
4) Error on the number of η mesons due to a 4 % uncertainty on the energy scale	$\rightarrow \Delta N_\eta$(energy)	15 %
5) Data: Error on the number of η mesons due to the fitting procedure	$\rightarrow \Delta N_\eta$(fit, data)	7 %
6) MC: Error on the number of η mesons due to the fitting procedure	$\rightarrow \Delta N_\eta$(fit, MC)	7 %
7) MC dependence	$\rightarrow \Delta N_\eta$	15 %
8) Error on integrated Luminosity $\mathcal{L}$	$\Delta\mathcal{L}$	1.5 %

Table 7.2: *Systematic errors of the η measurement. The quantities marked with an arrow differ slightly from the corresponding values of the π^0 analysis.*

7.5 Results

Figure 7.4 shows the inclusive η photoproduction cross section in the same rapidity region in which the π^0 cross section is measured ($-3.5 < y < -1.5$) for three intervals of $p_\perp$. The corresponding values are given in table 7.3. The bin-center correction was performed with the method sketched in section 6.5.

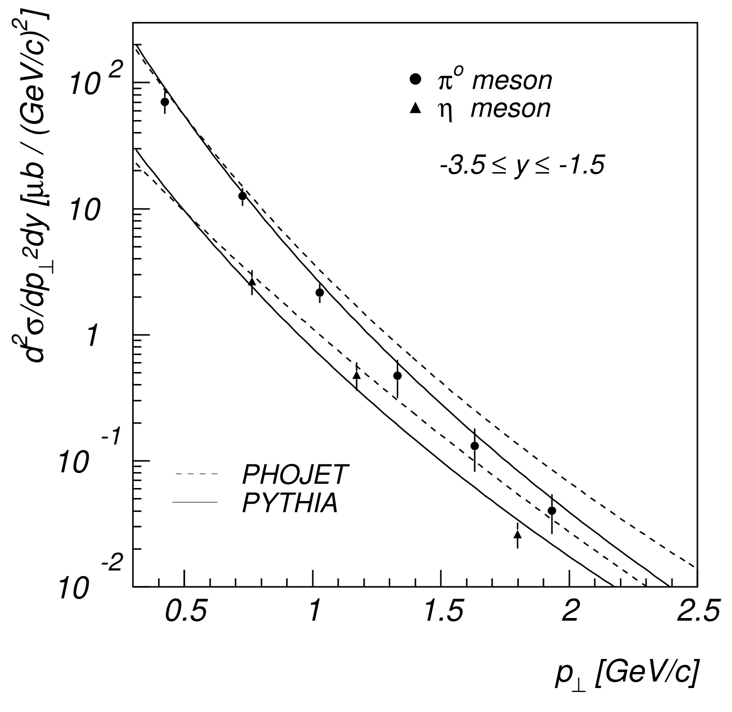

Figure 7.4: *Comparison of the inclusive π^0 and η photoproduction cross sections as a function of $p_\perp$, for the rapidity region $-3.5 < y < -1.5$, for $Q^2 \leq 0.01$ GeV^2 and $0.35 < y_{\mathrm{B}} < 0.65$. The curves are predictions of the PHOJET (dashed) and PYTHIA (full) models.*

y	$p_\perp$ [GeV/c]		
	$[0.6, 1.1]$ (0.76)	$[1.1, 1.4]$ (1.17)	$[1.4, 2.5]$ (1.79)
$[-3.5, -1.5]$	2.88 ± 0.64	0.52 ± 0.13	0.028 ± 0.006

Table 7.3: *Inclusive η photoproduction cross sections $d^2\sigma/dp_\perp^2 dy$ ($\mu b/(GeV/c^2)$) for different bins of the η transverse momentum $p_\perp$ and rapidity y. In addition to the interval limits, the bin centers are quoted.*

The MC model PYTHIA describes both the π^0 and η cross section very well while PHOJET tends to overestimate the cross sections for transverse momenta above $\approx$ 1.0 GeV/c. One observes that the cross sections approach each other with increasing values of the transverse momenta of the mesons. To quantify this effect the ratio of both cross sections was determined. For this purpose the π^0 cross section was measured in the same bins as the η cross section with the minimum bias data. The results of the π^0 cross section with the modified binning is compared with the previous one in figure 7.5 (left).

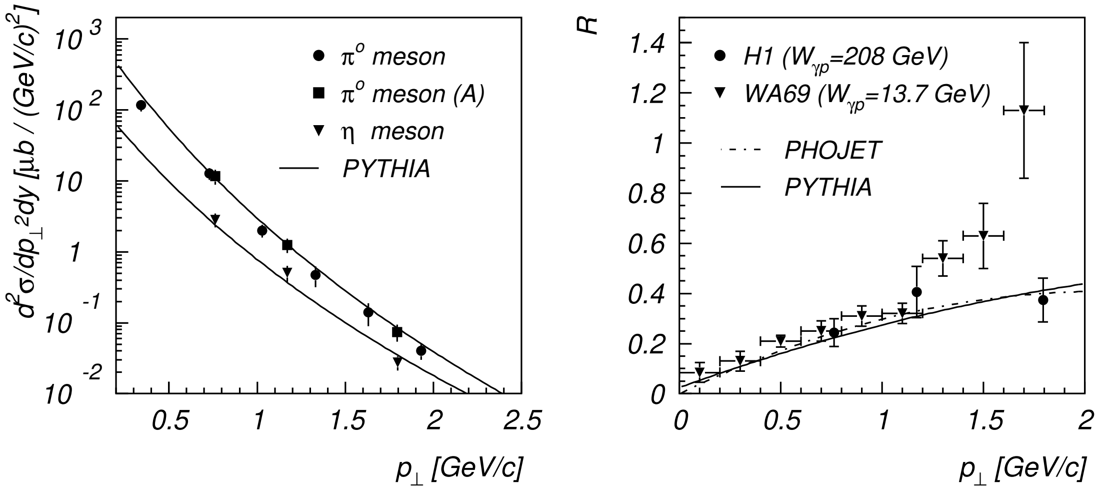

Figure 7.5: *Left side: the same cross sections as shown in figure 7.4. The squares (A) show the π^0 cross section measured in the same bins in which the η cross section is measured. Right side: Ratio R of the η/π^0 photoproduction cross sections as a function of the transverse momenta of the mesons in the interval $-3.5 < y < -1.5$. $R = \frac{d^2\sigma}{dp_\perp^2\, dy}(\eta)/\frac{d^2\sigma}{dp_\perp^2\, dy}(\pi^0)$.*

Within the errors both π^0 measurements agree. This demonstrates the stability of the π^0 cross section measurement with respect to the binning chosen. The ratio of the differential η and π^0 cross sections as a function of $p_\perp$ in the rapidity interval $-3.5 < y < -1.5$ is also shown in figure 7.5 (right) and compared with the predictions of PHOJET and PYTHIA. The MC model PYTHIA describes this ratio excellently. The agreement with PHOJET is also good, although it overestimates the π^0 as well as the η cross sections. This indicates that the processes which lead PHOJET to predict too large a meson cross section are the same for the π^0 and η production. In addition this ratio is compared with a previous measurement of the Omega Photon Collaboration of 1992 (WA69). At low $p_\perp$ values

($p_\perp < 1.2$ GeV/c) the WA69 results agree within the errors with the results presented here and they agree with the MC predictions for this ratio at $W_{\gamma p} \approx 208$ GeV. At larger $p_\perp$ values differences between both measurements are visible. In [APS92] several reasons are discussed which explain the variation of the ratio of the η/π^0 production. The most obvious reason appears to be that gluons are flavour blind. Thus, in the fragmentation processes, u, d and s quarks are "democratically" produced as long as mass effects can be neglected. With decreasing values of $p_\perp$, mass effects have to be taken into account which lead, due to the larger s quark mass, to a larger production of (u, d) quarks and antiquarks. Therefore, one expects π^0 and η mesons produced with nearly equal rates at large values of $p_\perp$ while at smaller values of $p_\perp$ the π^0 production should dominate. The data show this behaviour. Of course, the comparison of the H1 data and the WA69 results have to be taken with a grain of salt due to the large differences of the CM energies and the phase space regions.

Chapter 8

The Search for Particles in the Higher Mass Range

In the preceding chapters the π^0 and η cross section measurements in the photon hemisphere at HERA with the help of the H1 detector were presented. The SpaCal as well as the LAr calorimeters turned out to be suitable tools to perform mass spectroscopy with light mesons. Consequently the next step is to study the production of particles which decay via π^0 or η mesons into pure photonic final states.
The following table summarizes those particles which cascade down via π^0 and η mesons into pure photonic final states [PDG98]:

particle	**mass [MeV/c^2]**	Γ_{tot} **[MeV/c^2]**	**decay-channel**	**branching ratio**
ρ^0	769.9 $\pm$ 0.8	151.2 $\pm$ 1.2	$\pi^0\gamma$ $\eta\gamma$	(7.9 $\pm$ 2.0) $\times 10^{-3}$ % (3.8 $\pm$ 0.7) $\times 10^{-4}$ %
ω	781.94 $\pm$ 0.12	8.43 $\pm$ 0.1	$\pi^0\gamma$ $\eta\gamma$	(8.5 $\pm$ 0.5) % (8.3 $\pm$ 2.1) $\times 10^{-4}$ %
$\eta\prime$	957.77 $\pm$ 0.14	0.201 $\pm$ 0.016	$\pi^0\pi^0\eta$ $\gamma\gamma$	(20.8 $\pm$ 1.3) % (2.12 $\pm$ 0.13) %
$a_0(980)$	983.4$\pm$ 10	50 - 100	$\eta\pi^0$	dominant
ϕ	1019.413 $\pm$ 0.008	4.43 $\pm$ 0.06	$\eta\gamma$ $\pi^0\gamma$	(1.28 $\pm$ 0.06) % (1.31 $\pm$ 0.13 $\times 10^{-3}$ %
$f_2(1270)$	1275 $\pm$ 1.2	185.5 $\pm$ 3.8	$\pi^0\pi^0$	(28.2 $\pm$ 0.8) %
$a_2(1320)$	1318.1 $\pm$ 0.6	107 $\pm$ 5	$\eta\pi^0$	(14.5 $\pm$ 1.2) %
$f_0(1500)$	1500 $\pm$ 10	112 $\pm$ 10	$\eta\eta$	seen
$f_2'(1525)$	1525 $\pm$ 5	76 $\pm$ 10	$\eta\eta$	(10.3 $\pm$ 3.1) %

Table 8.1: *List of neutral particles decaying into pure photon states.*

The ρ^0 and ϕ mesons have a branching ratio for their decays into $\pi^0\gamma$ and $\eta\gamma$ on the one percent level. 20.8 % of all η' mesons decay into $\pi^0\pi^0\eta$, i.e. a six photon final state, and only 2.12 % into two photons. Since the probability for the detection of particles decreases with an increasing number of photons in the final state, the best conditions for their detection with the H1 calorimeters exist for the ω and the mesons listed above in the mass range between 1270 MeV/c^2 and 1525 MeV/c^2.

8.1 The ω Meson

The ω is already well established at HERA. The ZEUS collaboration determined the cross section of the process $\gamma p \to \omega p$ to (1.21 ± 0.35) μb via the decay channel $\omega \to \pi^+\pi^-\pi^0$ [DER96]. At H1 the elastic ω photoproduction is presently studied via the decay of the ω into $\pi^0\gamma$ [BER97]. The branching ratio for this channel is 8.5 %. The determination of the ω cross section via this channel is difficult due to contributions of the ρ^0 meson, which have to be taken into account. In the ω analysis the cut $\sum_{e',\omega}(E - p_z) > 50$ GeV is applied which mainly selects elastic events. For elastic events the following equation holds approximately:

$$2E_e = \underbrace{(E-p_z)_e}_{=2\cdot E_e} + \underbrace{(E-p_z)_P}_{=0} = (E-p_z)_{e'} + \underbrace{(E-p_z)_{P'}}_{\approx 0} + (E-p_z)_\omega \tag{8.1}$$

with $E_P = p_{z,P}$ and $E_e = -p_{z,e}$. e, P, e', P', ω denote the incoming electron, proton, the outgoing electron, proton and the produced ω, respectively.
The reconstruction of the ω mesons in the SpaCal from three photons with roughly the same cuts as applied in [BER97] (see table 8.2) leads to the ω signal shown in plot A of figure 8.1.

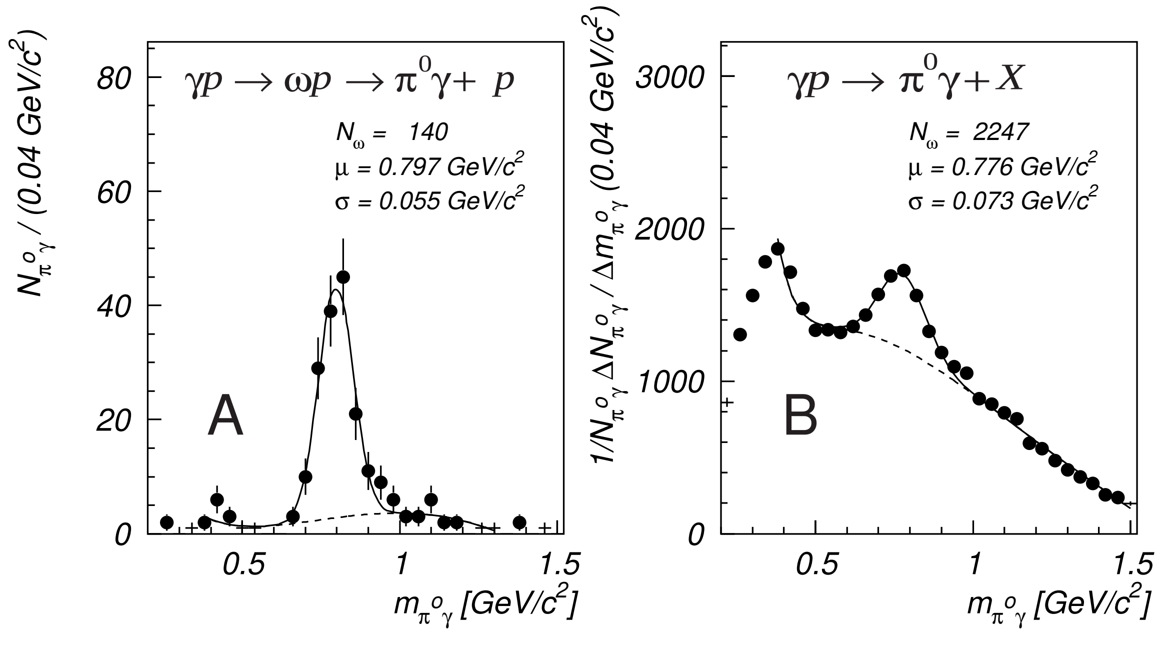

Figure 8.1: *SpaCal: A. $\pi^0\gamma$ mass spectrum which comes from elastic events, B. inclusive $\pi^0\gamma$ mass spectrum.*

There is a clear peak visible with a mean value of 797 MeV/c^2 and a width of 55 MeV/c^2 which is in agreement with the natural width of the ω folded with the energy resolution of the SpaCal. Thus, this peak can clearly be associated with the ω meson.

If one drops the cut $(E-p_z)_{e\omega} > 50$ GeV and in order to reduce the background increases the cut on the minimal photon energy from 0.4 GeV to 1.0 GeV for the photons of the π^0 mesons and to 2.5 GeV for the lonely photon of the $\pi^0\gamma$ combination (see table 8.2), one obtains the inclusive $\pi^0\gamma$ spectrum which is displayed in plot B of figure 8.1. Again, a clear ω signal is visible, located at the falling part of the background distribution. The mean value and the width of the exclusive ω signal (A) differ slightly from the corresponding values of the inclusive ω peak (B). This can be explained by the fact that the ω mesons shown in A and B, respectively, populate completely different phase space regions. The elastically produced ω mesons are mainly found in a rapidity region below -3 while the largest part of the inclusively measured ω mesons fulfil the condition $y_\omega > -3$. The clear inclusive ω signal justifies and encourages one to extend the search for heavier mesons into the mass range around 1500 MeV/c^2.

A. Photon selection	B. Photon selection
$8 <$ RD < 75 cm	$8 <$ RD < 75 cm
R < 3.5 cm	R < 3.5 cm
E > 0.4 GeV	E > 1.0 GeV
A. event selection	**B. event selection**
$0.3 < y_{\rm B} < 0.7$	$0.3 < y_{\rm B} < 0.7$
no reconstructed Vertex	Vertex reconstructed
-	$\lvert Z_{\rm Vertex}\rvert < 35$ cm
$N_\gamma = 3$	-
$52 < (E - p_z)_{e\omega} < 60$ GeV	-
$y_\omega < -3$	$E^3_\gamma > 2.5$ GeV

Table 8.2: *A. Selection cuts for the exclusive $\pi^0\gamma$ spectrum. B. Selection cuts for the inclusive $\pi^0\gamma$ spectrum. RD = Radial Distance of the cluster center to the beam line, R = Cluster radius, E = Cluster energy, y_ω = Rapidity of the ω meson, E^3_γ = "lonely" photon energy of the $\pi^0\gamma$-combination.*

8.2 The Search for Mesons in the 1500 MeV/c^2 Mass Range

The search for particles in the mass range around 1500 MeV/c^2 is interesting in the context of the search for glueball candidates, i.e. particles assumed to be bound gluonic states. Despite the fact that QCD calculations foresee such states, precise and reliable predictions concerning masses and widths are difficult. However, QCD inspired models supply a guide which helps to discriminate glueballs from ordinary $q\bar{q}$ states [CLO88]:

1. glueballs can have exotic J^{PC} quantum numbers not accessible to ordinary $q\bar{q}$ mesons,
2. glueballs can have anomalous production or decay characteristics,
3. glueballs are SU(3) singlets, they carry neither charge nor flavour and thus can not couple directly to photons, they are expected to be "flavour blind",
4. glueballs are copiously produced in "gluon rich" environments.

Traditionally mass spectroscopy is the basis of any glueball search. According to the conditions listed above, glueballs must lie outside SU(3) nonets which describe ordinary $q\bar{q}$ states. Despite the large amount of data available, hadron spectroscopy is very difficult due to its complexity, the overlap of $q\bar{q}$ ground states and radial excitations. Thus, each additional piece of information may be helpful for the identification of particles as glueballs.

Clearly, in γp reactions a lot of quarks and gluons are created. These reactions are visible for example as collimated particle bundles with high transverse momenta – so called high $p_{\perp}$-jets. Also the high particle multiplicity of γp events result from stretched colour fields between the copiously produced partons. Thus, photoproduction is a "gluon-rich" environment in which one should take the chance to look for glueball production.
One of the most promising candidates for a glueball is the scalar $f_0(1500)$ ($\mathrm{I} = 0, 0^{++}$) presented by Crystal Barrel in their analysis of $\pi^0\pi^0\pi^0, \pi^0\pi^0\eta$ and $\pi^0\eta\eta$ final states from $\bar{p}p$ annihilations at rest in liquid hydrogen [AMS92]. Later on Crystal Barrel confirmed the presence of the $f_0(1500)$ scalar resonance in $\eta\eta$ and $\pi^0\pi^0$ with high statistics data in $\bar{p}p$ annihilations at rest [ANI94]. Beside a clear signal at 1500 MeV/c^2 in the $\pi^0\pi^0$ mass spectrum there was also the striking peak of the $f_2(1270)$ visible.
Therefore the possible production of the $f_0(1500)$ and the $f_2(1270)$ in γp events at HERA energies was studied in this analysis.
Since neither the PHOJET nor the PYTHIA event generator produces these mesons, a TOY MC[1] was used for the determination of their reconstruction efficiencies and for the cut optimization. The TOY MC calculates the photon flux with the help of the program IJRAY [ABT92], which distributes the energy of the incoming electron on the quasi-real photon according to the Weizäcker-Williams approximation. It was implemented in the PYTHIA event generator without accounting for the conservation of energy of the produced particles in the events.

8.2.1 The Search for the $f_0(1500)$

Beside the mass and width of the scalar $f_0(1500)$ (see table 8.1), the main ingredients for the TOY MC are the longitudinal and transverse momenta spectra of the $f_0(1500)$ which result from its production in the γp CM system. These distributions were derived with the help of the PYTHIA model from events with two η mesons scattered into the backward region of the H1 detector. The invariant mass of the two η mesons was calculated and the longitudinal and transverse momenta of the two-η combinations within a mass window around 1.5 GeV/c^2 were determined in the γp CM system and plotted in figure 8.2. According to these distributions the $f_0(1500)$ is first generated by the TOY MC in the γp CM system and then boosted into the H1 lab frame, where it decays isotropically into two η mesons which in turn decay isotropically in two photons. Figure 8.3 shows the energies and the polar angles of the final state photons of the decay $f_0(1500) \to \eta\eta \to \gamma\gamma\gamma\gamma$. $E_{\gamma 1}$ is the energy of the most energetic photon, $E_{\gamma 2}$ the energy of the second most energetic photon and so on, $\theta_1 ... \theta_4$ denote the polar angles of the corresponding photons. As illustrated in the θ distributions, the SpaCal covers the polar angular range $153^\circ < \theta < 178^\circ$ and the LAr calorimeter the range $4^\circ < \theta < 154^\circ$. These plots already indicate that the H1

[1]TOY MC = simplified MC model

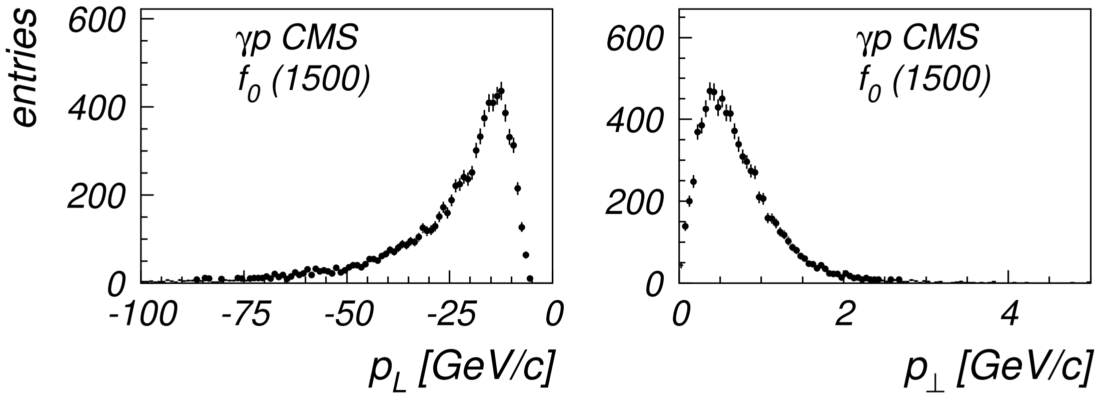

Figure 8.2: *Longitudinal (left side) and transverse (right side) momenta of the $f_0(1500)$ meson in γp CMS, used in the TOY MC.*

detector is not well suited for the search of mesons in the mass range about 1500 MeV/c^2. The decay photons with the largest energies lie mainly in the acceptance region of the SpaCal while approximately 90 % of the photons scattered into the central region of the LAr calorimeter have energies below 0.5 GeV. Since the cell size in the central region of the LAr calorimeter is 10×10 cm^2 and since the cut for the noise suppression has to be chosen around 0.5 GeV in this calorimeter, most of the low energy photons will not be resolved.

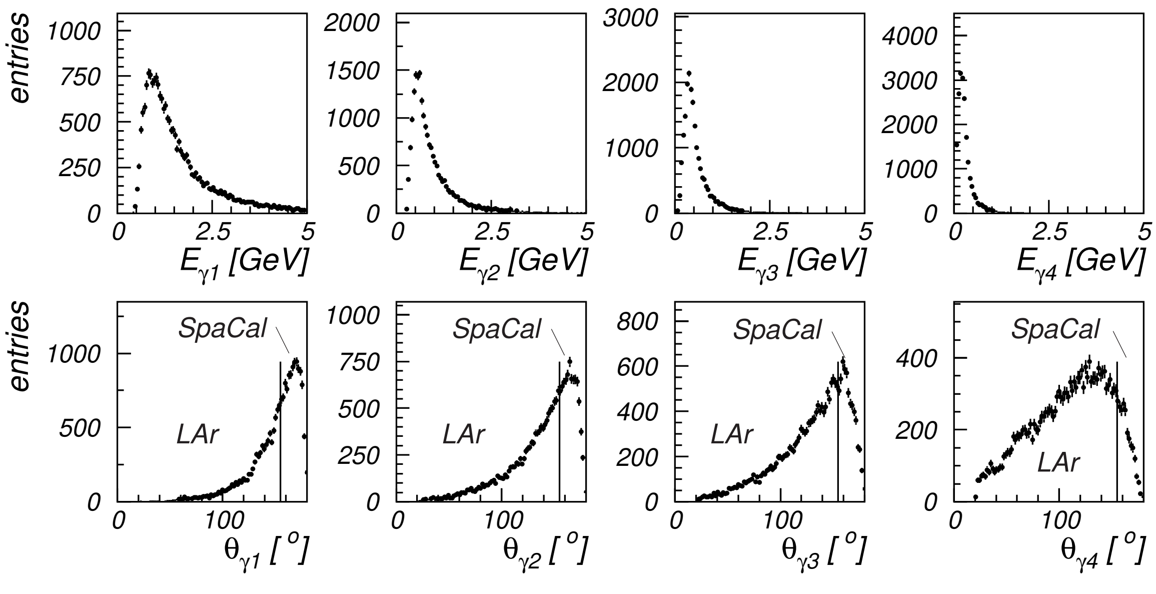

Figure 8.3: *TOY MC: Energy and polar angle distributions of the four decay photons of the $f_0(1500)$ as seen in the lab system. The line indicates the polar angular acceptance regions of the SpaCal and LAr calorimeter, respectively.*

In order to determine the reconstruction efficiency for the $f_0(1500)$, the events (generated by the TOY MC) were completely simulated and reconstructed with the help of the full H1 simulation and reconstruction programs. For the event generation two extreme assumptions were made:

1. only the $f_0(1500)$ is scattered into the backward region of H1
2. the $f_0(1500)$ is produced in addition to the ordinary particles generated by PYTHIA.

Assumption 1 leads to a two-photon spectrum as shown in figure 8.4. A clear η signal is visible for η mesons reconstructed in the SpaCal as well as for η mesons reconstructed with the help of both calorimeters, the SpaCal and the LAr calorimeter.

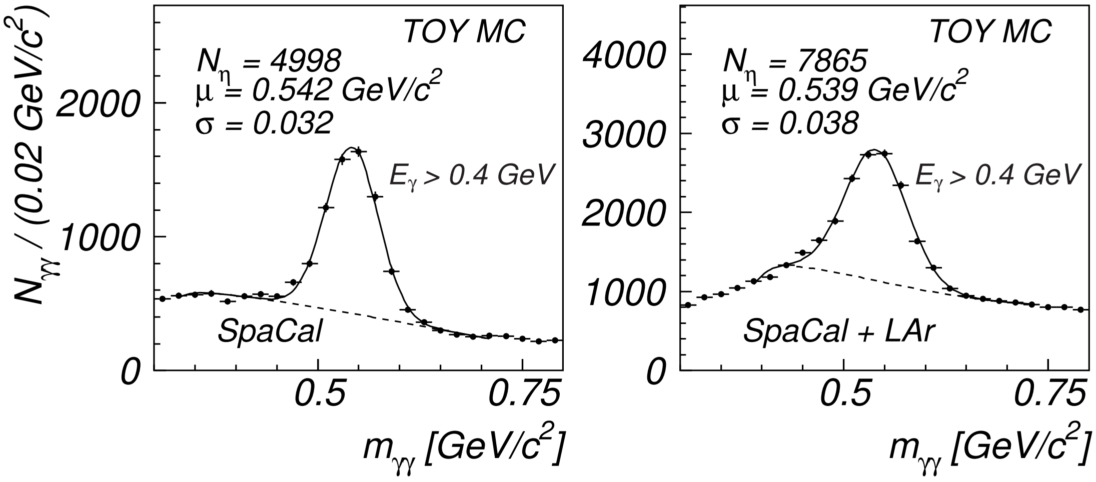

Figure 8.4: *TOY MC: The two-photon distribution of the decay $f_0(1500) \rightarrow \eta\eta \rightarrow \gamma\gamma\gamma\gamma$ as reconstructed in the SpaCal (left side) and as reconstructed in both, the SpaCal and LAr calorimeters (right side).*

For the latter case, all combinations of the decay photons were taken into account, i.e. combinations with both decay photons of the η meson registered in the SpaCal or the LAr calorimeter as well as the combinations with one decay photon in the SpaCal and the other in the LAr calorimeter. Compared to the number of η mesons found in the SpaCal alone, the inclusion of the LAr calorimeter increases the number of reconstructed η mesons by about 60 %. For the final reconstruction of the $f_0(1500)$ all two-photon combinations within the mass window of the η signal were selected and marked as η mesons. The invariant mass of all two-η combinations was calculated and plotted in figure 8.5. The left plot shows the $f_0(1500)$ signal reconstructed with the help of the SpaCal while the right plot displays the $f_0(1500)$ signal reconstructed with the help of the SpaCal and LAr calorimeter. The inclusion of the LAr calorimeter increases the efficiency of the $f_0(1500)$ only by 0.3 %. This can be explained, as already mentioned above, by the decay kinematics of the $f_0(1500)$. The decay photon with the lowest energy is preferentially scattered into the LAr calorimeter where a minimal cut on the energy of 400 MeV had to be applied for the suppression of background due to noise clusters. If one requires, in addition, the cuts for the simulation of subtrigger 50, $E_1 > 2.2$ GeV and $RD_1 > 16$ cm, the reconstruction efficiency decreases to a final value of 1.5 %.

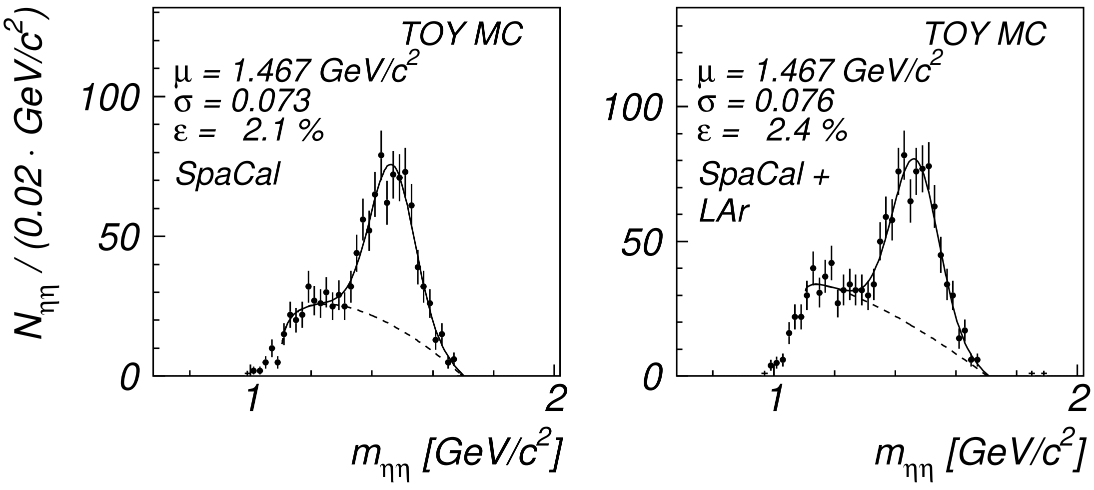

Figure 8.5: *TOY MC: Two-η spectra as seen in the SpaCal (left side) and as seen in the SpaCal and LAr calorimeters together (right side). Only the $f_0(1500)$ meson, scattered into the backward region of the H1 calorimeter, was generated by the TOY MC. The reconstruction efficiencies ϵ for the $f_0(1500)$ reconstruction are shown in the plots.*

For the more realistic **assumption 2**, the conditions for reconstructing the $f_0(1500)$ mesons become worse. Here the cut on the minimal photon energy had to be increased from 0.4 GeV to 0.8 GeV since only then the η signal became clearly visible in the detectors. Figure 8.6 shows the two-photon distribution for the case that the $f_0(1500)$ is produced in addition to the particles generated by PYTHIA. The corresponding two-η spectrum is also shown in figure 8.6 (right). The $f_0(1500)$ signal is no longer visible.

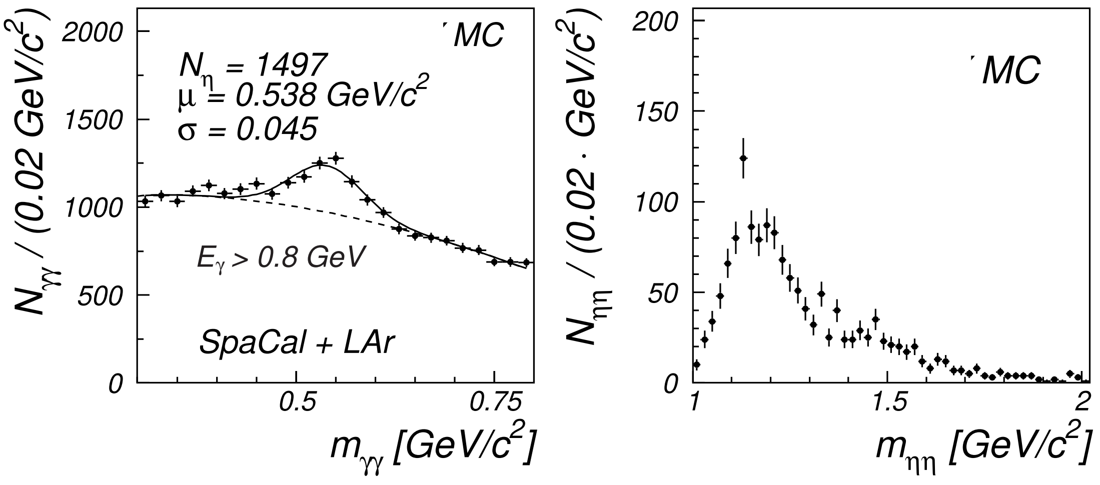

Figure 8.6: *TOY MC + PYTHIA: The two-photon distribution of events generated by PYTHIA with one additional $f_0(1500)$ added which was produced by the TOY MC in the backward region of H1. (left side). The $\eta\eta$ spectrum based on the selection of the two-photon combinations in the mass window around the η mass (right side).*

The reason for this is the merging of clusters generated by the $f_0(1500)$ final state photons with clusters generated by the photons from π^0 decays or by other hadrons copiously

produced in γp interactions at HERA. Thus, the efficiency of the $f_0(1500)$ reconstruction is clearly less than 1.6 %.
Figure 8.7 compares the $\eta\eta$-spectrum of assumption 2 with the $\eta\eta$-spectrum of the data selected by subtrigger 50. No $\eta\eta$ resonance is visible in the data within the mass range around 1500 MeV/c^2. The very low efficiency for the $f_0(1500)$ reconstruction does not allow any conclusions concerning the production properties of the $f_0(1500)$ in γp events at HERA (upper production limits for example).

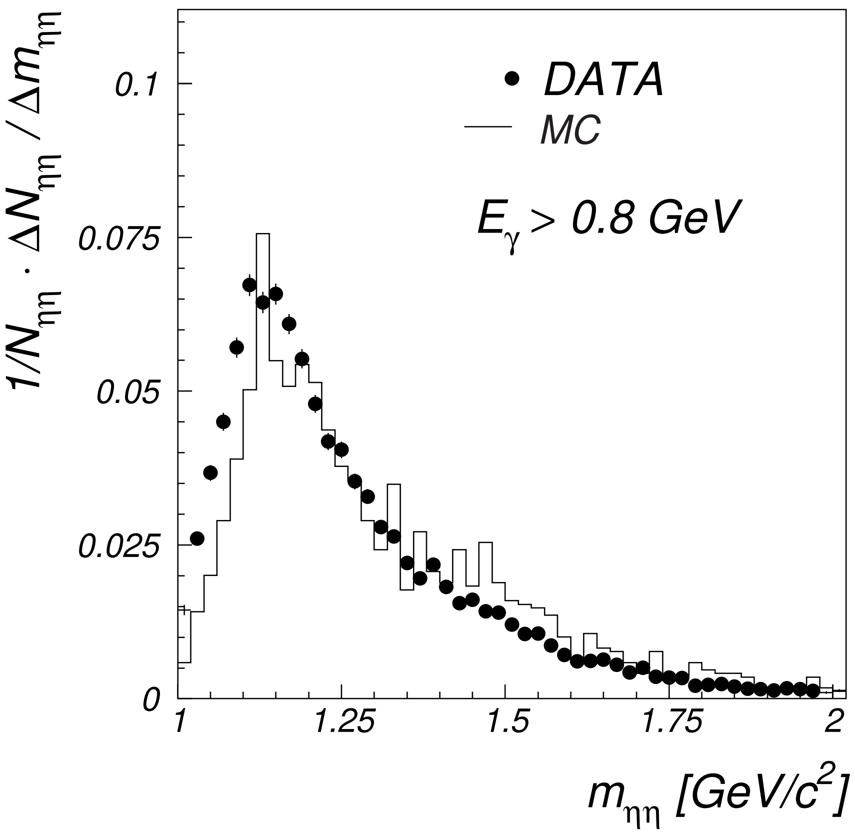

Figure 8.7: *Comparison of the $\eta\eta$ spectrum based on the data selected with subtrigger 50 with the spectrum predicted by PYTHIA with enhanced $f_0(1500)$ (TOY MC) production.*

8.2.2 The Search for the $f_2(1270)$

Finally the decay $f_2(1270) \to \pi^0\pi^0$ was investigated. The strategy of the search for this meson was the same as for the search of the $f_0(1500)$. Unfortunately, the differences of both mesons, in masses and widths of the mother and daughter particles respectively, are too small to result in visible differences of their reconstruction efficiencies. For the $f_2(1270)$ the reconstruction efficiency via two π^0 mesons was determined to be approximately the same as for the reconstruction of the $f_0(1500)$ via two η mesons, namely below 1.5 %. In figure 8.8 the two pion spectra of the data is compared with the prediction of the PYTHIA generator with enhanced production of the $f_2(1270)$. Again, there is no indication for a signal visible and due to the very low reconstruction efficiency, no conclusions can be drawn with respect to the production properties of the $f_2(1270)$.

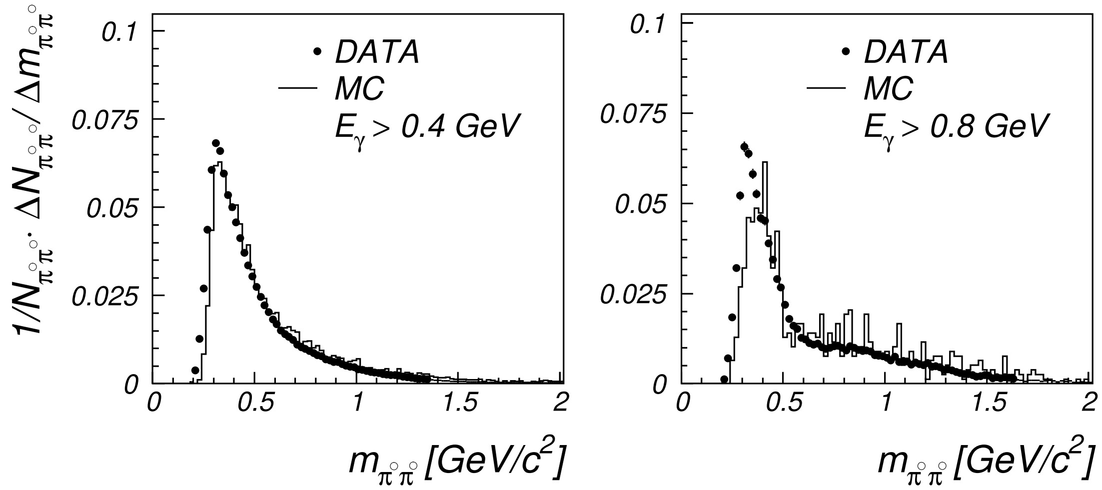

Figure 8.8: *Comparison of the $\pi^0\pi^0$ mass spectrum based on the data selected with subtrigger 50 with the spectrum predicted by PYTHIA with enhanced $f_2(1270)$ (TOY MC) production for two different cuts on the minimal photon energy.*

8.3 Outlook

The last section showed that the H1 detector is not suited for the search of inclusively produced mesons in the mass range above 1200 MeV/c^2. However, one should keep in mind that the situation is completely different for the exclusive photoproduction of particles. In this case, approximately the whole energy of the quasi-real photon is transferred to the meson. The larger energy of the meson leads to a much higher reconstruction efficiency of exclusively produced mesons compared with the highest efficiency possible (**assumption 1**) for the inclusively produced mesons. According to **assumption 1** only the $f_2(1270)$ ($f_0(1500)$) was scattered into the backward region of H1 with an energy distribution derived from inclusively measured $\pi^0\pi^0$ ($\eta\eta$) distributions.

Since the recently published paper [BER00] predicts a cross section of 20 nb for the exclusive $f_2(1270)$ meson photoproduction via Odderon exchange, the decay kinematics of this process at HERA energies is finally studied here.

The $f_2(1270)$ meson was produced with the help of the TOY MC with the $p_\perp$ spectrum given in [BER00]. The longitudinal momentum of the meson was transferred from the longitudinal momentum of the incoming quasi-real photon. The resulting energy and polar angle distributions of the four final states photons of the $f_2(1270)$ decay is shown in figure 8.9.

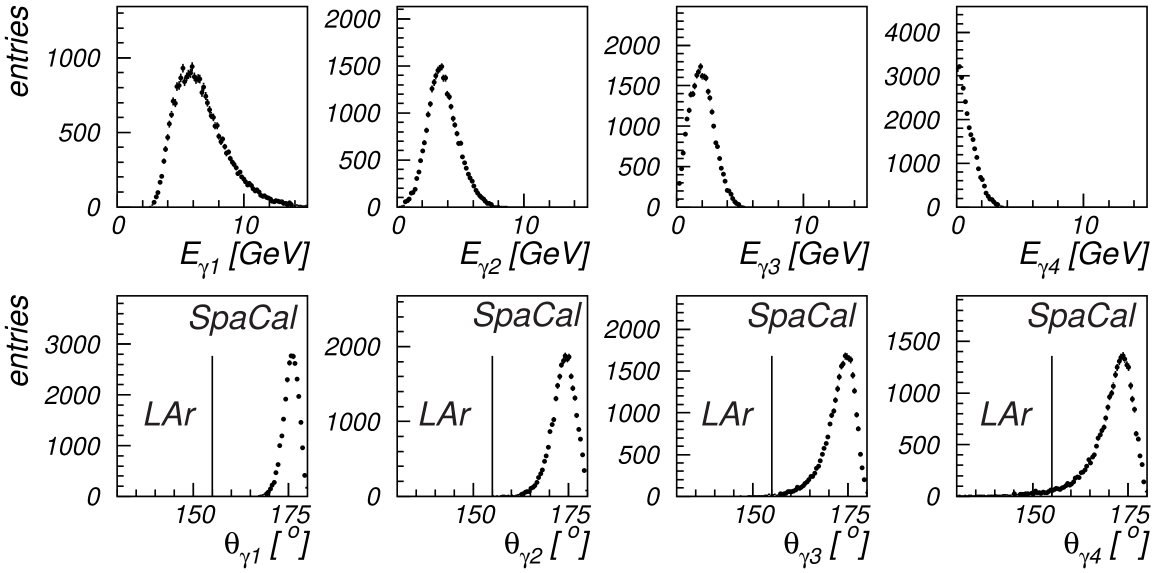

Figure 8.9: *TOY MC: Energy and polar angle distributions of the four decay photons of the exclusively produced $f_2(1270)$ as seen in the lab system. The line indicates the polar angular acceptance regions of the SpaCal and LAr calorimeter, respectively.*

Note that the scales of the coordinates in figure 8.9 differ from the scales in figure 8.3. Compared with the inclusive production of the scalar $f_0(1500)$ or the tensor meson $f_2(1270)$ nearly all decay photons are scattered with larger energies in the acceptance region of the SpaCal. There are two reasons for this differences:

- As already mentioned, the energy of the incoming photon is transferred to the interacting meson and is not shared between several particles.

- According to the production process presented in [BER00] the helicity $\pm$ 1 photon is diffractively transformed into a helicity $\pm$ 2 tensor meson f_2. The decay angle distribution of a helicity $\pm$ 2 tensor meson has a $\sin^4\theta^*$ dependence [PDG98]. The direction of the meson defines the quantisation axis with respect to which the polar angle θ^* of the decay particles is measured in the rest frame of the f_2. For the inclusively produced tensor meson f_2 one assumes that all its possible helicity states are equally occupied leading to an isotropic decay of the f_2. As shown in [BER97] the acceptance of the SpaCal for isotropically decaying particles is clearly worse than for particles with a $\sin^4\theta^*$ dependence of the decay angles.

The $f_2(1270)$ as reconstructed in the SpaCal is displayed in figure 8.10.

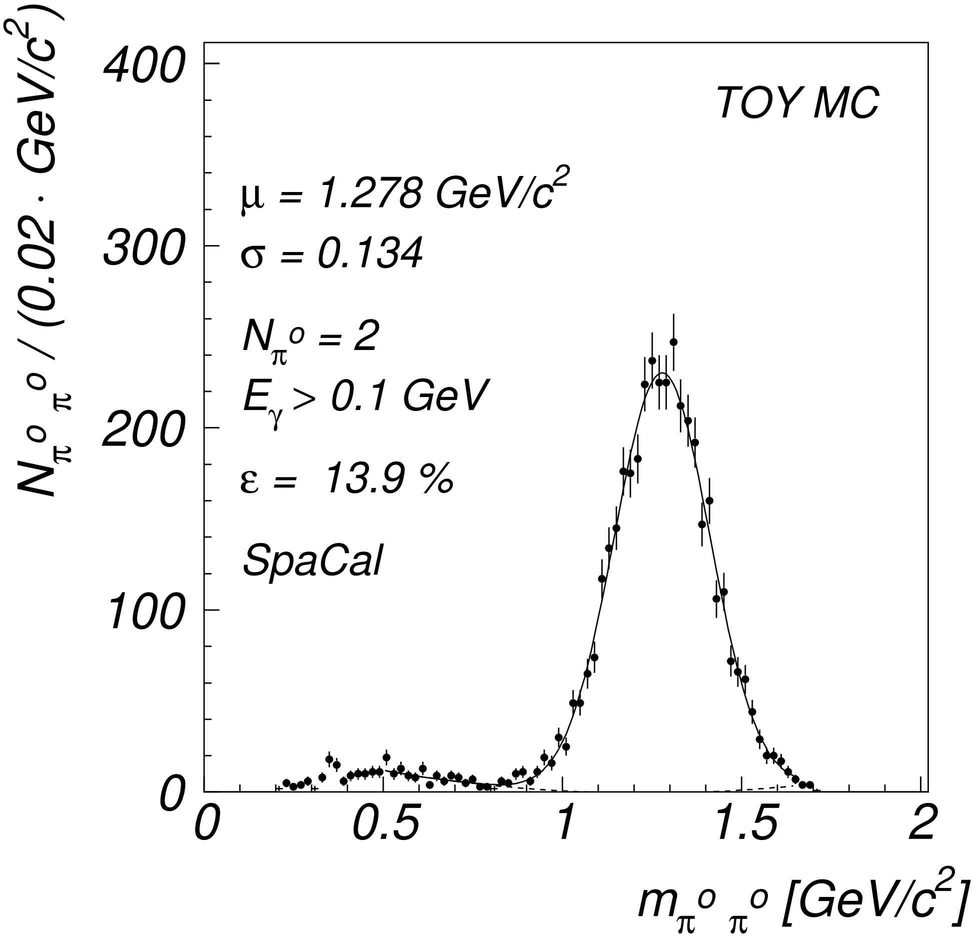

Figure 8.10: *TOY MC: Two-π^0 spectrum as seen in the SpaCal. Only the tensor meson $f_2(1270)$ was generated by the TOY MC with the $p_\perp$ distribution presented in [BER00].*

To avoid double counting of photons, only events with exactly two π^0 candidates were selected. This results in a very pure $f_0(1270)$ signal reconstructed with the correct mass and a width in agreement with the energy resolution of the SpaCal calorimeter. The efficiency for the $f_2(1270)$ reconstruction in an exclusive measurement with the help of the SpaCal is ≈ 14 %. The acceptance for the $f_2(1270)$ reconstruction is reduced by a factor of two to ≈ 7 %, if, in addition to the photon selection criteria, the cuts simulating subtrigger 50, $E_1 > 2.2$ GeV and $RD > 16$ cm, are applied. With this efficiency of the SpaCal for the Odderon induced $f_2(1270)$ photoproduction, all quantities are known for the estimation of the number of $f_2(1270)$ tensor mesons expected in the data of 1996 via:

$$N_{f_2(1270)} = \sigma(\gamma p \to f_2(1270)p) \cdot \Phi \cdot \mathcal{L} \cdot \epsilon_{\,\mathrm{eTag}} \cdot \epsilon_{\,\mathrm{SpaCal}} \cdot \Gamma_{f_2(1270)\to\pi^0\pi^0} \qquad (8.2)$$

Φ denotes the flux factor, $\mathcal{L}$ the integrated Luminosity, $\epsilon_{\,\mathrm{eTag}}$ the efficiency of the electron tagger, $\epsilon_{\,\mathrm{eTag}}$ the efficiency of the SpaCal for the $f_2(1270)$ reconstruction and $\Gamma_{f_2(1270)\to\pi^0\pi^0}$ the branching ratio for the decay of the $f_2(1270)$ meson into two neutral pions. Using the quantities listed in table 8.3 one expects ≈ 10 $f_2(1270)$ mesons in the 1996 data. This number of $f_2(1270)$ mesons is too low for the detection of this particle via the Odderon induced process, but with the inclusion of the 1997 data, the detection appears possible from the technical point of view, provided the cross section for this process is 20 nb as calculated in [BER00].

$\sigma(\gamma p \to f_2(1270)p)$ [BER00]	20 nb
Φ	0.00968
$\mathcal{L}$	4.3 pb^{-1}
ϵ_{eTag}	0.5
ϵ_{SpaCal}	0.07
$\Gamma_{f_2(1270)\to\pi^0\pi^0}$	0.28

Table 8.3: *Quantities needed for the estimation of the number of $f_2(1270)$ tensor mesons in the data selected by subtrigger 50 in 1996 (Φ = photon flux, $\mathcal{L}$ = integrated luminosity, ϵ_{eTag} = efficiency of the electron tagger, ϵ_{SpaCal} = efficiency of the SpaCal calorimeter for the reconstruction of the $f_2(1270)$ mesons, $\Gamma_{f_2(1270)\to\pi^0\pi^0}$ = branching ratio for the decay of the $f_2(1270)$ meson into two neutral pions).*

Chapter 9

Summary and Conclusions

Inclusive π^0 and η photoproduction in the photon hemisphere has been analysed with the detector H1 at HERA in an as yet unexplored kinematical region. Differential cross sections with respect to transverse momentum $p_\perp$, rapidity y, and the Feynman variable x_F are presented. This work continues previous H1 measurements performed with charged particles. In the phase space region covered by both the charged particle and the neutral pion analysis, the agreement between neutral and charged pion differential cross sections is excellent. The neutral meson data extend the measurements towards the previously unexplored domain of large rapidity in the photon fragmentation region, sensitive to the photon remnant in resolved γp interactions at large $p_\perp$.
The differential π^0 cross section as a function of transverse momentum $p_\perp$ shows an exponential fall at lower $p_\perp$ values as seen in soft hadron-hadron collisions, but exhibits at values of $p_\perp$ larger than 1.5 GeV/c an enhancement which is expected for hard parton-parton scattering processes. The distribution in the entire $p_\perp$ range covered here is well described by a QCD based power law ansatz. The QCD inspired generator models, PHOJET and PYTHIA, are able to describe the measured cross sections in this kinematical domain, with a slight preference for PYTHIA.
Within the framework of the PYTHIA model the impact of different assumptions concerning the "primordial" $k_\perp$ distributions of the partons inside the photon on the π^0 cross section were studied. The data do not allow a conclusion regarding a finite "primordial" intrinsic transverse momentum of the "hadronic" photon.
Beside the π^0 also the η photoproduction cross section is well reproduced by PYTHIA while PHOJET tends to overestimate it. The situation changes if one considers the ratio of both cross sections. This ratio is very well reproduced by both MC models indicating that the process leading PHOJET to predict too large a cross section is the same for the π^0 as well as for the η production. The ratio of the η/π^0 photoproduction cross section increases with increasing values of the transverse momenta of the mesons.
π^0 and η mesons are an ideal starting point to look for higher mass mesons which are of interest e.g. in the context of the glueball search or in the context of rare production processes like Odderon-photon fusion. Careful acceptance studies for the decay of higher mass mesons ($f_0(1500)$, $f_2(1270)$) into pure photonic final states showed that these studies can be performed only in an exclusive measurement due to acceptance limitations of the H1 detector.

Appendix A

π^0 Reconstruction Efficiencies (ϵ_{π^0})

The following tables supply the π^0 reconstruction efficiencies determined as described in section 6.2.

ϵ_{π^0} for the Minimum Bias Data

-3.5 < y < -1.5 (SpaCal)			
$p_\perp$ [GeV/c]	PHOJET	PYTHIA	ϵ_{π^0}
[0.3, 0.6]	0.325 ± 0.026	0.320 ± 0.026	0.322 ± 0.026
[0.6, 0.9]	0.418 ± 0.033	0.423 ± 0.034	0.420 ± 0.034
[0.9, 1.2]	0.512 ± 0.041	0.472 ± 0.038	0.492 ± 0.044
[1.2, 1.5]	0.525 ± 0.042	0.448 ± 0.036	0.487 ± 0.055
[1.5, 1.8]	-	-	-
[1.8, 2.1]	-	-	-

-3.5 < y < -2.8 (SpaCal)			
$p_\perp$ [GeV/c]	PHOJET	PYTHIA	ϵ_{π^0}
[0.2, 0.6]	0.272 ± 0.022	0.314 ± 0.025	0.293 ± 0.031
[0.6, 0.8]	-	-	-

-2.8 < y < -2.4 (SpaCal)			
$p_\perp$ [GeV/c]	PHOJET	PYTHIA	ϵ_{π^0}
[0.2, 0.6]	0.390 ± 0.031	0.409 ± 0.033	0.400 ± 0.033
[0.6, 0.8]	0.73 ± 0.058	0.758 ± 0.061	0.744 ± 0.061
[0.8, 1.0]	-	-	-
[1.0, 2.0]	-	-	-

-2.4 < y < -2.0 (SpaCal)			
$p_\perp$ [GeV/c]	PHOJET	PYTHIA	ϵ_{π^0}
[0.2, 0.6]	0.353 ± 0.028	0.351 ± 0.028	0.352 ± 0.028
[0.6, 0.8]	0.569 ± 0.046	0.526 ± 0.042	0.548 ± 0.049
[0.8, 1.0]	-	-	-
[1.0, 2.0]	-	-	-

-2.0 < y < -1.5 (SpaCal)			
$p_\perp$ [GeV/c]	PHOJET	PYTHIA	ϵ_{π^0}
[0.2, 0.6]	0.231 ± 0.018	0.236 ± 0.019	0.233 ± 0.019
[0.6, 0.8]	0.343 ± 0.027	0.330 ± 0.026	0.336 ± 0.028
[0.8, 1.0]	-	-	-
[1.0, 2.0]	-	-	-

-0.5 < y < 1.0 (LAr - AE0R)			
$p_\perp$ [GeV/c]	PHOJET	PYTHIA	ϵ_{π^0}
[0.8, 1.0]	0.123 ± 0.010	0.143 ± 0.011	0.133 ± 0.015
[1.0, 2.0]	0.186 ± 0.015	0.216 ± 0.017	0.201 ± 0.022

-0.5 < y < 1.0 (LAr - AE1R)			
$p_\perp$ [GeV/c]	PHOJET	PYTHIA	ϵ_{π^0}
[0.8, 1.0]	0.169 ± 0.013	0.158 ± 0.013	0.163 ± 0.014
[1.0, 2.0]	0.202 ± 0.016	0.222 ± 0.018	0.212 ± 0.019

Table A.1: π^0 *reconstruction efficiencies determined by the MC models PHOJET and PYTHIA in intervals of the* π^0 *rapidity* y *and of the transverse momentum* $p_\perp$ *of the* π^0*s.* ϵ_{π^0} *denotes the mean value of the efficiencies from PHOJET and PYTHIA.*

-3.5 < y < -1.5 (SpaCal)			
x_F [GeV/c]	PHOJET	PYTHIA	ϵ_{π^0}
$[0.1, 0.15]$	0.305 ± 0.024	0.295 ± 0.024	0.300 ± 0.025
$[0.15, 0.2]$	0.312 ± 0.025	0.334 ± 0.027	0.323 ± 0.028
$[0.2, 0.25]$	0.363 ± 0.029	0.386 ± 0.031	0.375 ± 0.032
$[0.25, 0.3]$	0.454 ± 0.036	0.394 ± 0.031	0.424 ± 0.045
$[0.3, 0.4]$	0.485 ± 0.039	0.466 ± 0.037	0.475 ± 0.039
$[0.4, 0.6]$	0.321 ± 0.026	0.319 ± 0.025	0.320 ± 0.026

Table A.2: π^0 *reconstruction efficiencies determined by the MC models PHOJET and PYTHIA in intervals of the variable* x_F*, Feynman x.* ϵ_{π^0} *denotes the mean value of the efficiencies from PHOJET and PYTHIA.*

ϵ_{π^0} for the Data Selected by Subtrigger 50 in 1996

-3.5 < y < -1.5 (SpaCal)			
$p_\perp$ [GeV/c]	PYTHIA	PHOJET	ϵ_{π^0}
$[0.3, 0.6]$	0.130 ± 0.008	0.144 ± 0.002	0.137 ± 0.008
$[0.6, 0.9]$	0.236 ± 0.013	0.247 ± 0.005	0.241 ± 0.010
$[0.9, 1.2]$	0.333 ± 0.005	0.330 ± 0.011	0.331 ± 0.008
$[1.2, 1.5]$	0.404 ± 0.022	0.349 ± 0.020	0.376 ± 0.035
$[1.5, 1.8]$	0.565 ± 0.042	0.418 ± 0.025	0.491 ± 0.081
$[1.8, 2.1]$	0.608 ± 0.058	0.435 ± 0.020	0.522 ± 0.095

-3.5 < y < -2.8 (SpaCal)			
$p_\perp$ [GeV/c]	PYTHIA	PHOJET	ϵ_{π^0}
$[0.2, 0.6]$	0.103 ± 0.008	0.113 ± 0.005	0.108 ± 0.008
$[0.6, 0.8]$	0.208 ± 0.014	0.204 ± 0.007	0.206 ± 0.011

-2.8 < y < -2.4 (SpaCal)			
$p_\perp$ [GeV/c]	PYTHIA	PHOJET	ϵ_{π^0}
$[0.2, 0.6]$	0.156 ± 0.009	0.163 ± 0.008	0.160 ± 0.009
$[0.6, 0.8]$	0.584 ± 0.021	0.624 ± 0.035	0.604 ± 0.034
$[0.8, 1.0]$	0.514 ± 0.047	0.506 ± 0.034	0.510 ± 0.041
$[1.0, 2.0]$	0.368 ± 0.054	0.351 ± 0.032	0.359 ± 0.044

-2.4 < y < -2.0 (SpaCal)			
$p_\perp$ [GeV/c]	PYTHIA	PHOJET	ϵ_{π^0}
$[0.2, 0.6]$	0.082 ± 0.001	0.095 ± 0.007	0.089 ± 0.008
$[0.6, 0.8]$	0.292 ± 0.015	0.282 ± 0.012	0.287 ± 0.014
$[0.8, 1.0]$	0.556 ± 0.024	0.584 ± 0.052	0.570 ± 0.040
$[1.0, 2.0]$	0.654 ± 0.040	0.590 ± 0.021	0.622 ± 0.044

-2.0 < y < -1.5 (SpaCal)			
$p_\perp$ [GeV/c]	PYTHIA	PHOJET	ϵ_{π^0}
$[0.2, 0.6]$	0.047 ± 0.004	0.043 ± 0.003	0.045 ± 0.004
$[0.6, 0.8]$	0.068 ± 0.002	0.074 ± 0.006	0.070 ± 0.005
$[0.8, 1.0]$	0.121 ± 0.003	0.143 ± 0.012	0.132 ± 0.013
$[1.0, 2.0]$	0.420 ± 0.016	0.337 ± 0.012	0.378 ± 0.044

-0.5 < y < 1.0 (LAr - AE0R)			
$p_\perp$ [GeV/c]	PYTHIA	PHOJET	ϵ_{π^0}
$[0.8, 1.0]$	0.028 ± 0.001	0.028 ± 0.001	0.028 ± 0.001
$[1.0, 2.0]$	0.042 ± 0.002	0.042 ± 0.004	0.042 ± 0.003

-0.5 < y < 1.0 (LAr - AE1R)			
$p_\perp$ [GeV/c]	PYTHIA	PHOJET	ϵ_{π^0}
$[0.8, 1.0]$	0.039 ± 0.005	0.031 ± 0.004	0.035 ± 0.005
$[1.0, 2.0]$	0.050 ± 0.005	0.050 ± 0.004	0.050 ± 0.005

Table A.3: π^0 *reconstruction efficiencies for the MC models PHOJET and PYTHIA in intervals of the* π^0 *rapidity y and of the transverse momentum* $p_\perp$ *of the* π^0*s.* ϵ_{π^0} *denotes the mean value of the efficiencies supplied by PHOJET and PYTHIA respectively.*

-3.5 < y < -1.5 (SpaCal)			
x_F [GeV/c]	PYTHIA	PHOJET	ϵ_{π^0}
[0.1, 0.15]	0.078 ± 0.003	0.074 ± 0.001	0.076 ± 0.003
[0.15, 0.2]	0.078 ± 0.001	0.087 ± 0.005	0.084 ± 0.006
[0.2, 0.25]	0.172 ± 0.006	0.179 ± 0.001	0.175 ± 0.014
[0.25, 0.3]	0.306 ± 0.013	0.337 ± 0.018	0.318 ± 0.023
[0.3, 0.4]	0.389 ± 0.049	0.420 ± 0.016	0.405 ± 0.036
[0.4, 0.6]	0.249 ± 0.017	0.271 ± 0.021	0.260 ± 0.022

Table A.4: π^0 *reconstruction efficiencies for the MC models PHOJET and PYTHIA in intervals of the variable* x_F*, Feynman x.* ϵ_{π^0} *denotes the mean value of the efficiencies supplied by PHOJET and PYTHIA, respectively.*

Appendix B

Charged Particle Fit for $p_\perp < 2$ GeV/c

Since the transverse momentum intervals of the charged particle measurement [ABT99] and the neutral pion analysis do not agree (see figure 6.11), a smooth interpolation of the charged particle data in the range $0.3 < p_\perp < 2$ GeV/c was performed. The interpolation and the fit function used are shown in figure B.1.

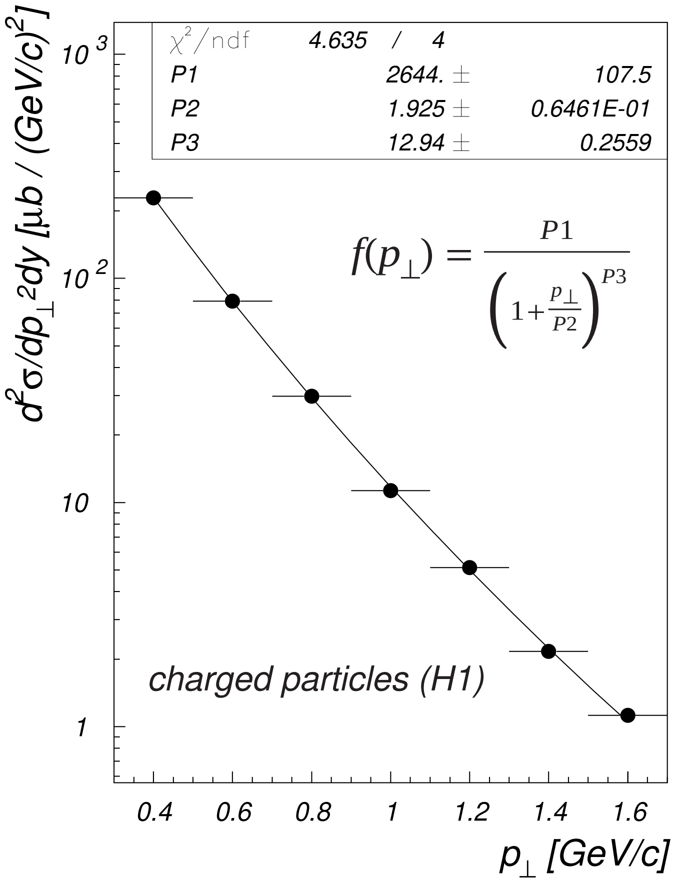

Figure B.1: *Charged particle cross section as a function of $p_\perp$ for $p_\perp < 2$ GeV/c with a smooth interpolation used to account for different momentum ranges in the charged particle and π^0 analysis respectively.*

For the comparison with the neutral pion cross section the resulting fit values were corrected for charged "non-pions" by subtracting a fraction of 17.5 %, the mean value of the PHOJET and PYTHIA prediction (17.5 ± 0.2 %), and divided by the isospin factor 2. The values used for the comparison are listed in table B.1

$p_\perp$ [GeV/c]	$\frac{\mathrm{d}^2\sigma}{\mathrm{d}p_\perp^2\,\mathrm{d}y}$ $[\mu b/(GeV/c)^2]$
0.69	50.1 ± 6.0
0.89	19.3 ± 2.3
1.35	2.7 ± 0.3

Table B.1: *Charged pion cross section (H1) (= "scaled" charged particle cross section) used for the comparison with the neutral pion data.*

Appendix C

Conversion of the Invariant Neutral Pion Cross Section as Measured by the Omega Photon Collaboration (WA69) to $\mathrm{d}\sigma/\,\mathrm{d}x_\mathrm{F}$

In section 6.6 the x_F distribution of the neutral pion production, as measured in this analysis, is compared with the x_F distribution measured by the Omega Photon collaboration (WA69) in γp collisions with an average photon energy of 80 GeV at a fixed target experiment [APS91]. Since WA69 did not measure the inclusive π^0 production as a function of x_F in bins of the π^0 rapidity but the invariant cross section $E \cdot d^3\sigma/dp^3$ as a function of the π^0 transverse momentum in bins of x_F, the WA69 data (accessible via [DUR]) had to be converted to cross sections differential in x_F. In this appendix the conversion of the WA69 data is described. Figure C.1 shows the invariant π^0 cross section as measured by WA69 at $W_{\gamma p} = 12.3$ GeV.

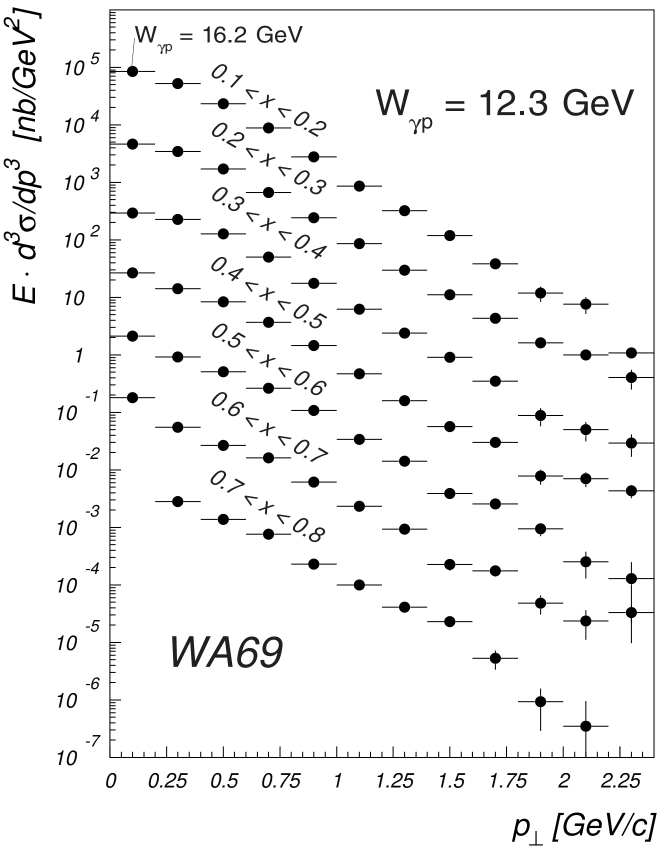

Figure C.1: *Invariant neutral pion cross section as measured by the Omega Photon collaboration (see text) at $W_{\gamma p} = 12.3$ GeV.*

Since the data point in the lowest $p_\perp$ and x_{F} bin is missing the corresponding data point at $W_{\gamma p} = 14.2$, also measured by WA69, was taken.

For the conversion

$$E \cdot \frac{\mathrm{d}^3\sigma}{\mathrm{d}p^3} \rightarrow \frac{\mathrm{d}\sigma}{\mathrm{d}x_{\mathrm{F}}}, \tag{C.1}$$

following relations were used:

$$\frac{\mathrm{d}\sigma}{\mathrm{d}x_{\mathrm{F}}} = p_{\mathrm{L}}^{\max} \cdot \frac{\mathrm{d}\sigma}{\mathrm{d}p_{\mathrm{L}}} \tag{C.2}$$

$$= \frac{\sqrt{s}}{2} \cdot \frac{\mathrm{d}\sigma}{\mathrm{d}p_{\mathrm{L}}} \tag{C.3}$$

and

$$\pi \cdot E \cdot \frac{\mathrm{d}^3\sigma}{\mathrm{d}p^3} = E \cdot \frac{\mathrm{d}^2\sigma}{\mathrm{d}p_\perp^2\,\mathrm{d}p_{\mathrm{L}}} \tag{C.4}$$

$E, p_\perp$ and p_{L} denote the energy, transverse and longitudinal momentum of the neutral pions respectively ($p_\perp^{\max}$ = maximal longitudinal π^0 momentum). With C.3 and C.4 one obtains:

$$\frac{\mathrm{d}\sigma}{\mathrm{d}x_{\mathrm{F}}} = \frac{\sqrt{s}}{2} \cdot \pi \int \underbrace{E\frac{\mathrm{d}^3\sigma}{\mathrm{d}p^3}}_{\mathrm{WA69}} \cdot \frac{1}{E}\,\mathrm{d}p_\perp^2 \tag{C.5}$$

$$= \sqrt{s} \cdot \pi \int \underbrace{E\frac{\mathrm{d}^3\sigma}{\mathrm{d}p^3}}_{\mathrm{WA69}} \cdot \frac{p_\perp}{E}\,\mathrm{d}p_\perp \tag{C.6}$$

$$\tag{C.7}$$

with

$$E = \sqrt{m^2 + p_\perp^2 + p_{\mathrm{L}}^2} \tag{C.8}$$

$$= \sqrt{m^2 + p_\perp^2 + (x_{\mathrm{F}}/2 \cdot \sqrt{s})^2} \tag{C.9}$$

For the calculation of E the bin centers of the x_{F} and $p_\perp$ intervals were used and m denotes the π^0 mass.

The integration of the WA69 data over the intervals of the π^0 transverse momenta yields the following values (table C.1):

Δx_{F}	$\frac{\mathrm{d}\sigma}{\mathrm{d}x_{\mathrm{F}}}$ $[\mu b]$
0.1 - 0.2	343.8 ± 3.5
0.2 - 0.3	152.3 ± 1.5
0.3 - 0.4	77.9 ± 0.7
0.4 - 0.5	43.5 ± 0.5
0.5 - 0.6	24.7 ± 0.2
0.6 - 0.7	13.3 ± 0.1

Table C.1: *Inclusive neutral pion cross section in intervals of* x_{F} *as derived from the invariant neutral pion cross section, measured by the Omega Photon collaboration (see text).*

Bibliography

[ABE94] F. Abe et al., CDF Collaboration, Phys. Rev **D50** (1994) 5550.

[ABR91] H. Abramowicz, E. M. Levin, A. Levy, and U. Maor, Phys. Lett. **B269** (1991) 465.

[ABT92] I. Abt, IJRAY Manual (Version 1.05);
H1 internal note H1-249 (1992)

[ABT94] H1 Collaboration, I. Abt et al., Phys. Lett. **B328** (1994) 176.

[ABT95] H1 Collaboration, I. Abt et al., Z. Phys. **C69** (1995) 27

[ABT97] H1 Collaboration, I. Abt et al., Nucl. Instr. and Meth. **A386** (1997) 310 & 348.

[ABT99] H1 Collaboration, C. Adloff et al., Eur. Phys. J. **C10** (1999) 363.

[ADL98] H1 Collaboration, C. Adloff et al., Eur. Phys. J. **C1** (1998) 97.

[ADL99] H1 Collaboration, C. Adloff et al., Eur. Phys. J. **C10** (1999) 363.

[AMS92] C. Amsler et al., Phys. Lett. **B291** (1992) 347.

[AND80] B. Andersson, G. Gustafson and T. Sjöstrand, Phys. Lett. **B 94** (1980) 211;
B. Andersson et al., Phys. Rep. **97** (1983) 31.

[AND94] H1 Calorimeter Group, B. Andrieu et al., Nucl. Instr. and Meth. **A350** (1994) 57.

[ANI94] V.V. Anisovich et al., Phys. Lett. **B 323** (1994) 233.

[APP95] H1 SpaCal group, Appuhn et al., DESY preprint 95-250, 1995

[APP96] R. D. Appuhn et al., The H1 SpaCal Group, Nucl. Instr. Methods **A382** (1996) 395;

[APP97] R. D. Appuhn et al., The H1 SpaCal Group, Nucl. Instr. Methods **A386** (1997) 397.

[APS91] Omega Photon Collab., R.J. Apsimon et al., Z. Phys. **C52** (1991) 397.

[APS92] Omega Photon Collab., R.J. Apsimon et al., Z. Phys. **C54** (1992) 185.

[ARN82] A. Arnison et al., Phys. Lett. **B118** (1982) 167.

[BAN85] UA2 Collab., M. Banner et al., Z. Phys. **C27** (1985) 329.

[BAS97] U. Bassler, G. Bernardi, DESY preprint 97-137, 1997

[BAU78] T. H. Bauer et al., Rev. Mod. Phys. **50** (1978) 261,
Rev. Mod. Phys. **51** (1979) 407.

[BER97] T. Berndt, Diploma Thesis, Heidelberg, (1997),
T. Berndt, Dissertation in preperation.

[BER00] E. R. Berger, A. Donnachie, H. G. Dosch, O. Nachtmann, hep-ph/0001270.

[BLA78] R. Blankenbecler, S. J. Brodsky and J. F. Gunion, Phys. Rev **D18** (1978) 900.

[BUE73] F.W. Büsser et al., Phys. Lett. **46B** (1973) 471;
F.W. Büsser et al., Nucl. Phys. **B106** (1976) 1.

[CAP94] A. Capella et al., Phys. Rep. **236** (1994) 225.

[CLO88] F.E. Close, Rep. Prog. Phys. **51** (1988) 833.

[DER94] ZEUS Collaboration, M. Derrick et al., Z. Phys. **C63** (1994) 391

[DE95a] ZEUS Collaboration, M. Derrick et al., Z. Phys. **C67** (1995) 227.

[DE95b] ZEUS Collaboration, M. Derrick et al., Phys. Lett. **354** (1995) 163

[DER96] ZEUS Collaboration, M. Derrick et al., hep-ex/9608010.

[DON92] A. Donnachie and P. V. Landshoff, Phys. Lett. **B296** (1992) 227.

[DUR] HEPDATA, the Durham RAL Databases, http://durpdg.dur.ac.uk/HEPDATA

[ENG95] R. Engel, PHOJET Manual (Version 1.04), Univ. Siegen Preprint 95-05 (1995);
R. Engel, Z. Phys. **C66** (1995) 203.

[ERD97] Erdmann, M., "The partonic structure of the Photon: Photoproduction at the lepton-proton Collider HERA", Sringer-Verlag, Berlin, 1997.

[FRI93] S. Frixione, Phys. Lett. **B319** ,339 (1993)

[GEA93] GEANT: Detector description and Simulation Tool, CERN Program Library Long Writeup W5013.

[GLU92] M. Glück, E. Reya and A. Vogt, Phys. Rev. **D46** (1992) 1973;
M. Glück, E. Reya and A. Vogt, Z. Phys. **C53** (1992) 127.

[HAG83] R. Hagedorn, Riv. Nuovo Cim. **6:10** (1983) 1.

[KOU80] C. Kourkoumelis et al., Z. Phys **C5** (1980) 95.

[LAF95] G. D. Lafferty and T. R. Wyatt, Nucl. Instr. Methods **A355** (1995) 541.

[LEV95] H1PHAN routine written by S. Levonian in 1995.

[NIC96] T. Nicholls et al.,The H1 SpaCal Group, Nucl. Instr. Methods **A374** (1996) 149.

[PDG98] The Particle Data Group, C. Caso et al., Eur. Phys. J. **C3** (1998) 1.

[SCH93] G.A. Schuler and T. Sjöstrand, Phys. Lett. **B300** (1993) 169;
G.A. Schuler and T. Sjöstrand, Nucl. Phys. **B407** (1993) 539.

[SJO87] T. Sjöstrand and M. Bengtsson, Comp. Phys. Comm. **43** (1987) 367;
H. - U. Bengtsson and T. Sjöstrand, Comp. Phys. Comm. **46** (1987) 43;
T. Sjöstrand, CERN-TH-6488 (1992).

[SJO94] PYTHIA Version 5.722, T. Sjöstrand, Comp. Phys. Comm. **82** (1994) 74;
T. Sjöstrand, "PYTHIA 5.7 and JETSET 7.4", CERN-TH.7112/93 (1993) (revised Feb. 1994).

[WEI34] C. F. Weizsäcker, Z. Phys. **88** (1934) 612; E. J. Williams, Phys. Rev. **45** (1934) 729.

Acknowledgements

Finally I would like to thank all the people who supported me during my time as a Ph.D. student. Especially many thanks to:

Prof. Karlheinz Meier for the opportunity to perform this thesis and for his useful and spontaneous advice whenever a problem occurred,

Prof. Franz Eisele for taking over the burden of the correction,

Armen Bunatyan and Jan Olsson for the long and detailed discussions about technical details of the analysis and the interpretation of the results,

all the H1 members who thoroughly cared about the publication of the π^0 paper,

Claus Beier; sharing a room and the delightful outdoor activities with him were a pleasure for me,

Selvam Damotharam, the inspiring voice, full of ideas, jokes and more,

Tommy Berndt, for his cheerful disposition and his smiley way to cope with physics problems,

Rick Cavanaugh, Oliver Nix, the youngsters Eric Wannemacher, Tobias Golling, Oliver Niedermeier for the friendly atmosphere.

Many thanks to Anke, who so patiently was enduring the time of my Ph.D. thesis.

And last but not least I would like to thank Jürgen Stiewe, who always was a reliable and helpful friend and colleague, without him there would have been more madness, less method.